NASA CONFERENCE PUBLICATION

NASA CP-2179

FLOAT ZONE WORKSHOP
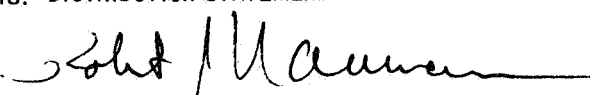
Summary of a Meeting Held at
Marshall Space Flight Center, Alabama,
December 12, 1980

Edited by R. J. Naumann

December 1980

1. REPORT NO. NASA CP-2179	2. GOVERNMENT ACCESSION NO.	3. RECIPIENT'S CATALOG NO.
4. TITLE AND SUBTITLE Float Zone Workshop		5. REPORT DATE December 1980
		6. PERFORMING ORGANIZATION CODE
7. AUTHOR(S) Edited by R. J. Naumann		8. PERFORMING ORGANIZATION REPORT #
9. PERFORMING ORGANIZATION NAME AND ADDRESS George C. Marshall Space Flight Center Marshall Space Flight Center, Alabama 35812		10. WORK UNIT NO.
		11. CONTRACT OR GRANT NO.
		13. TYPE OF REPORT & PERIOD COVERED Conference Publication
12. SPONSORING AGENCY NAME AND ADDRESS National Aeronautics and Space Administration Washington, D. C. 20546		
		14. SPONSORING AGENCY CODE

15. SUPPLEMENTARY NOTES

Prepared by Space Sciences Laboratory, Science and Engineering Directorate

16. ABSTRACT

This report summarizes the results of a Float Zone Workshop held at the Marshall Space Flight Center, December 12, 1980. The report consists of four major sections: (1) an introduction, (2) a summary of the Analytical Float Zone Experiment System (AFZES) concept and the types of experiments being considered for such a facility, (3) reports from various industrial producers and users of float zone material, and (4) a summary of the conclusions from the workshop.

17. KEY WORDS Float zone material Materials processing in space	18. DISTRIBUTION STATEMENT Unclassified — Unlimited

19. SECURITY CLASSIF. (of this report) Unclassified	20. SECURITY CLASSIF. (of this page) Unclassified	21. NO. OF PAGES 178	22. PRICE NTIS

MSFC - Form 3292 (Rev. December 1972) For sale by National Technical Information Service, Springfield, Virginia 22151

PREFACE

A Float Zone Workshop was held at MSFC on December 12, 1980. The plan for this workshop was to bring the investigators formulating the NASA concept of an Analytical Float Zone Experiment System (AFZES) together with representatives from industry involved in commercial processes. The purpose was to examine the relevance of some of the experiments being considered for the AFZES to industrial users. Also, since budgetary constraints require a substantial descoping of the presently envisioned AFZES, it has been necessary to reevaluate the types of experiments that can be accomplished and possibly to restructure the effort to include investigations that are more directly related to industrial needs.

The workshop was structured into two parts. The first part consisted of a summary by the existing NASA study team of the AFZES concept and the types of experiments being considered for such a facility. The second part consisted of reports from various industrial producers and users of float zone material. This was followed by a round table discussion comparing and contrasting the NASA program with industrial problems to determine what restructuring may be desirable in the approach taken by NASA.

The list of attendees and an agenda are given in Tables 1 and 2.

TABLE 1. ATTENDANCE LIST FOR FLOAT ZONE WORKSHOP - 12/12/80

Dr. J. Carruthers
EM-7
NASA Headquarters
Washington, DC 20546
(202) 755-8614

Dr. Ted Ciszek
Photovoltaics Research Branch
SERI
Bldg 16, First Floor
1617 Cole Boulevard
Golden, CO 80401
(303) 231-1769

Dr. Creed Clayton
Semtec, Inc.
500 Wynn Drive
Huntsville, AL 35805
(205) 830-0430

Dr. Arthur A. Fowle
Arthur D. Little, Inc.
25 Acorn Park
Cambridge, MA 02140
(617) 253-864-5770

Dr. Gerald Gill
Westech Systems, Inc.
4225 South 37th Street
Phoenix, AZ 85040
(602) 276-4261

Dr. Jim Hendrick
Rockwell
Rocketdyne Division
6633 Canoga Avenue
Canoga Park, CA 91304
(213) 922-4884

Dr. George Homsy
Department of Chemical Engineering
Stanford University
Stanford, CA 94305
(415) 497-4906

Dr. Lubek Jastrzebski
RCA
Princeton, NJ 08540
(603) 734-2655

Dr. Jasuhiro Kamontani
Case Western Reserve University
Cleveland, OH 44106
(216) 368-4580

Dr. E. L. Kern
Hughes Carlsbad
Carlsbad, CA 92008
(714) 438-9191

Dr. K. M. Kim
Dept., 267, 13, 300-40E
IBM East Fishkill Labs
Hopewell Junction, NY 12533
(914) 897-6627

Dr. Jack Kropp
TRW
One Space Park
Redondo Beach, CA 90278
(213) 536-3021

Dr. J. Adin Mann
Case Western Reserve University
Cleveland, OH 44106
(216) 368-4150

Dr. John Manning
NBS
Washington, DC 20234
(301) 921-3354

Dr. W. A. Oran
EM-7
NASA Headquarters
Washington, DC 20546
(202) 755-8610

Dr. Simon Ostrach
Case Western Reserve University
Cleveland, OH 44106
(216) 368-2940

Dr. Guy E. Rindone
201 Steidle Building
Pennsylvania State University
University Park, PA 16802
(814) 865-6932

TABLE 1. (Concluded)

Dr. Robert M. Sandfort
Monsanto Co.
St. Peters, MO   63376
(314) 272-6281

Dr. Lawrence Spradley
Lockheed - Huntsville Research
  and Engineering Center
P.O. Box 1103
Huntsville, AL   35807
(205) 837-1800

Dr. L. R. Testardi
EM-7
NASA Headquarters
Washington, DC   20546
(202) 755-8614

Dr. John Verhoeven
126 Metallurgy Building
Iowa State University
Ames, IA   50011
(515) 294-5900

Dr. Donald Waltz
TRW
One Space Park
Redondo Beach, CA   90278
(213) 536-4745

Dr. William Wilcox
Department of Chemical Engineering
Clarkson College of Technology
Potsdam, NY   13676
(315) 268-6650

Dr. August Witt
MIT
Cambridge, MA   02139
(617) 253-5303

NASA/MSFC
Marshall Space Flight Center, AL   35812 :

Ms. Wendy S. Alter, ES72

Ms. Barbara Askins, ES72

Ms. Ernestine Cothran, ES72

Mr. Sam Lowry, ES72

Dr. C. A. Lundquist, ES01

Mr. Gene McKannan, LA01

Dr. Robert J. Naumann, ES71

Mr. Charles F. Schafer, ES82

Mr. David A. Schaffer, LA11

Mr. J. R. Williams, LA11

Mr. L. K. Zoller, LA01

Mr. J. M. Zwiener, ES72 .

TABLE 2. AGENDA

FLOAT ZONE WORKSHOP
MARSHALL SPACE FLIGHT CENTER
SPACE SCIENCES LABORATORY
BUILDING 4481, ROOM 107

December 12, 1980

Introduction	J. Carruthers	8:00 - 8:30
Review of NASA's Activities in the Float Zone Program	A. Fowle J. Mann S. Ostrach J. Verhoeven G. Homsy	8:30 - 10:30
Industrial Aspects of Float Zone Crystal Growth	T. Kern T. Ciszek R. Sandfort G. Gill W. Wilcox L. Jastrzebski K. Kim	10:30 - 12:30
Lunch and Discussion		12:30 - 1:30
Wrap-Up Discussion		1:30 - 2:30

TABLE OF CONTENTS

TABLE OF CONTENTS (Concluded)

I. INTRODUCTION

J. R. Carruthers

Dr. J. R. Carruthers, Program Director, set the stage for the meeting with his introductory comments. He reviewed the rationale and objectives of the Materials Processing in Space program. He gave a general overview of the problems in controlling the growth of single crystalline material in the float zone process and described how various chemical inhomogeneities and crystalline defects are influenced by the processing parameters. Parameters of interest are: temperature profiles, forced and natural convection, growth rate, melt composition, interface shape, melt/meniscus shape and overall melt shape and volume. The elimination of gravity should provide a new dimension of control over some of these parameters by removing buoyancy-driven convection and hydrostatic pressure. This could result in a better capability for growing uniformly doped crystals by maintaining diffusion-controlled compositional profiles and by eliminating certain growth rate fluctuations believed to be related to convective effects. The absence of hydrostatic pressure allows the extension of the float zone process to systems that possess insufficient surface tension to maintain useful zone dimensions in Earth's gravity. Also, considerable freedom exists for configuring the shape of floating zones to vary the surface to volume ratio in order to obtain better purification, to establish more planar isotherms, to obtain flatter interfaces, to establish higher thermal gradients for better control of compositional supercooling, or to extend the region of coupled growth in solidification of certain alloys.

Dr. Carruthers presented some background to the floating zone stability problem, including the use of neutral density immiscible liquids to model the process (Plateau technique) and the Skylab floating zone demonstration. He outlined the recent experiments conducted in this country and in Europe and described the ESA-sponsored floating zone experiments being developed for the first Spacelab mission.

Finally, Dr. Carruthers discussed the budgetary constraints and the need to reconsider the present direction of the program. An attempt to include the Analytical Float Zone Experiment System (AFZES) in the FY 80 budget was unsuccessful . Approval was granted in FY 81, but the limited funding that might be available would effectively delay any major action and would have to be deferred until 1982. Also, the cost estimates of the AFZES as defined in the recent A. D. Little phase B study are already substantially larger than the program can afford, and there are increasing congressional concerns over the large cost growths in other programs. For these reasons, Dr. Carruthers announced a new policy to be applied to this and related programs. This policy emphasizes ground-based research to establish the rationale and background needed for space experiments, to explore alternative approaches, to identify requirements for flight apparatus, to explore process

automation to minimize or eliminate crew involvement, and to identify and breadboard technology drivers. The use of existing facilities will be explored together with specialized but vastly simplified experiment packages to obtain early flight data utilizing Shuttle mid-deck capabilities. A major dedicated facility will not be undertaken until the rationale, scientific requirements, and required technology are well in hand. In the case of the float zone effort, Dr. Carruthers stated that he sees the need to expand the scientific working group activities and to involve industrial participation, particularly those industries involved in producing intrinsic and extrinsic infrared detector material. He then announced that Dr. Ted Kern, Hughes Aircraft Corporation, would help NASA organize and direct this expanded scientific working group.

II.   REVIEW OF NASA-SPONSORED EFFORTS IN THE
DEVELOPMENT OF THE AFZES

SCIENCE REQUIREMENTS WORKING GROUP (SRWG) IN FLOAT ZONE MATERIALS PROCESSING IN SPACE: A REVIEW

Arthur A. Fowle

A summary and history of the Float Zone Working Group was presented by its chairman, Dr. Arthur A. Fowle. This group was established at NASA's request in early 1978. The functions of this working group are to: provide an informal forum of scientific investigators for the exchange of information and ideas in the approach to the solution of common problems in float zone processing, help plan the research and development necessary to place the float zone process on a firm base of scientific understanding and advanced technological development, establish the science requirements for the AFZES for Spacelab, and seek ways to maximize the advantages of the space environment in the pursuit of these goals.

The membership consists of funded investigators and colleagues with scientific interest in the float zone process. The current members are shown in Table 1.

The working group's first task was to prepare and submit to NASA a 4-year plan for research and development leading to a set of flight experiments to be conducted in the AFZES. Such a plan was submitted in February 1979. This plan called for a comprehensive theoretical development of models which accurately predict the velocity, temperature, and compositional fields and for a major development in instrumental techniques for measuring thermophysical properties and flow fields in the floating zone. Specifically, it is desired to:

1. Determine surface tension as a function of temperature and composition.

2. Directly measure surface tension gradients in response to imposed temperature and composition gradients.

3. Detect insoluble surface films and surface phase behavior.

4. Measure volume and surface flows.

5. Measure volume and surface temperatures.

6. Determine minority constituents in solid and liquid phases.

7. Determine other thermophysical and optical properties (e.g., coefficient of thermal expansion, emissivity, etc.).

The working group also assisted in the development of the science requirements for the AFZES study and formally approved the final science requirements in September 1979. The preliminary specifications

5

TABLE 1. SCIENCE REQUIREMENTS WORKING GROUP ON FLOAT ZONE MATERIALS PROCESSING IN SPACE

Dr. Arthur A. Fowle (Chairman)
Arthur D. Little, Inc.
20 Acorn Park
Cambridge, MA 02140

Dr. Roger K. Crouch
Code 473
NASA/Langley Research Center
Hampton, VA 23665

Dr. Edward Gertner
Rockwell International Science
    Center
1049 Camino Dos Rios
Thousand Oaks, CA 91360

Dr. Lubek Jastrezebski
David Sarno Research Center
Princeton, NJ 08540

Dr. J. Adin Mann, Jr.
Chemical Engineering Department
Case Western Reserve University
University Circle
Cleveland, OH 44106

Dr. Simon Ostrach
Division of Fluid, Thermal and
    Aerospace Science
Case Western Reserve University
University Circle
Cleveland, OH 44106

Dr. John D. Verhoeven
126 Metallurgy Building
Iowa State University
Ames, IA 50011

Dr. Robert A. Brown
Department of Chemical
    Engineering
Massachusetts Institute
    of Technology
Cambridge, MA 02139

Dr. Steven Davis
Department of Engineering
    Science and Applied Math.
Northwestern University
Evanston, IL 60301

Dr. George Homsy
Department of Chemical
    Engineering
Stanford University
Stanford, CA 94305

Dr. K. M. Kim
Department 267, 13, 300-40E
IBM East Fishkill Labora-
    tories
Hopewell Junction, NY 12533

Dr. John Manning
Metallurgy Division
National Bureau of Standards
Washington, DC 20234

Dr. L. E. Scriven
Department of Chemical
    Engineering and
    Materials Science
University of Minnesota
151 Chemical Engineering
421 Washington Avenue, SE
Minneapolis, MN 55455

Dr. August F. Witt
Department of Material
    Science
Massachusetts Institute of
    Technology
Cambridge, MA 02139

for the AFZES are given in Table 2. A conceptual design is shown in Figure 1, with details shown in Figure 2.
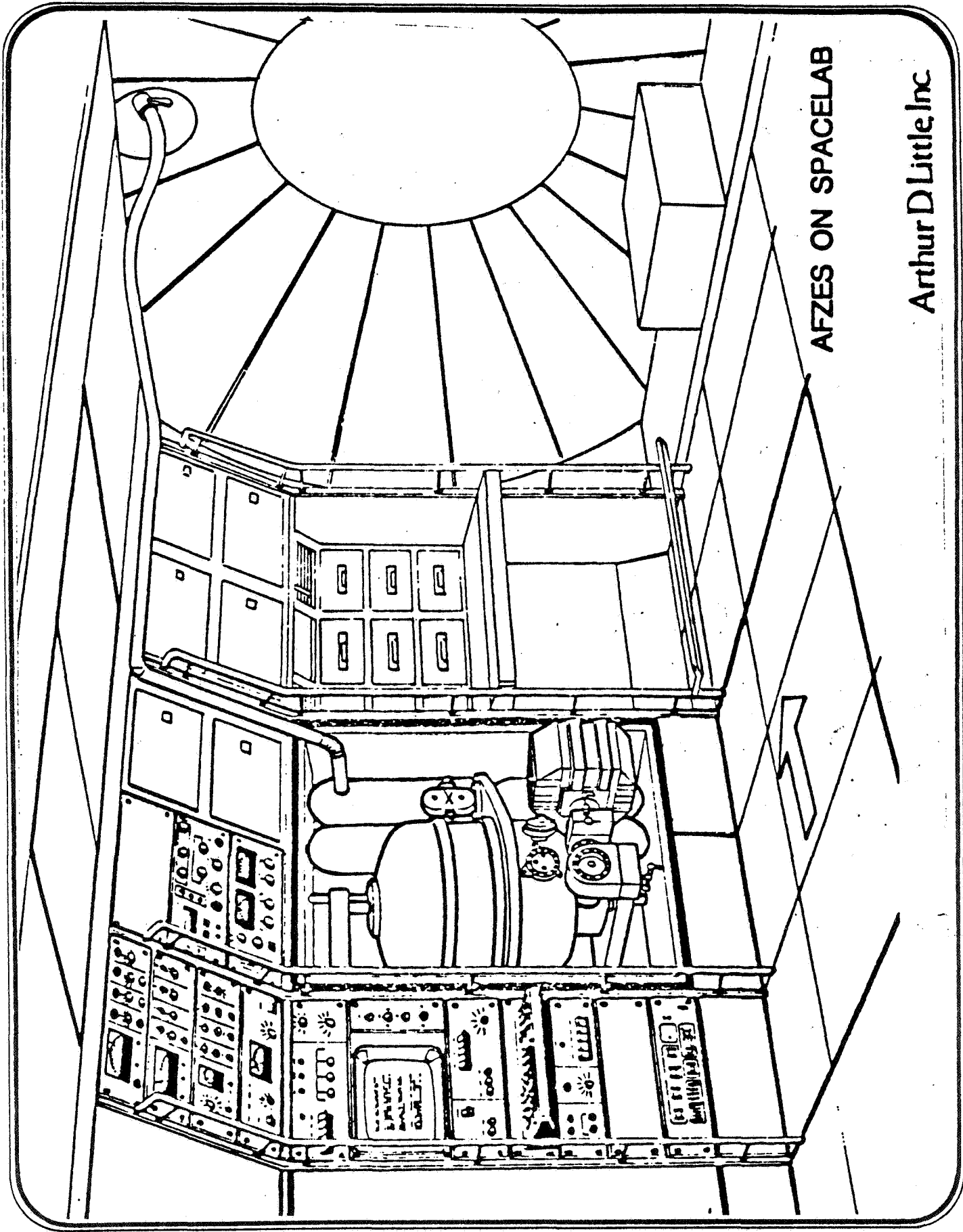
In his perspective, Dr. Fowle believed that the theoretical work was in expert hands and had perhaps advanced beyond the support of available thermophysical data and experimental techniques. However, he pointed out that no adequate velocity or temperature measurement techniques are yet available; properties of liquid metal surfaces, detection of insoluble surface films and surface phase behavior have barely been touched; and no work has been done to develop the advanced characterization techniques needed for the growth of the crystals. The apparatus conceived for the AFZES would be generally useful for ground-based, float zone experimentation in a preliminary design phase.

In summary, Dr. Fowle stated that a good start had been made but much needed to be done. The emphasis should be on the development of measuring techniques and on obtaining thermophysical properties of metal films to support the theoretical efforts. He would like to see more involvement of industrial users and processors of electronic materials (i.e., semiconductors) but pointed out that uncertainties regarding scope and continuity of NASA programs strain the commitment of the competent community of scientists and engineers working on the effort.

TABLE 2.   ANALYTICAL FLOAT ZONE EXPERIMENT SYSTEM (AFZES) FOR SPACELAB

(Preliminary Design, Per Performance Specifications,
29 February 1980)

● DOUBLE RACKS ON SPACELAB

● TOTAL WEIGHT = 549 KG; MAXIMUM TOTAL POWER = 1290 W

● SAMPLE HEATER: 8 QUARTZ-HALOGEN LAMPS WITH PARTIAL-ELLIPSOIDAL
  REFLECTORS (550 W)

● SAMPLE SIZE: APPROXIMATELY 0.5 to 3.0 CM

● SAMPLE TEMPERATURE: APPROXIMATELY 300 - 1200°C

● SAMPLE MANIPULATION IN AXIAL AND ROTATIONAL DIRECTIONS

● SURFACE VELOCITY SCAN BY LDV

● SURFACE TEMPERATURE SCAN BY RADIATION PYROMETER

● SAMPLE ENVIRONMENT: VERY HIGH VACUUM, INERT GAS, CONTROLLED
  GAS COMPOSITION

● OTHER INSTRUMENTS: GAS ANALYZER, AUGER, ION BEAM

● PRIMARY DESIGN FEATURE: FLEXIBLE, MODULAR CONSTRUCTION

AFZES ON SPACELAB
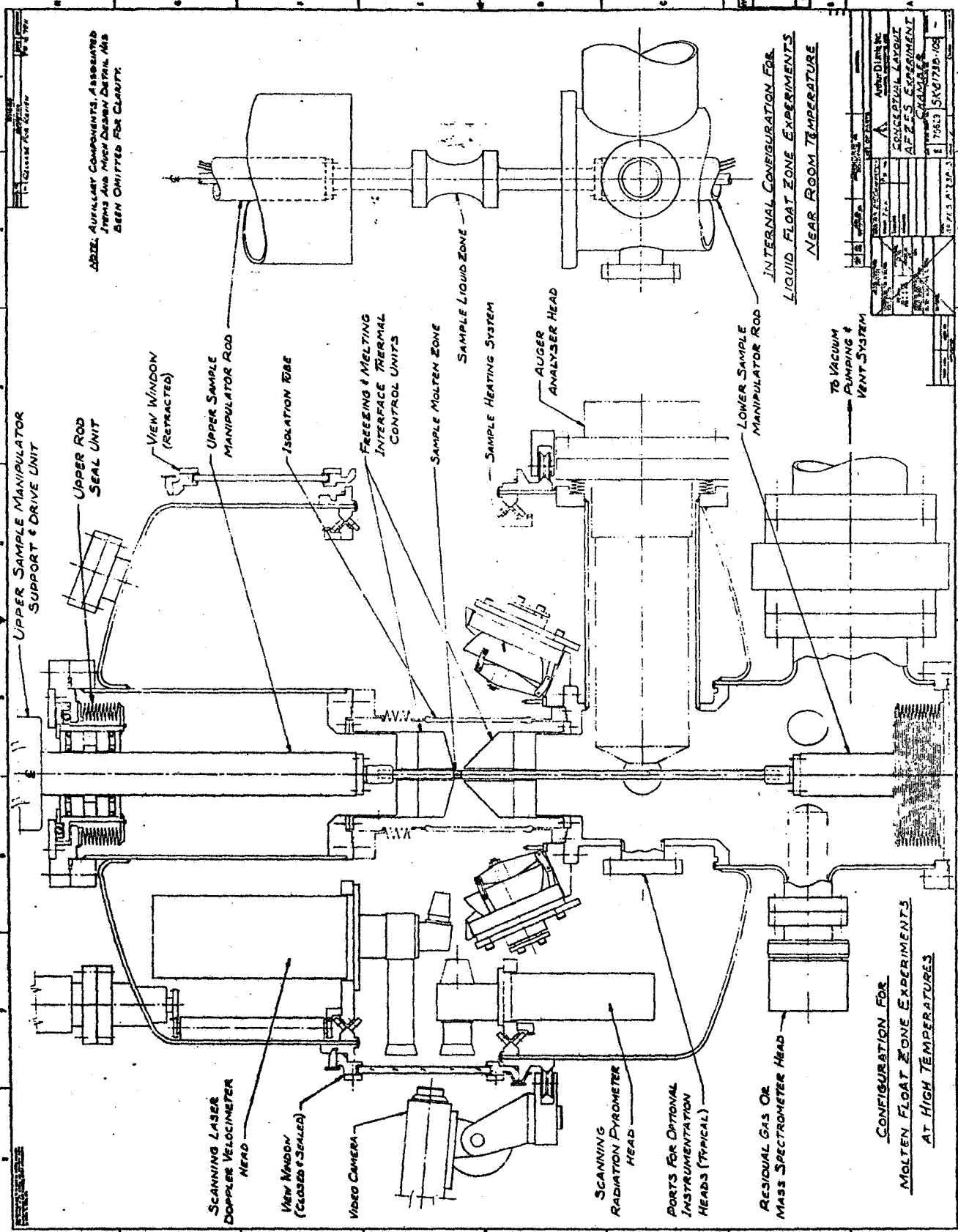
Arthur D Little Inc

FIGURE 1

FIGURE 2

Upper Sample Manipulator Support & Drive Unit

Upper Rod Seal Unit

View Window (Retracted)

Upper Sample Manipulator Rod

Isolation Tube

Freezing & Melting Interface Thermal Control Units

Sample Molten Zone

Sample Liquid Zone

Sample Heating System

Auger Analyser Head

Lower Sample Manipulator Rod

To Vacuum Pumping & Vent System

Internal Configuration For Liquid Float Zone Experiments Near Room Temperature

Scanning Laser Doppler Velocimeter Head

View Window (Closed & Sealed)

Video Camera

Scanning Radiation Pyrometer Head

Ports For Optional Instrumentation Heads (Typical)

Residual Gas Or Mass Spectrometer Head

Configuration For Molten Float Zone Experiments At High Temperatures

Note: Auxiliary Components, Associated Items And Much Design Detail Has Been Omitted For Clarity.

10

SURFACE TENSION-DRIVEN CONVECTION PHENOMENA

J. Mann

Professor J. Mann, Case Western Reserve University, reported on the techniques his group is developing for measuring surface tension-driven flow. In addition to the fairly standard crossed beam LDV method, this group is working on methods using ripplon scattering[1] which do not require "seeding" of the fluid and can also be used to determine thermophysical properties of the surface, such as surface tension, viscosity, and local temperature. This technique was utilized by L. B. Shih in her dissertation (see Appendix) to observe the change in surface tension associated with the nematic to isotropic phase transition of para-azoxydianisole at 134°C.

The ripplon scattering methods become difficult for surface velocities below 1 mm/sec because of the overlapping spectra. Careful analysis procedures could extend this to smaller flows, but the more conventional LDV techniques with seeded flows are the method of choice for slow flows. These can be employed to measure flows below 0.1 mm/sec.

Two papers[2] by R. S. Sirohi, R. V. Edwards and J. A. Mann were summarized by Professor Mann. The first paper dealt with the use of grating heterodyne spectroscopy to analyze ripplon scattering to determine the visco-elastic properties of the liquid interface.

The experimental setup is shown in Figure 1. The operation of the grating heterodyne apparatus is as follows: A beam of light incident at the liquid surface is scattered by thermally excited capillary waves (ripplons). Just above the surface there are specularly reflected and scattered fields; the scattered field is easily detectable in a very narrow angular range about the specularly reflected beam. The scattered irradiance falls as $1/|\sin\theta - \sin\theta_{scatt}|^2$, where the angles are computed from the normal to the surface. The reflected and scattered fields pass through a grating which is designed for high transmittance. Therefore, the scattered field is assumed to propagate unattenuated, but the specularly reflected beam suffers diffraction. Various orders thus produced propagate in well-defined directions, and a lens brings the diffracted field to focus at its focal plane where one spot is observed for each order. If, for example, the grating is parallel to the liquid surface and is located very near to it, the component of the scattered field from surface ripplons characterized by

---

1. By "ripplon scattering" we mean the scattering of light from thermally excited capillary waves.

2. Drafts of two papers are included in the Appendix. The first paper has been accepted in revised form by J. Applied Optics. The second has been submitted to J. Applied Physics.

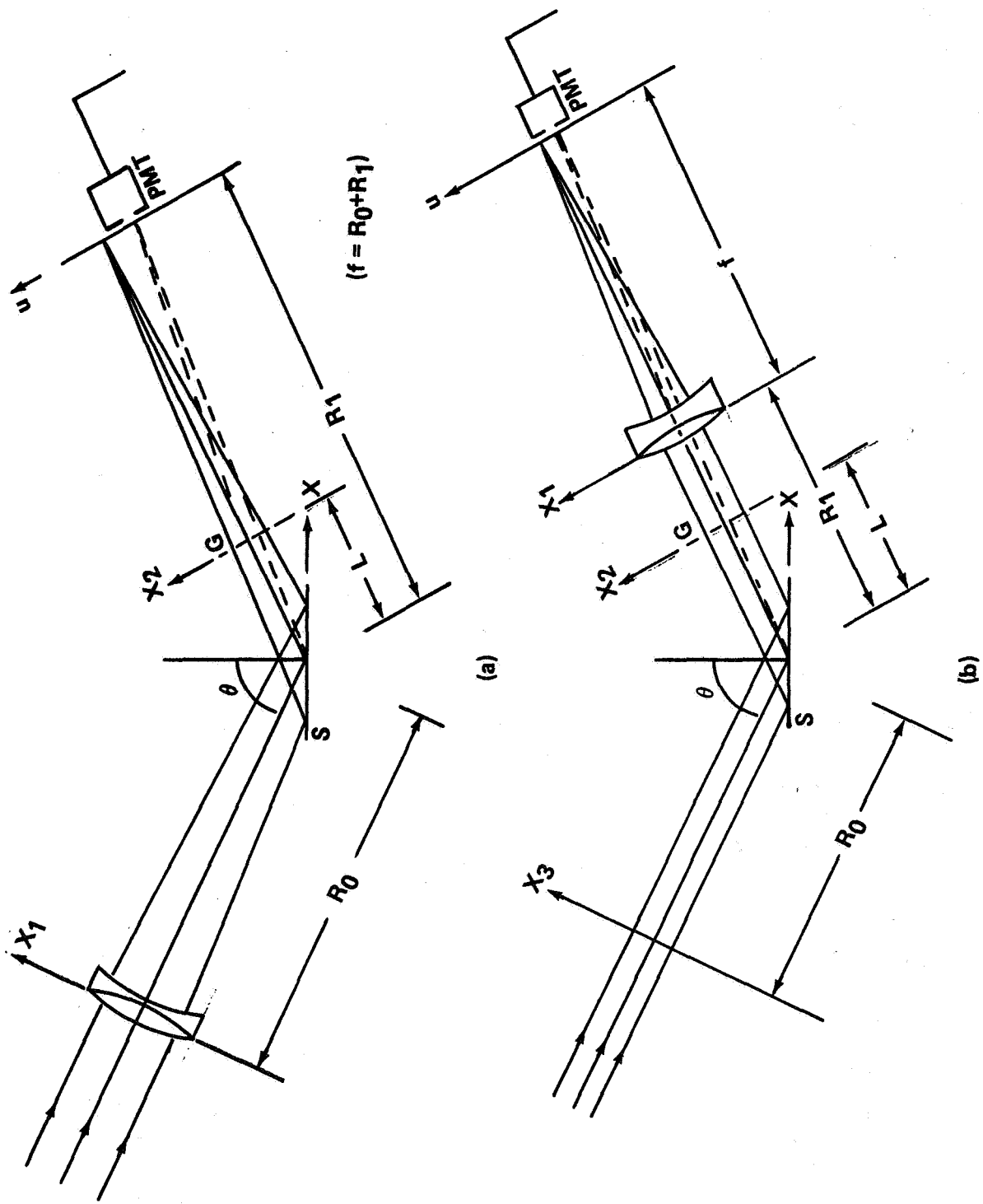(a)

$(f = R_0 + R_1)$

(b)

Figure 1. Schematics of the experimental setup for heterodyne apparatus.

the same wave vector as that of the grating will propagate in the same direction and will completely superpose on the focal plane because the focal spots will be of identical sizes. If a photodetector is placed at the focal plane, photomixing takes place. To minimize the effect of homodyne, the local oscillator beam is stronger by many orders of magnitude than the ripplon scattered field.

The experimental parameters of interest are the center frequency ω_0 and the width Γ_1 of the power spectrum of the photocurrent. These are related to the physical properties of the scattering material, i.e., the surface tension, density ρ and viscosity η, by the dispersion relationships

$$\omega_0 = (\frac{\alpha y_1}{\rho})(K_0 \cos \theta)^{3/2}$$

and

$$\Gamma_1 = \frac{2 \eta K_0^2 \cos^2 \theta}{\rho} \quad ,$$

where y_1 is a dimensionless group involving bulk and surface properties that range from 0.95 to 1.05 for most materials, and K_0 is the ripplon wave number.

The power spectrum was obtained for H_2O and C_2H_5OH using 400-point autocorrelation functions shifted by 10 μsec. This was converted to a power spectrum by a 256-point digital Fourier transform with a step of 195.31 Hz. Other pertinent data are $\theta = 7.2°$, $K_0 = 247$ cm^{-1}. The results are shown in Figures 2 and 3. By appropriate fitting techniques, ω_0 was found to be 20322 rad/sec and $\Gamma_1 = 1841$ rad/sec for ethanol. From these data, $\alpha = 22.16$ dyne/cm and $\eta = 0.0121$ poise. As a further check, the spectra were computed for the measured values of α and η. As may be seen from the figures, the comparison is excellent except for the low frequency edge. This discrepancy is probably caused by the presence of nonwhite noise in the system. Similar results were obtained for H_2O.

The second paper reviewed by Professor Mann extended the ripplon measurement technique to obtain surface velocities. In a sense, the ripplons act as tracer particles for following the surface velocity field. Since they are confined to the surface, they provide a better representation of the surface velocity than seeded particles.

The ripplons may be thought of as waves propagating in random directions generated by local thermal fluctuations in the surface profile. If we consider the propagation of waves along the x direction, on the average, equal numbers of ripplons will cross any line in the surface $x = x_1$ at any instant of time from both positive and negative x directions. If the interface is translated along the positive x
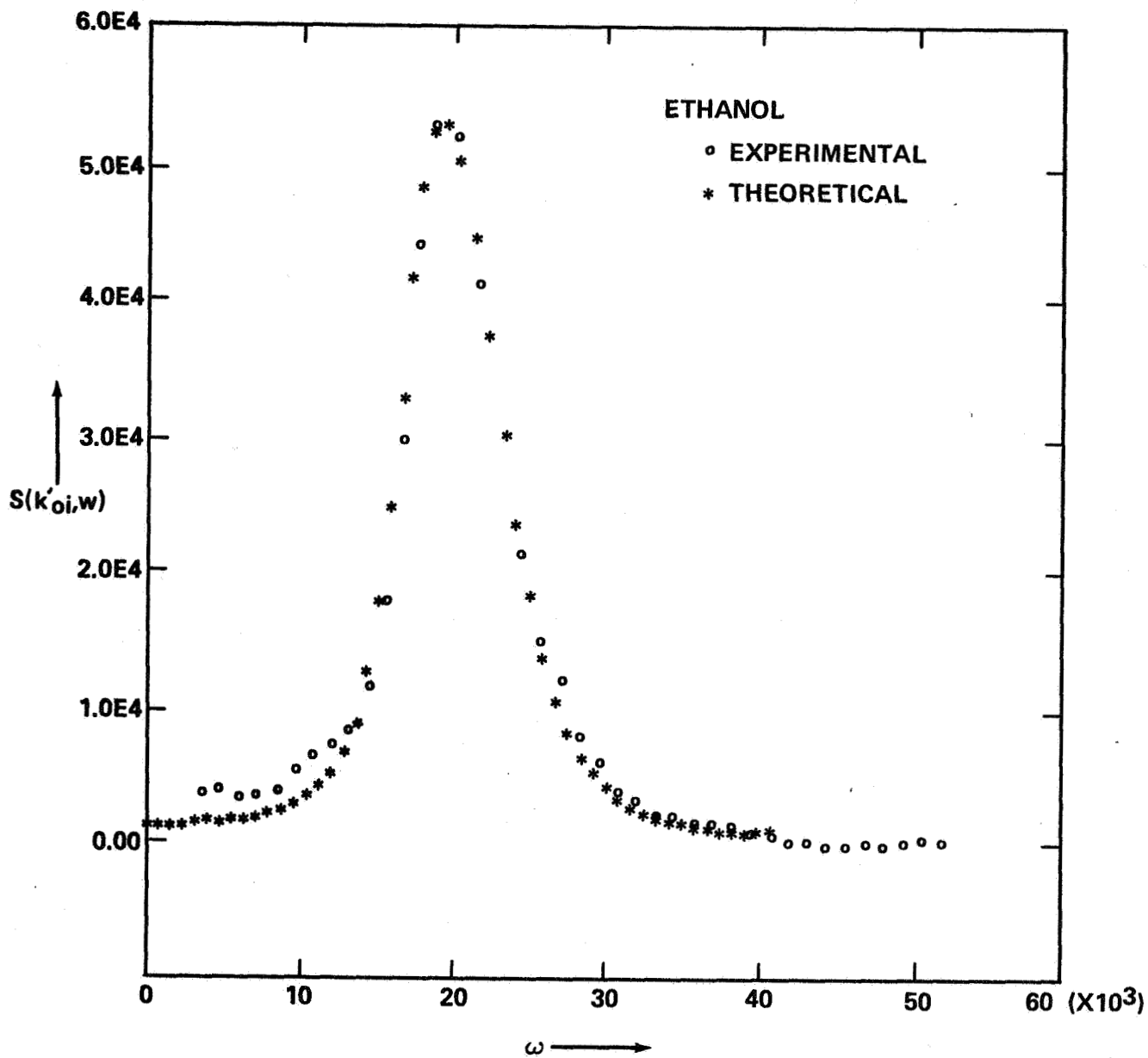
13

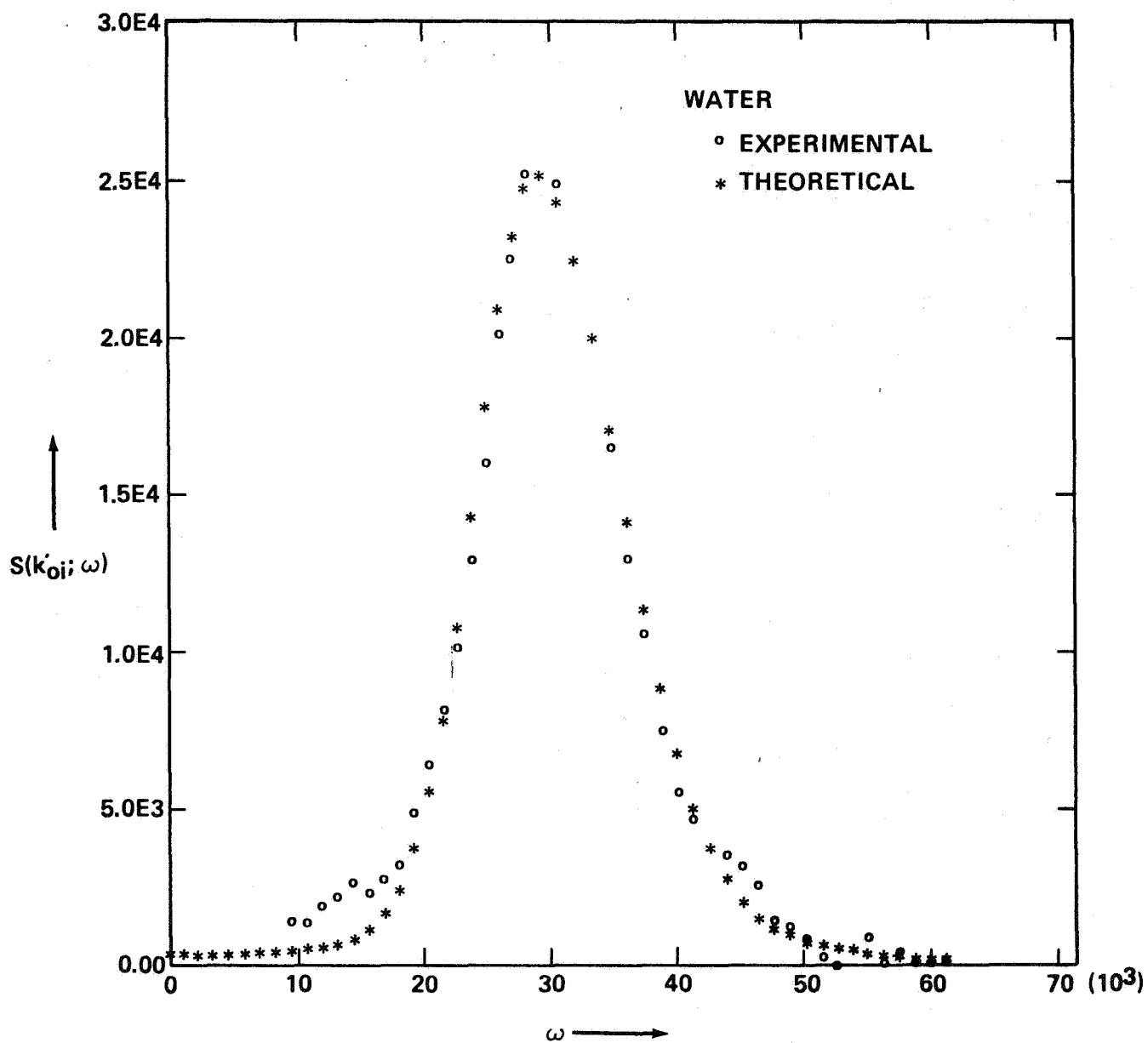Figure 2. Experimental and theoretical spectra for ethanol.

Figure 3. Experimental and theoretical spectra for water.

direction with a velocity v, the frequency of ripplons propagating along the positive x direction is increased by $K_0 v$, while that of those propagating along the negative x direction is decreased by the same amount. The power spectrum of the photocurrent thus exhibits two peaks situated at $\omega = \omega_0 \pm K_0 v$. A detailed mathematical analysis leads to a modified dispersion equation

$$\left(\omega \pm K_0 v\right)^2 = y_1 \frac{v}{\rho} K_0^{\;3} \quad .$$

This equation has two roots at $\omega = \omega_0 \pm K_0 v$. It can be shown that the study of the field scattered from a moving interface can be used to extract surface velocity information. It is known that the field scattered by ripplons is mostly concentrated in a very narrow angular range about the specularly reflected beam and, hence, relatively coarse gratings ($Kg < 1000$ cm^{-1}) are employed in practice. A measurable frequency shift can be obtained from a relatively fast moving interface, > 1 cm/sec. For lower velocities, the two peaks may not be resolved. The velocity information is contained in the shape of the spectrum. Careful analysis can extract the velocity information for surface flows less than 1 cm/sec. The basic restriction on slower flows is the concerted influence of instrumental broadening and natural broadening of the power spectrum. Also, the use of a grating with a higher spatial frequency will reduce the broadening and allow the measurement of slower velocities.

To confirm the theory, experiments were conducted on the surface of ethanol. A circular disk 30 cm in diameter containing ethanol was rotated slowly (6 sec per revolution) and the laser beam was reflected off the surface at various distances from the center of rotation. A grating of $K_g = 247$ cm^{-1} was used, and the beam was incident at an angle of $24.8°$, giving an effective K_0 of 224.8 cm^{-1}.

The measurements are made at various locations on the surface of ethanol in the rotating disk. The original data were again obtained as 400-point autocorrelation functions. These were then converted to 256-point spectra by digital Fourier transform methods. Figure 4 shows the spectrum from the stationary ethanol surface. Figure 5 shows the spectrum obtained by shining the laser beam at a location where the mean velocity was 5.5 cm/sec. The spectrum is not resolved and appears identical in shape to that of Figure 4 except for the increased width. However, when the mean velocity is 9.5 cm/sec, the spectrum is well resolved with the frequency separation between the two peaks of 635 Hz. This spectrum is shown in Figure 6. The theoretical spectra are computed and plotted in Figures 4 through 6 for the sake of comparison. There is an excellent fit between experimental and theoretical spectra.

Figure 7 shows the plot between the separation of resolved peaks and the distance of the measurement region from the center of rotation.
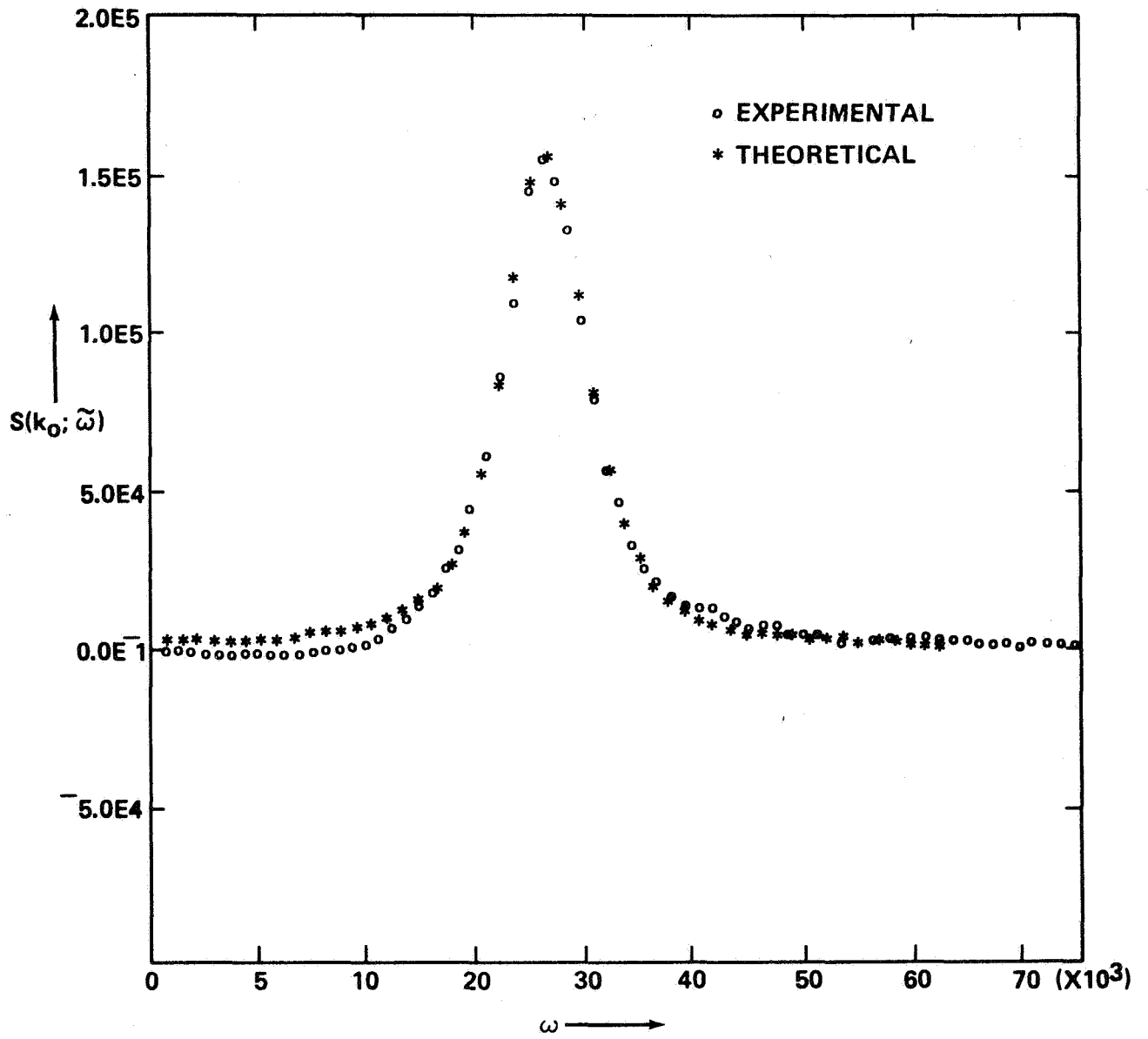
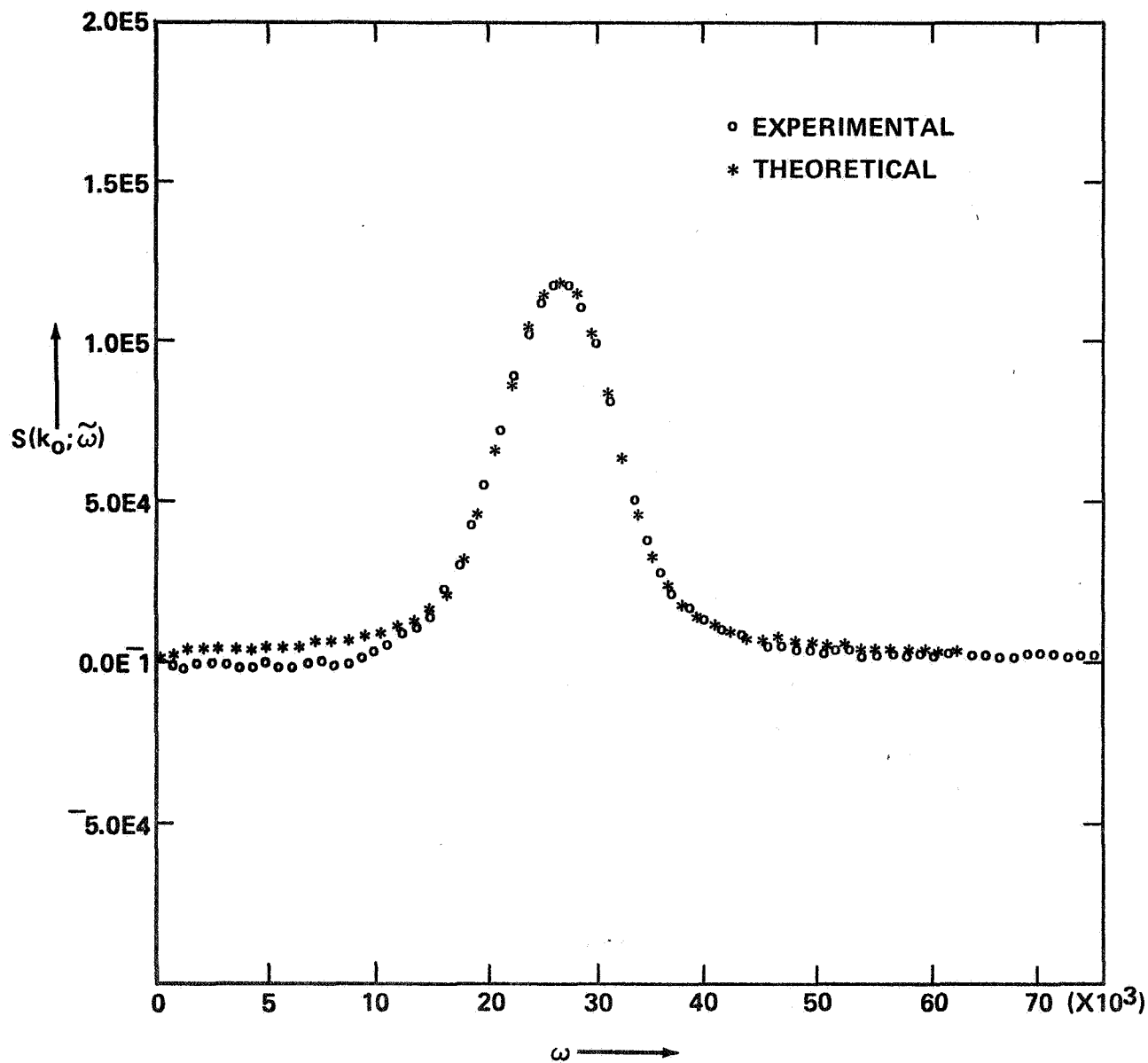Figure 4. Power spectrum from stationary ethanol surface.

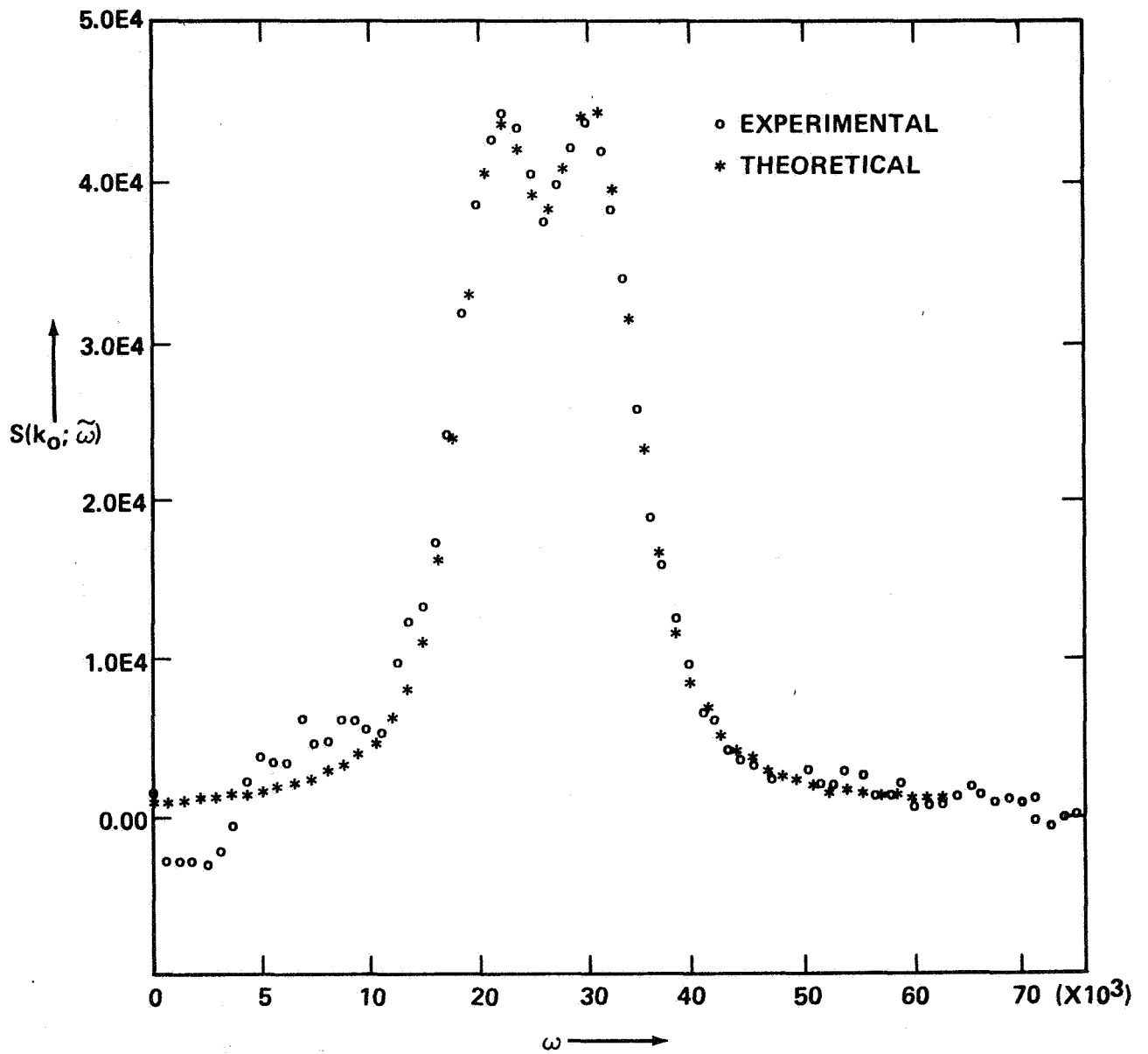Figure 5. Power spectrum from ethanol surface moving at 5.5 cm/sec.

Figure 6. Power spectrum from ethanol surface moving at 9.5 cm/sec.
Note that now the two peaks are resolved with
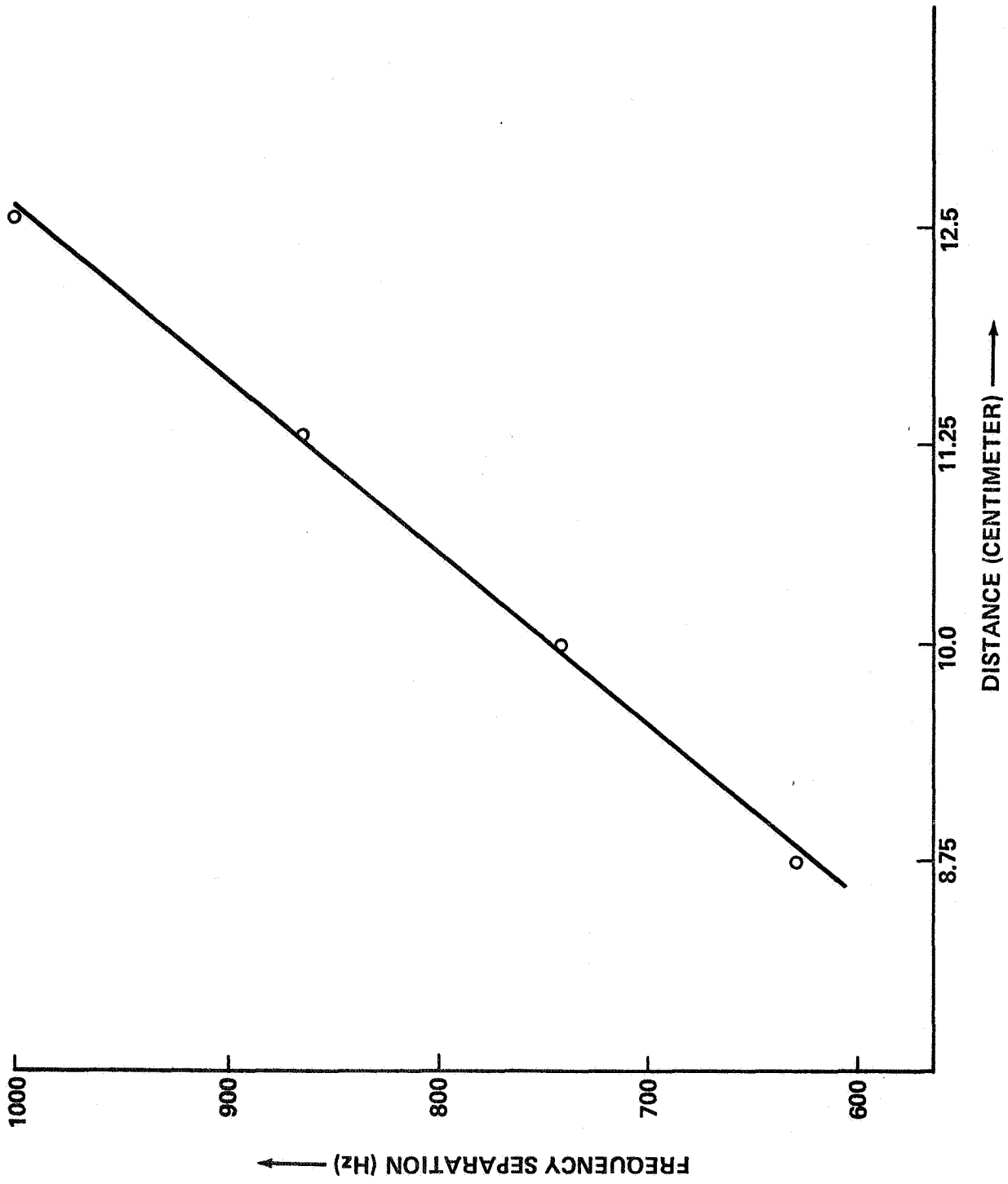a separation of 635 Hz.

19

Figure 7. Frequency separation versus radius of rotating surface.

The measurements were made at distances of 5, 8.75, 10, 11.25, and 12.5 cm from the center of rotation. The spectrum corresponding to the measurement at 5 cm is not resolved; however, however, the shape of the spectrum still contains the velocity information. The bars in Figure 7 represent the uncertainty of distance (or velocity) measurement due to the fat beam ($4\sigma \doteq 3$ mm) used in the measurement.

In summary, it may be concluded that surface flow velocities can be measured by studying the light scattered from the capillary waves on the moving interface. A nonlinear, least-squares procedure will be required in the analysis of the line shape of spectra obtained from slow flows. The experimental and theoretical understanding of the experiment is sufficient for this extension to be accomplished.

Dr. Mann is now ready to carry out the work with liquid gallium and extend the work to higher temperatures. The techniques developed by S. Hardy (NBS) will be used in handling and cleaning up the gallium. He expects to confirm some of Hardy's surface tension measurements as a function of temperature, although the major interest is in obtaining spectra as a function of the adsorbed species expected in a practical float zone system. Oxygen and carbon containing adsorbents will be studied at first. Surface visco-elastic parameters will be determined as a function of temperature. From these data it should be possible to predict whether the surface will tend to restrict temperature-driven flows under realistic operating conditions.

SURFACE TENSION-DRIVEN CONVECTIONS

S. Ostrach

A series of current theoretical and experimental work pertaining to surface tension-driven convection was described by Professor Ostrach.

Theoretical Work

The study of time-dependent flows generated by surface-tension gradients in thin liquid layers has been published.[1]

To proceed with studies of more general problems involving free surfaces it is essential to use the most general equations for the free-surface boundary conditions, particularly because in the float zone problem effects of rotation, internal flows, and surface tension must be considered. Thus, surface curvature, as distinct from surface deformation, must be accounted for. Since such complete formal boundary-condition equations are not available in the literature they were formulated. The dimensionless parameters associated with these equations are being derived for many situations of interest, e.g., predominant rotation coupled with thermocapillary flow and predominant thermocapillary flow coupled with rotation. In this way clarification will be obtained of the significance of dimensionless parameters, such as Crispation number, static Bond number capillary number, and Goucher number, which appear in the literature for special cases and are often confused. More importantly, this work will indicate explicitly the importance of the changes in the free-surface shapes. Since theoretical studies are considerably more difficult if the free-surface shape must be determined as part of the solution, it will be most helpful to know the conditions under which this complexity is unnecessary.

A new doctoral student has started to investigate numerical techniques for dealing with the complete float-zone process. In particular, he is looking at finite element methods with fast iterative procedures, using multipoint constraints and nonlinear optimization.

Experimental Work

A. The first set of experiments, performed by his graduate student, Sam Lowry,[2] consisted of observing the flows produced by heating a shallow pool of silicone oil from above by means of a hot wire (Fig. 1).

---

1. Pimputkar, S. M., and Ostrach, S.: Transient Thermocapillary Flow in Thin Liquid Layers, *Phys. Fluids*, Vol. 23, (7), 1281-1285, July 1980.

2. Mr. Lowry is now a visiting scientist at MSFC.
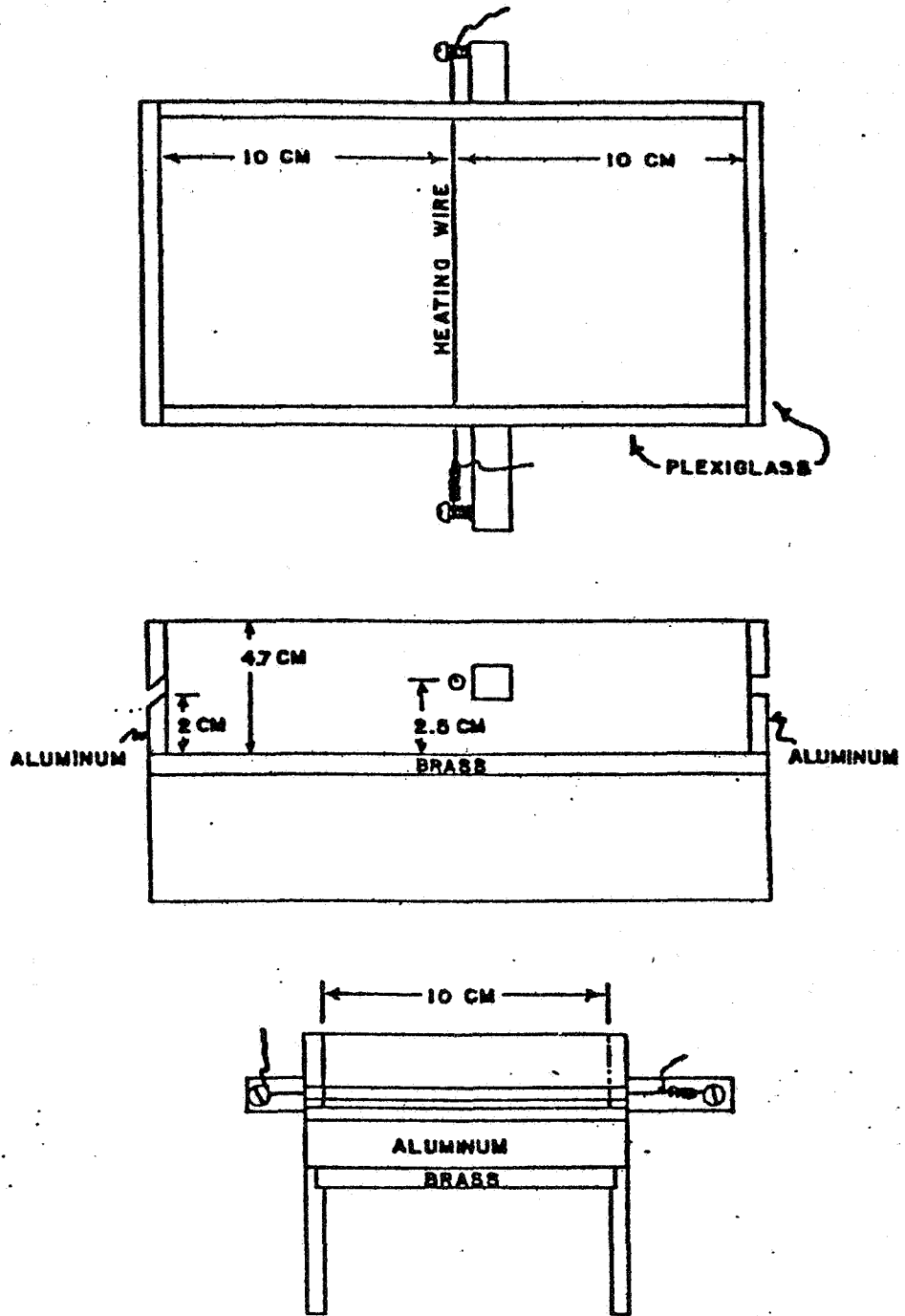
TEST. SECTION

Figure 1. Test apparatus for observing surface tension-driven convection.

The geometry was chosen to produce essentially a two-dimensional flow field with an imposed temperature gradient on the upper surface. Heating from above imposes a thermally stable vertical stratification which reduces the contribution of natural convection. Also, since the surface tension-driven flow is away from the hot wire, the resulting circulation pattern brings cooler fluid up from the bottom of the container in the vicinity of the wire. This tends to minimize the buoyancy-driven natural convection and, hopefully, allows surface tension-driven convection to dominate the flow field.

Velocity fields were obtained by use of tracer particles and LDV. Figure 2 is a time-lapse photograph showing the motion of tracer particles on the surface. Some distortion of the flow field from side walls is evident, but the flow near the center appears to be essentially two-dimensional. Figure 3 shows the flow field cross section.

The flow fields were computer modeled by Dr. Kamotani, assuming surface tension-driven flows only (0-g case), pure natural convection flows ($\sigma = 0$), and combined surface tension and natural convection. The results compared with experimental measurements at the surface are shown in Figure 4. As may be seen, there is fair agreement between experiment and theory, but for the case of silicone oil the flow is dominated by natural convection. Similar results are seen in Figure 5, which depicts velocity profile at various depths obtained using LDV techniques.

Because the effect of surface tension-driven flow was too small to be experimentally determined in the case of silicone oil, the experiments were repeated using FC-43 (an inert fluorocarbon). As may be seen in Figure 6, there is a considerable effect on surface temperature from surface-tension driven flow. The effect of additional surface flow is to transport heat away from the wire, thus reducing the thermal gradient. This is corroborated by the experimental measurements, although these show a lower than predicted overall temperature. This could result from the fact that the theory assumes adiabatic boundary conditions at the end wall when, in fact, the wall is a good conductor.

Figure 7 shows that significant differences can be expected between the depth profiles of the flow field with and without surface tension-driven flows. Again, the flow fields near the surface appear to be dominated by surface tension-driven flows. There appears to be a difference between experiment and theory, however, in the deep flow regime. Here the theory predicts a shallow return flow and a stagnant deep region. The experimental data show no evidence of this stratified flow but, instead, indicate a bulk return flow all the way to the bottom of the container. The boundary conditions in the experiment are not the same as in the calculations. This matter is being reinvestigated by Dr. Kamotani.
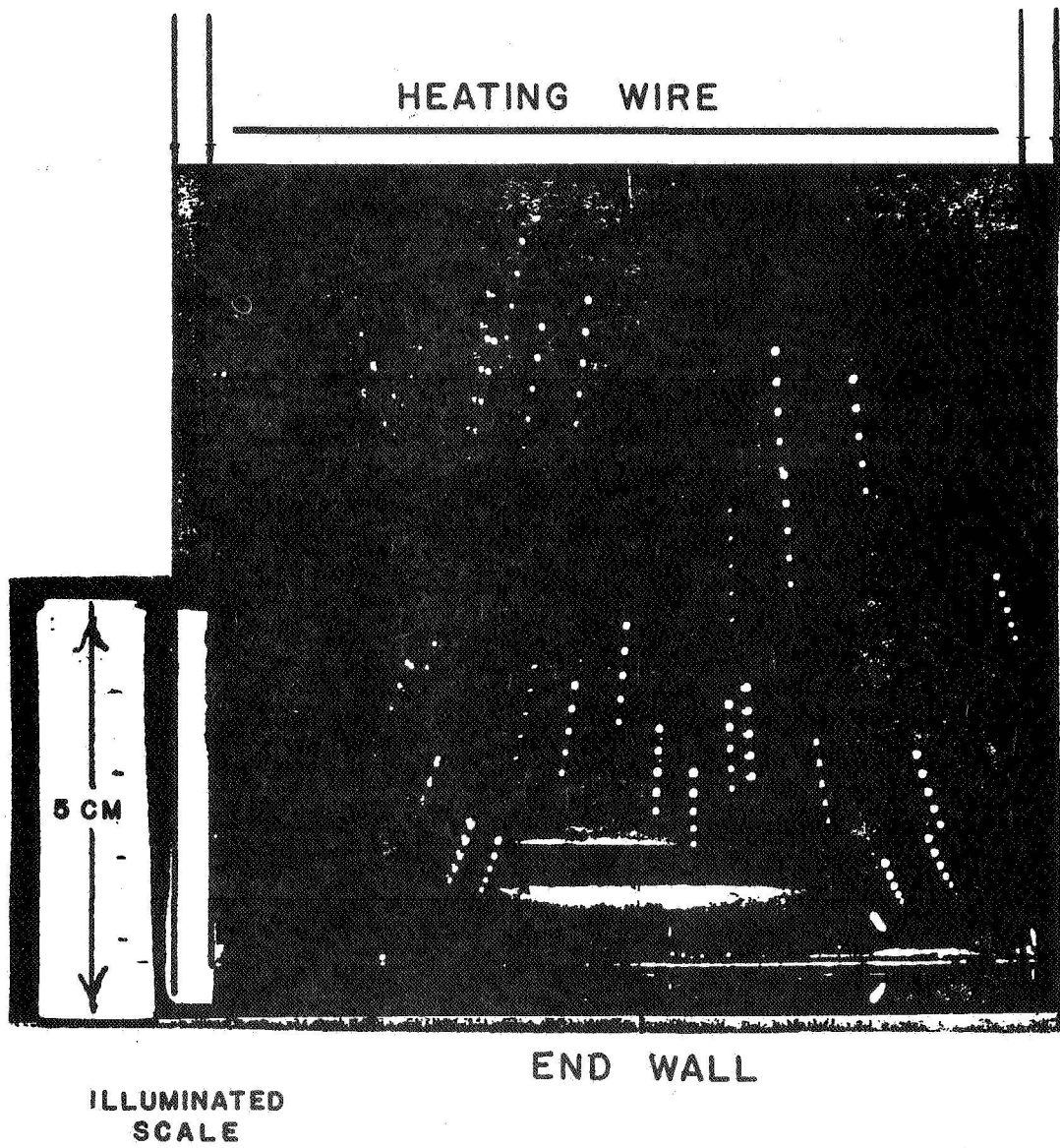
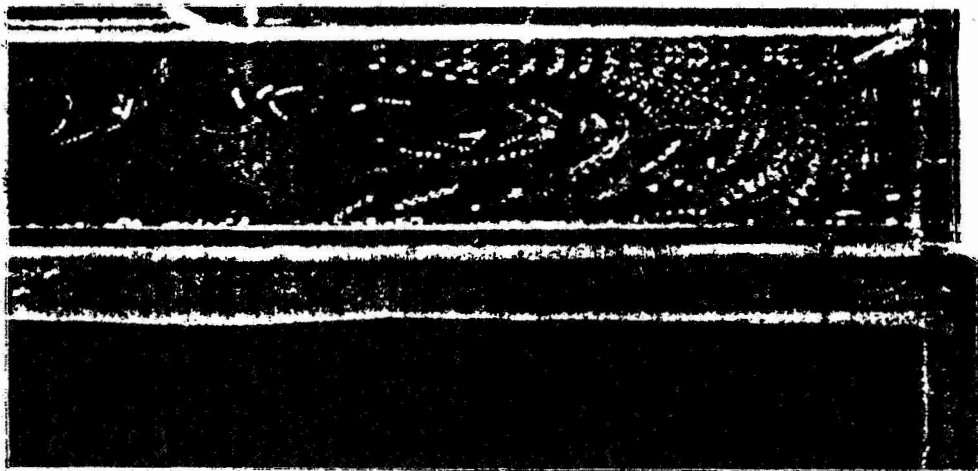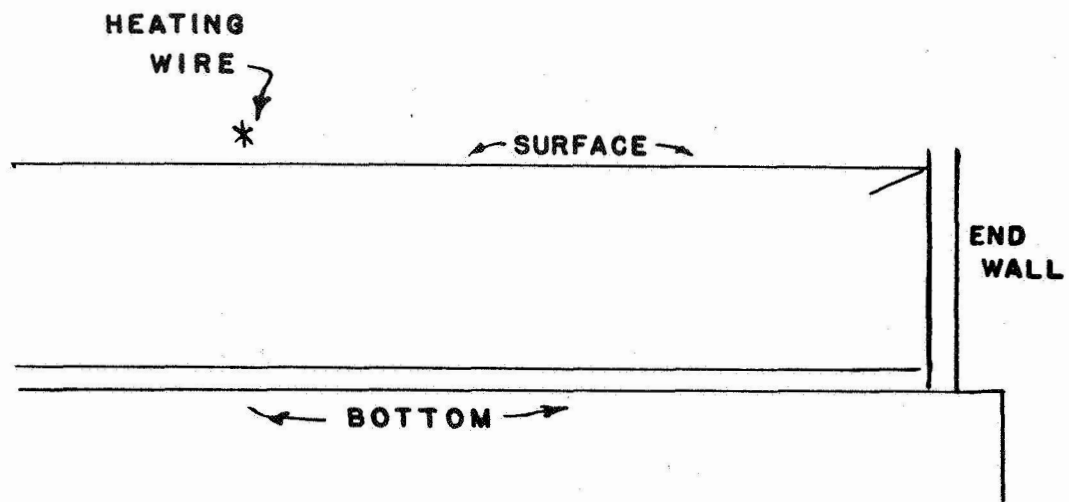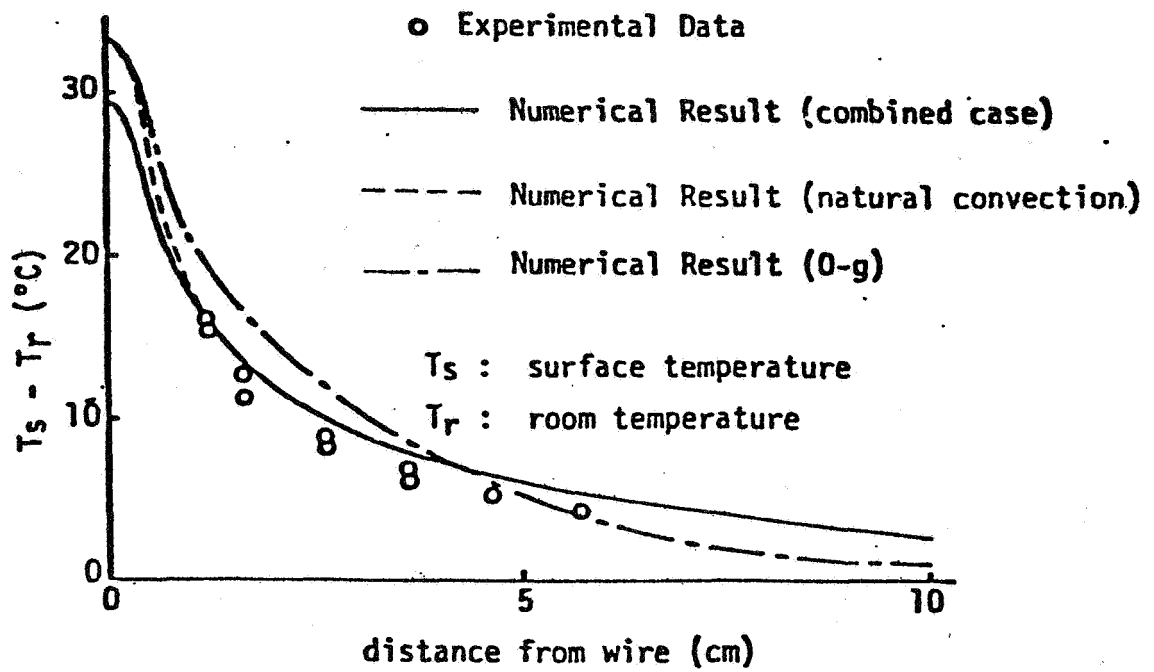Figure 2. Sequence photograph of the silicone oil flow pattern, top view.

Figure 3.   Sequence photograph of the silicone oil flow pattern, side view.

o Experimental Data

—————— Numerical Result (combined case)

— — — — Numerical Result (natural convection)

—··—— Numerical Result (0-g)

T_s : surface temperature

T_r : room temperature

SURFACE TEMPERATURE DISTRIBUTION
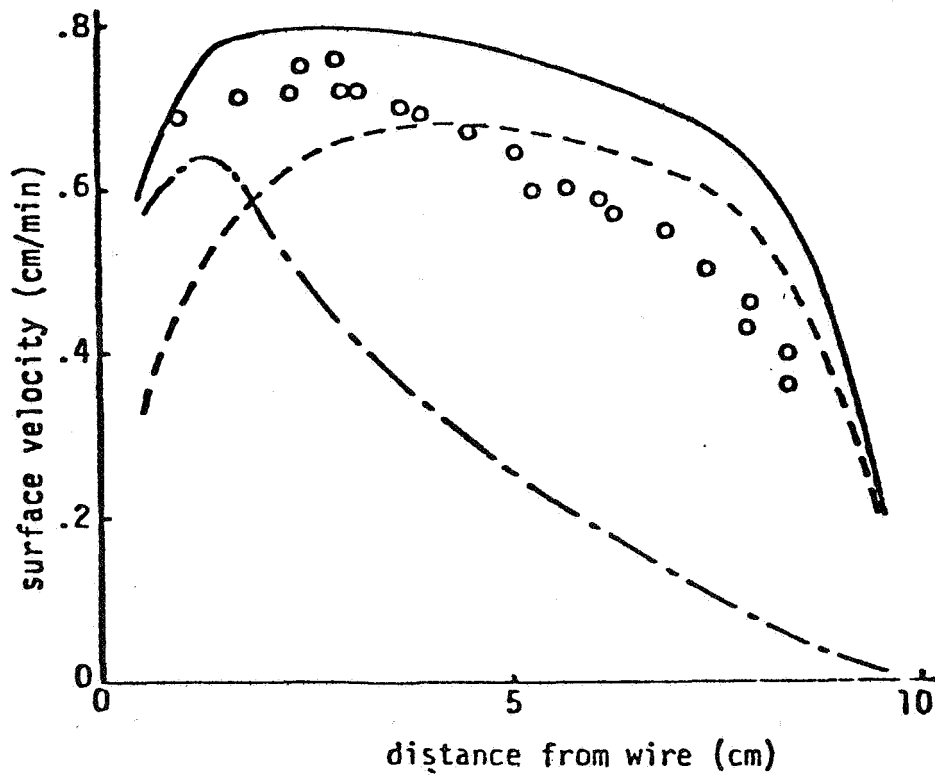
SURFACE VELOCITY DISTRIBUTION

Figure 4. Experimental and numerical results for the
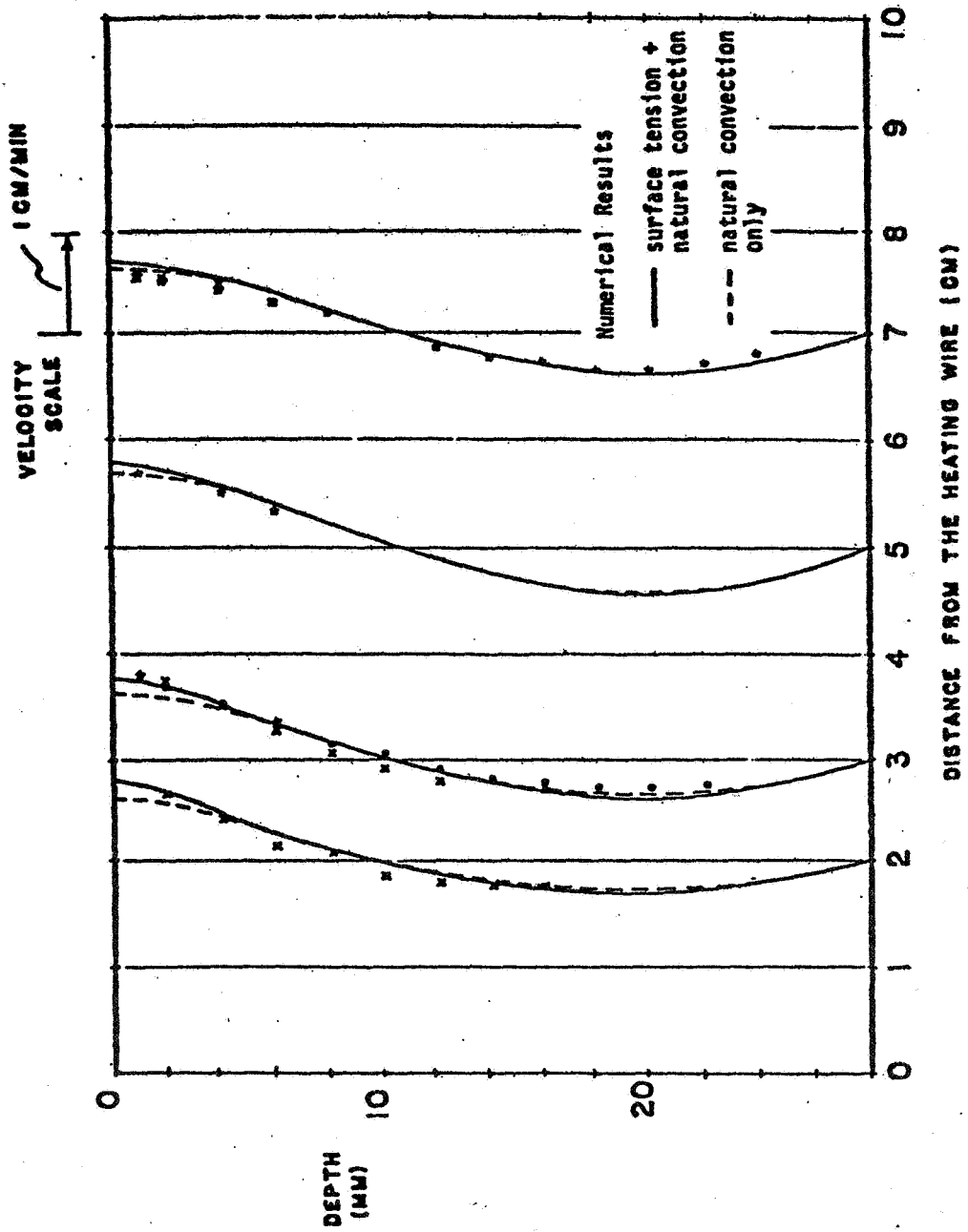surface of silicone oil.

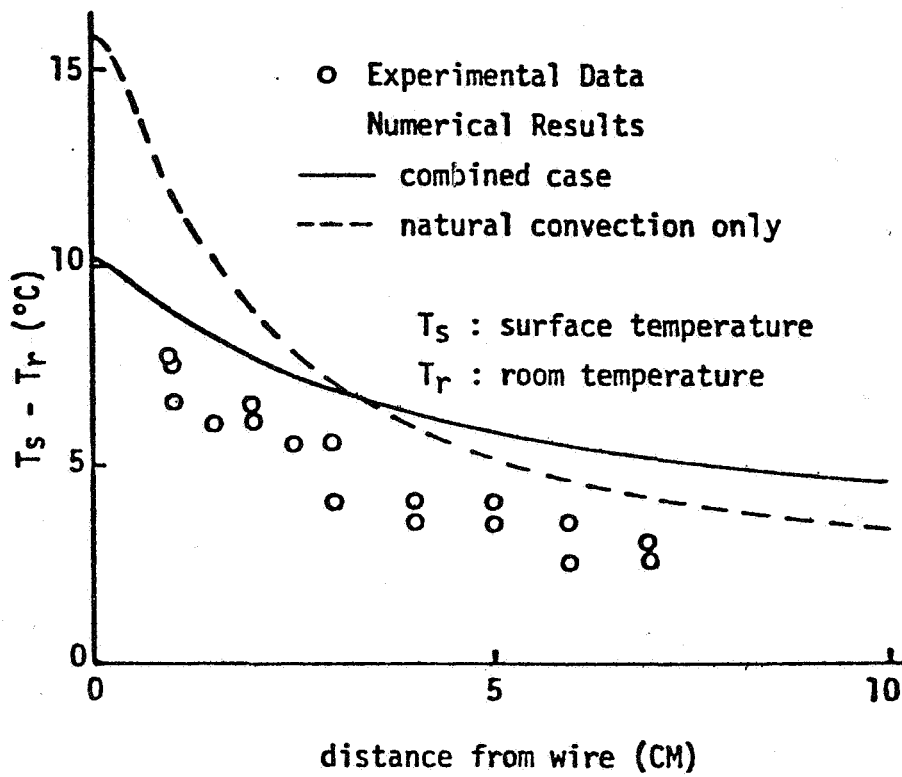Figure 5. Numerical and experimental results for silicone oil.

28

Figure 6. Experimental and numerical temperature
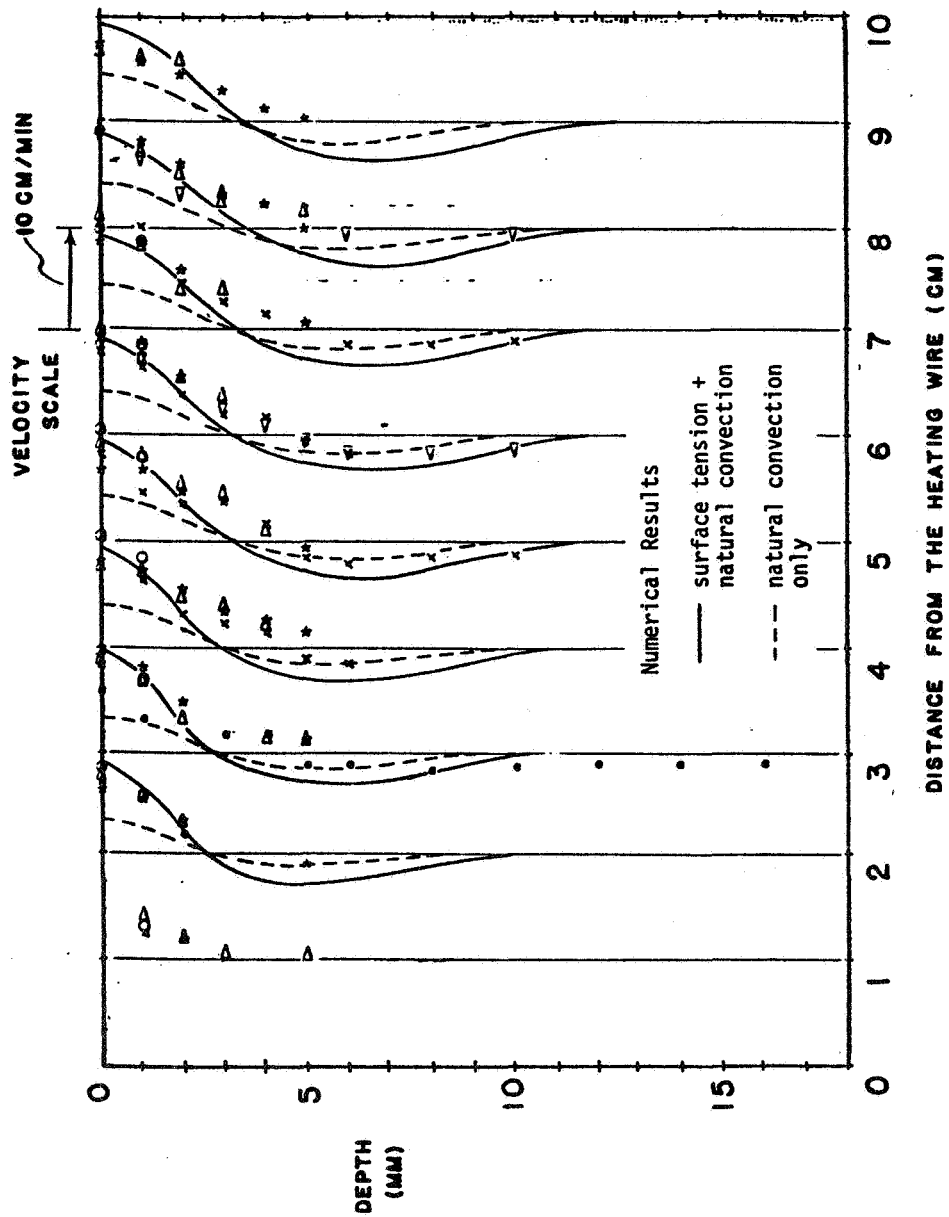distribution for FC-43.

Figure 7. Numerical and experimental results for FC-43.
(The six different typed symbols each represent the
experimental data from an individual data run.)

Although it was not presented by Professor Ostrach, Mr. Lowry pointed out after the meeting that there was considerable difference in the boundary layer depths of the surface tension-driven flows between silicone oil and FC-43. In the case of FC-43, the boundary layer thickness, given by

$$\delta = \left[\frac{\rho \upsilon^2 L^2}{(\partial \sigma / \partial T) \; \Delta T} \right]^{1/3} \quad ,$$

is 0.49 cm, which is small compared to the depth of the container. In silicone oil, this boundary layer increases to 39 cm, which is much greater than the container dimensions. For molten Si, the boundary depth is 0.1 cm.

B. The second series of experiments involves the investigation of the flow field in a liquid column suspended vertically between two rotating ends. The investigation under isothermal conditions has been completed. The two rotating ends were inserted into the shafts of two variable speed dc motors. The ends were carefully aligned, and the vibration was minimized. First, shape stability experiments were conducted by rotating both ends at the same speed and direction and, also, by keeping one end stationary. A predetermined amount of clean water (determined by the diameter and length of the space between two ends) was inserted into the space by a hypodermic needle. The fluid motion was observed with a microscope. The motor speeds were increased gradually until the liquid zone disintegrated. Just before that occurred, the liquid column had a nonaxisymmetric shape, shown in Figure 8. In Figure 9, the dimensionless zone destruction frequency is plotted against the length to radius ratio. Each point in the figure is the average frequency of several runs. The broken line is the theoretical prediction for the C-mode disturbances. The data agree well with the theory. The data for the semirotational case (one end fixed) are presented in Figure 10. In this case, as the speed was increased, the same nonaxisymmetric shape was first observed as in the corotational case; but, unlike that case, the liquid column did not disintegrate immediately after the surface deformation. Instead, as the speed was increased further, the column returned to the original cylindrical shape and stayed like that until the maximum speed of the motor was reached. A careful observation of the flow field revealed that the flow becomes turbulent after the appearance of the nonaxisymmetric deformation, and the randomness appeared to restabilize the liquid column shape. The result in Figure 10 shows the frequency at which the nonaxisymmetric deformation occurs. The stability limit was higher than the corotational case. This is mainly because the average rotational velocity is smaller in the semirotational case since only one end is rotating. The flow structure in the semirotational case was qualitatively studied by tracing small particles in the liquid column with the microscope. The particles followed rather complex spiral trajectories. The motion has been qualitatively studied in the past by
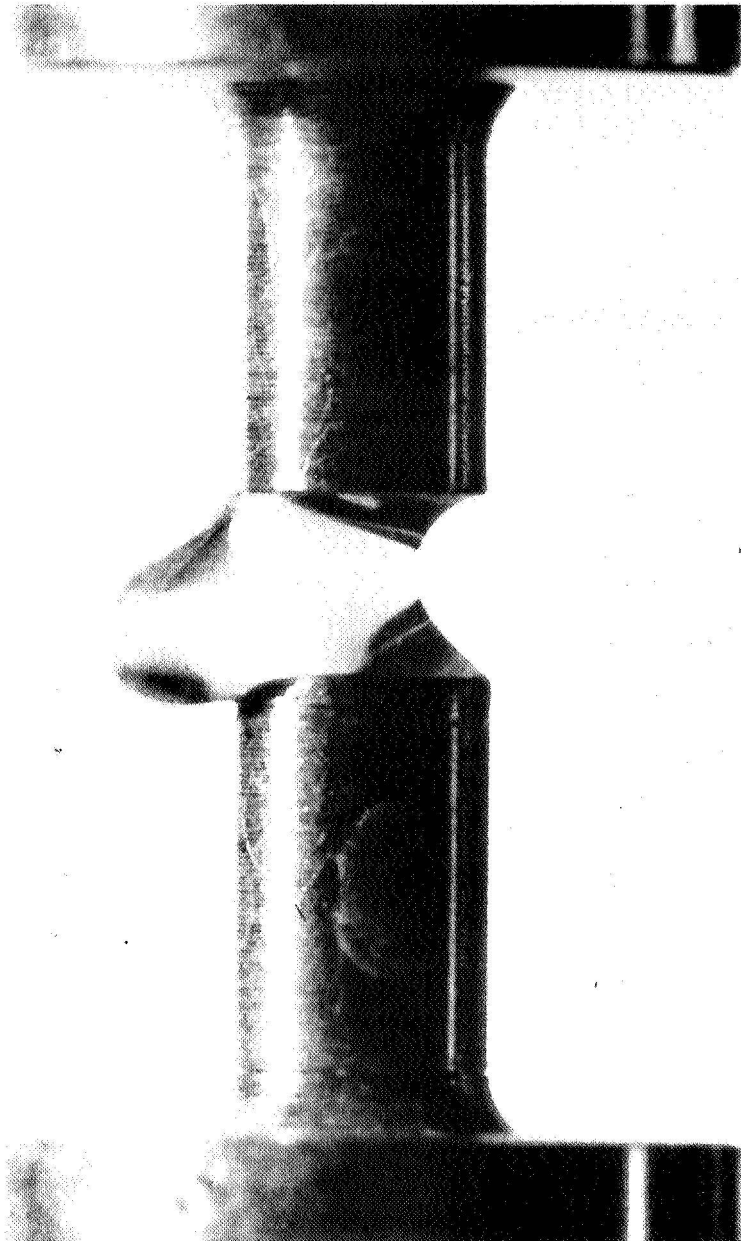
Figure 8. Shape of liquid column just prior to break-away.
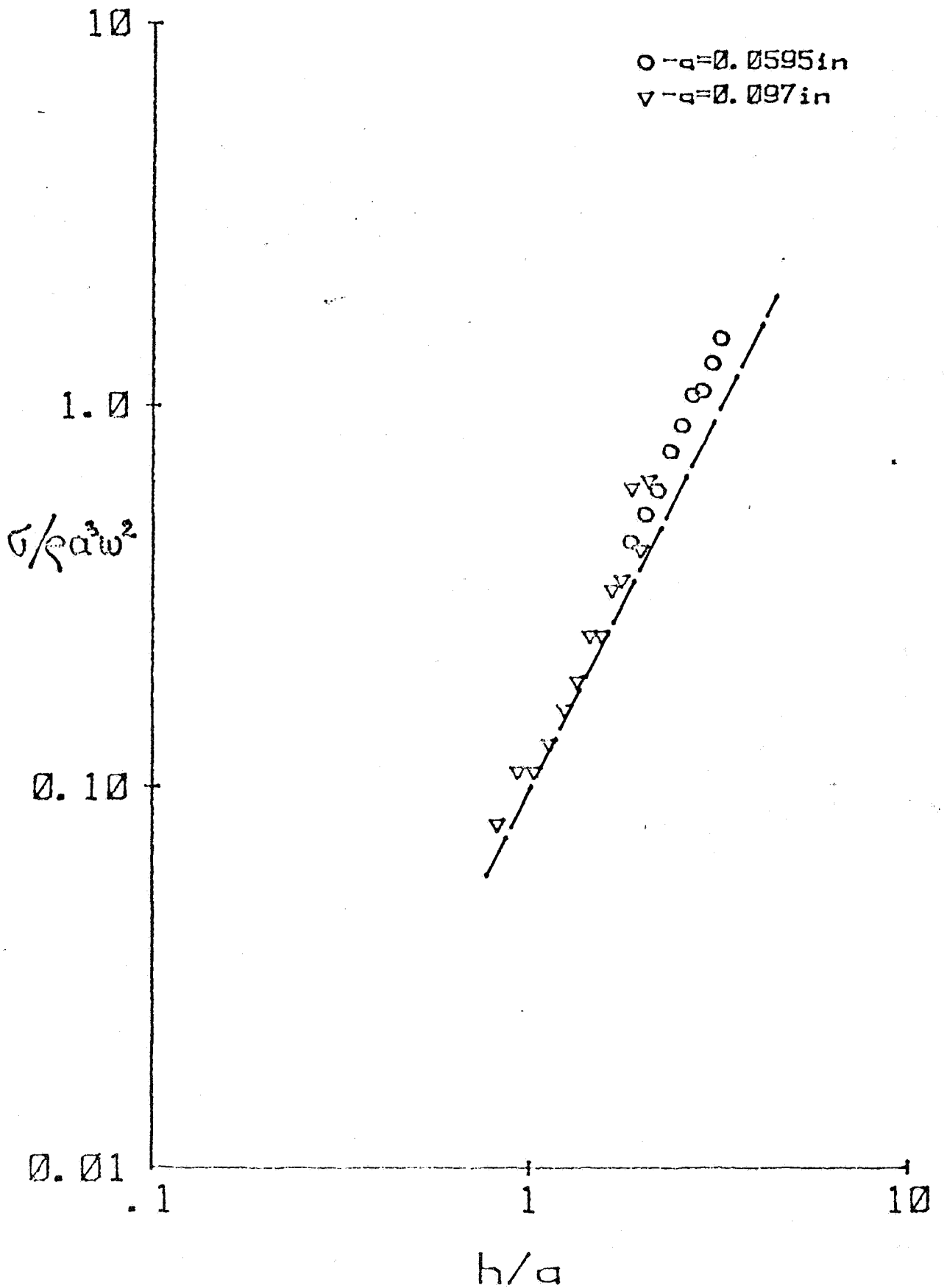
Figure 9. Stability limit for corotational case.
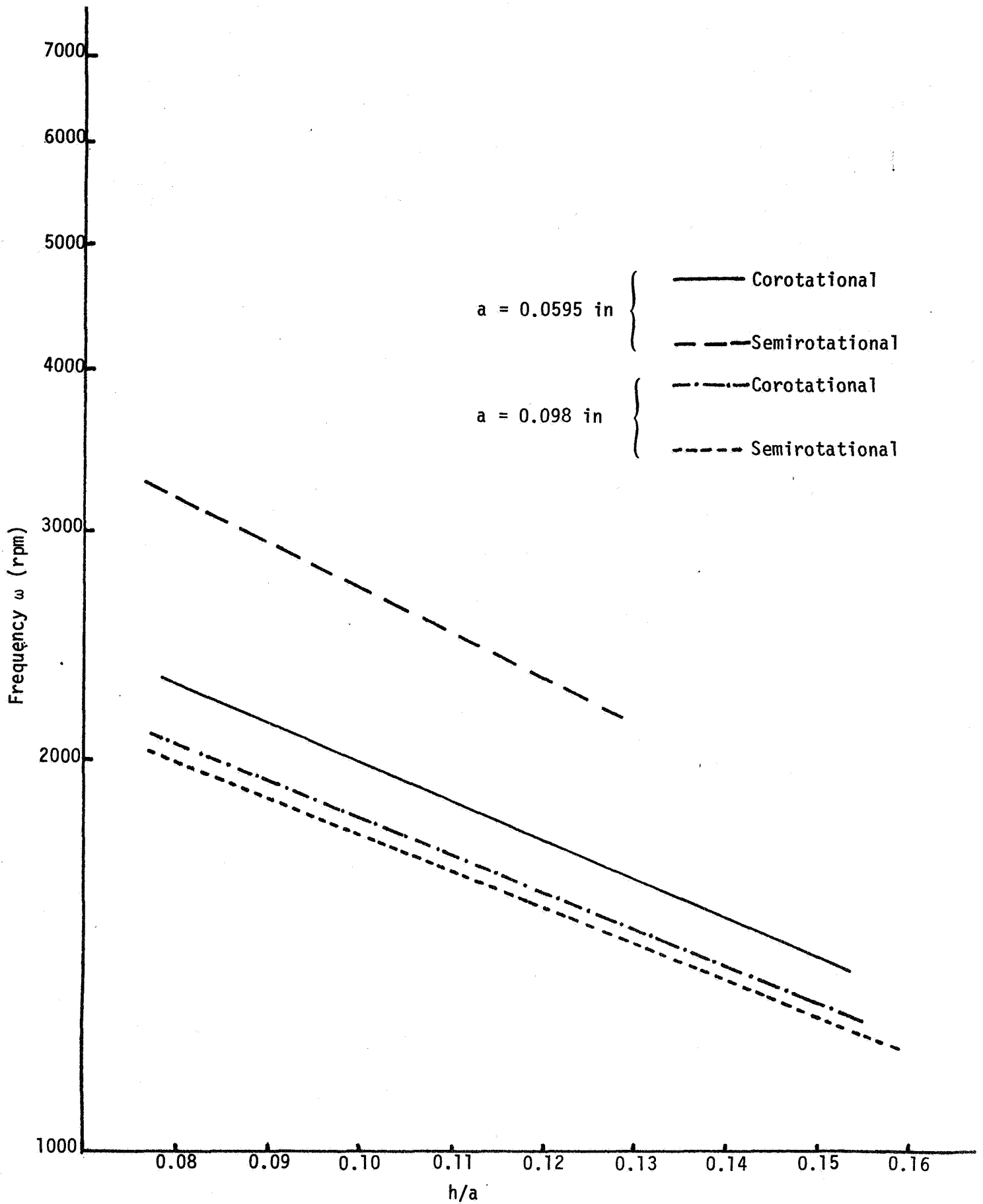
Figure 10. Experimental stability limits for the semirotational and
corotational case for two different radii.

Fowle et al. at A. D. Little. The present observations are in agreement with theirs. So far a good technique to study quantitatively the motion in such a small liquid column has not been found. The feasibility of a LDV system suitable for the present configuration is being studied.

Currently a heating system is being developed to heat one end of the liquid column in order to introduce surface tension as well as natural convection into the rotational flow field. The temperature field will be primarily studied, especially temperature oscillations predicted under certain conditions by the past work on the floating zone system.

FLOAT ZONE EXPERIMENTS

John Verhoeven

Dr. John Verhoeven reported on the experimental work being carried out at the USDOE Ames Laboratory, Iowa State University. The objectives of this work are: (1) to determine if surface tension-driven convection in float zone experiments may be controlled by means of surface films and (2) if convection can be controlled, determine: (a) whether homogeneous solute distributions will be achieved in float zone solidification and (b) whether accurate measurements of liquid diffusion coefficients may be obtained from float zone solidification experiments.

The major goals of the program are outlined in Table I. Sn was chosen as a model material because (1) it is a group IV element, chemically similar to Si and Ge and (2) its low melting point and low vapor pressure allow Auger spectroscopy to be employed with liquid samples. Good oxidation kinetics data are available for solid Sn for pressures > 10^{-3}, but only limited data exist for liquid Sn. Oxides form via nucleation of islands followed by lateral growth on a chemisorbed layer. Above 1 Torr, the oxide develops internal cavities after achieving continuous coverage. Below 1 Torr, the oxide may not become continuous. The oxide is in the form of SnO below 280 C and undergoes a transition to SnO_2 between 280 and 600 C.

Surface analytical techniques that may be applicable are Auger, XPS, EELS, and UPS. A literature search reveals that practically no work has been done on liquid metal surfaces (with the exception of the NASA-sponsored work at NBS on liquid Ga). There is a good line shift between metallic Sn and oxidized Sn, but no observable shift between SnO and SnO_2 on either Auger or XPS. There is some evidence of a thin layer of SnO_2 on SnO films from valence band spectra of XPS and in-depth selective Mössbauer studies.

A schematic of the experimental concept is shown in Figure 1. A molten zone of Sn is supported internally by a Ta tube which, in turn, is heated and cooled from the inside. This maximizes the viewing of the free exterior surface by the surface analyzer and solves some of the heat transfer problems posed by attempting to get heat in and out of a low-temperature sample in a vacuum. A more detailed design of the heating/cooling mechanism is shown in Figure 2. At present, heating is accomplished by E-beam. The thermal profile achieved by this apparatus is shown in Figure 3.

A number of problems were encountered with the use of E-beam heating in a low-pressure O_2 environment. Even at 10^{-4} Torr, the W filament reacts with O_2 to form WO_3. Also, both CO and CO_2 may be produced by the filament from any residual C atoms that may be present. Oxygen ions may form in the beam which may change the heat input

OUTLINE MAJOR GOALS OF GROUND BASE EXPERIMENTS

A. Design and build a float zone apparatus which would allow us to control and measure in a high vacuum environment:
1. Temperature gradients
2. Growth rates
3. Residual gas levels, particularly oxygen

B. Develop techniques to measure:
1. Oxide layer thickness on molten tin employing Auger plus depth profiling equipment
2. Solid-liquid interface shapes and liquid zone lengths
3. Radial and longitudinal compositional profiles

C. Establish the effect of oxide film thickness upon:
1. Convection induced oscillatory temperature fluctuations in a stationary floating zone
2. Interface shape and temperature profiles in stationary floating zone experiments

D. In float zone experiments establish effect of:
1. Oxide film thickness
2. Temperature gradient
3. Composition level

Upon:

1. Solute distribution
2. Interface shape
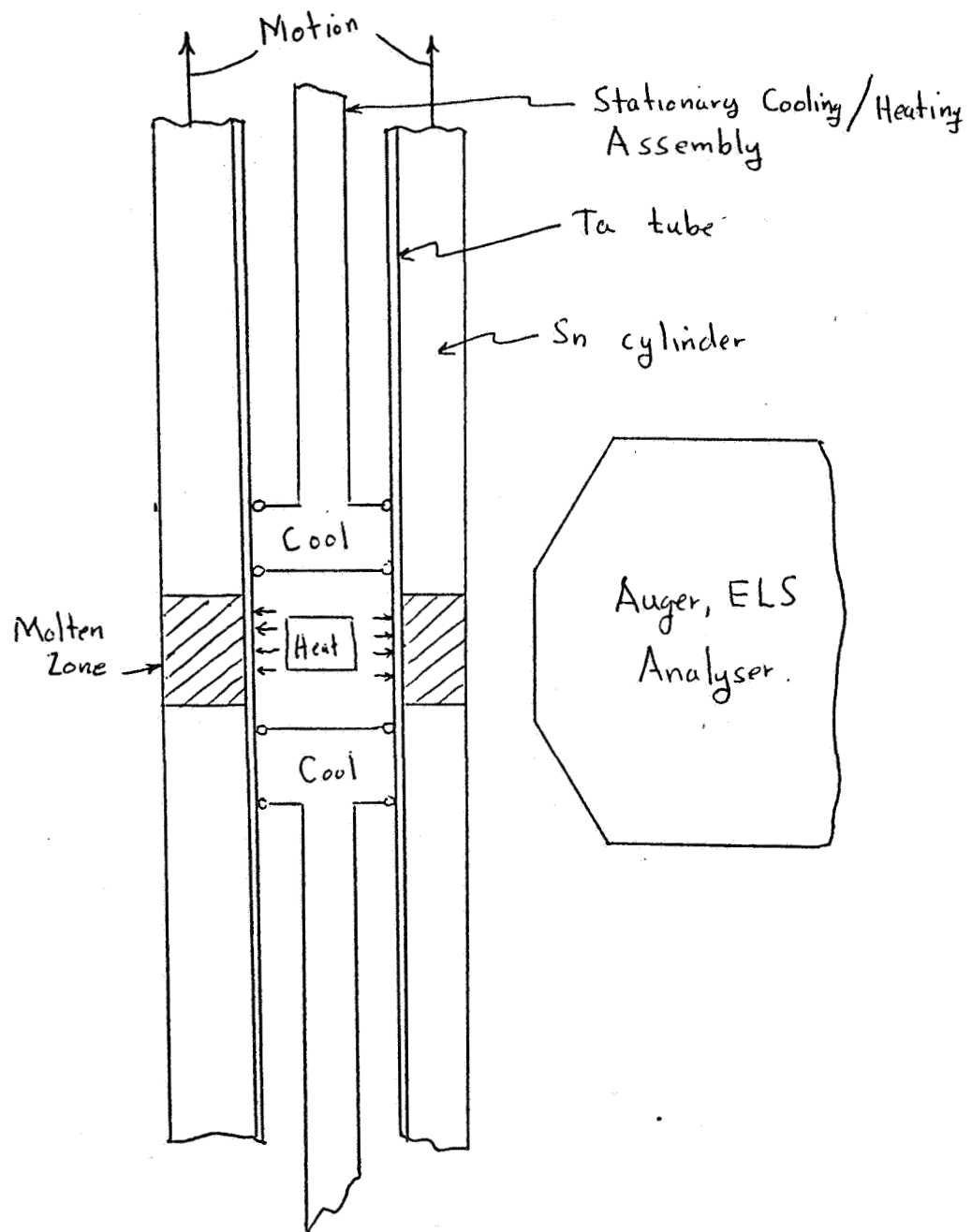3. Measured diffusion coefficients

Table I

37

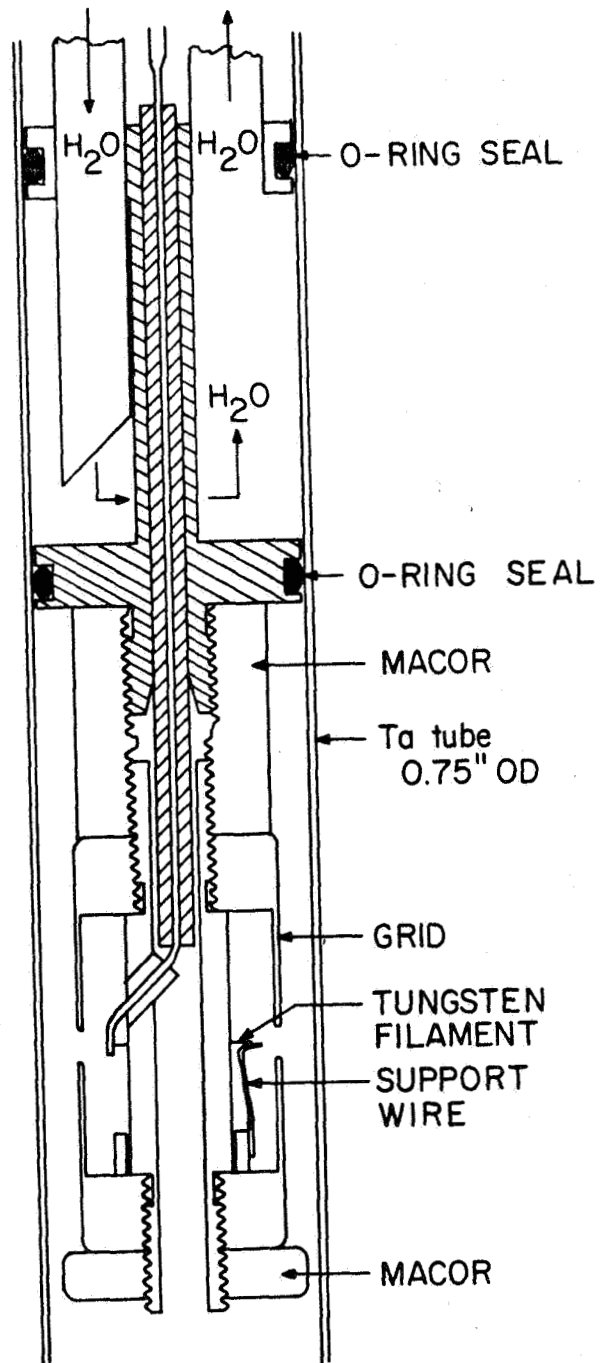Figure 1.   Experimental concept for
stabilized floating zone.

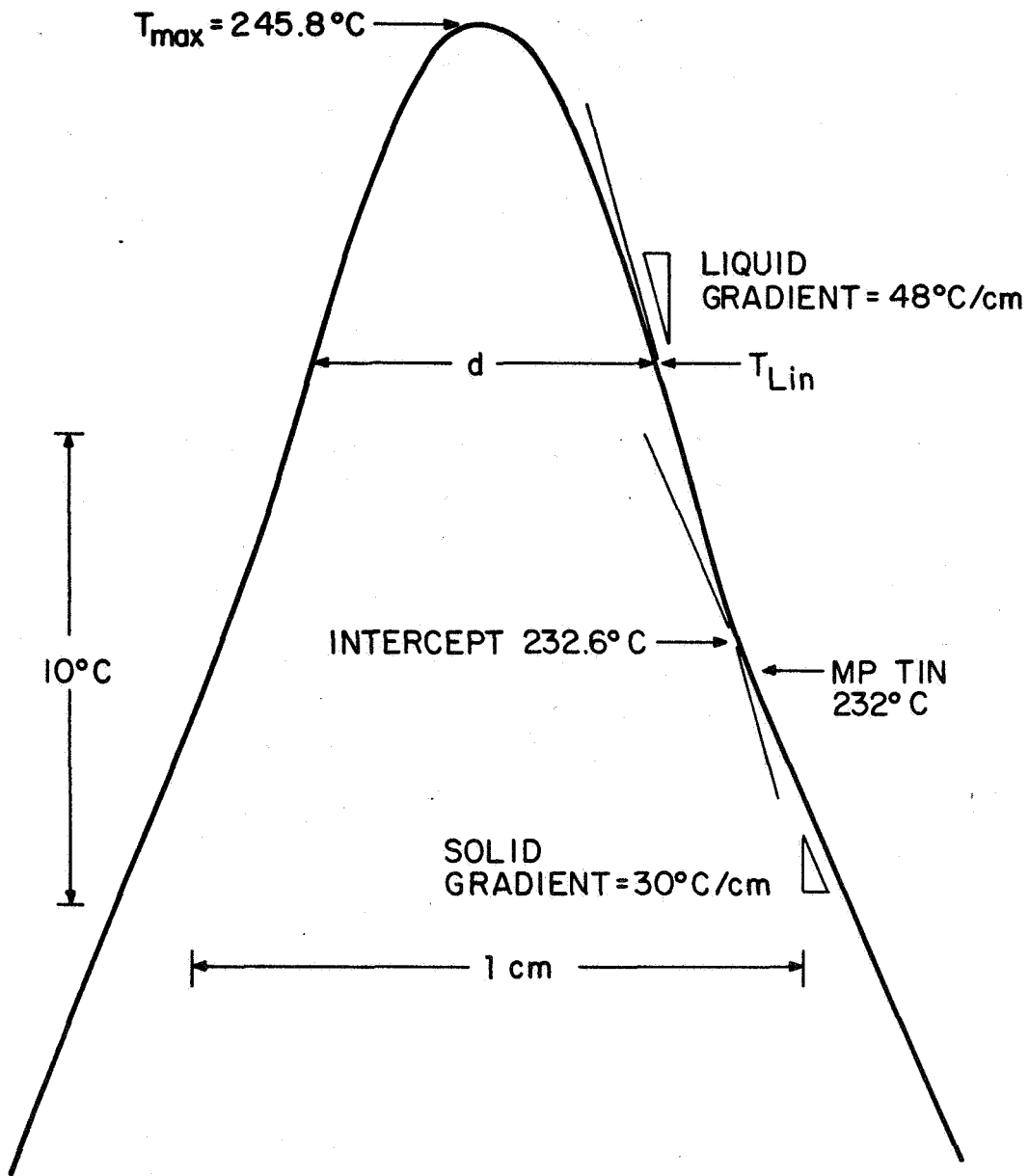Figure 2. Schematic of heating/cooling apparatus.

39

Figure 3. Thermal profile of Sn sample using heating/cooling apparatus shown in Figure 2.

40

and affect the oxide layer to be studied. Also, to produce thick oxide films, the higher pressures required are not compatible with the E-beam technique. For these reasons, an alternative heating method is being developed.

Techniques have been developed to grow and characterize SnO and SnO_2 standards. These samples have known thickness and are used to calibrate sputter rates. They are prepared by evaporation from an alumina crucible in a furnace shown schematically in Figure 4. The Sn and oxide layers are deposited on Ag-coated glass. The Ag layer acts to passivate the OH surface groups on the glass. A protective layer of Ag is deposited over the Sn layers to protect against additional oxidation. A typical depth profile is show in Figure 5.

Finally, development work on the heating stage and gas-handling system for high-temperature Auger work on Sn was presented. The present Auger setup is being modified to accommodate molten samples, as shown in Figure 6. A disc zone heater is being designed, as shown in Figure 7, which will produce the thermal profiles shown in Figure 8. The heater assembly mounted to the sample manipulator is shown schematically in Figure 9. The schematic for the gas-handling system is shown in Figure 10. This apparatus, when completed, will produce the first data on the formation of oxide layers on liquid metal surfaces at moderately high temperatures.

Tantalum Radiation Shielding
(19mm and 25mm)

Slip Cast Alumina Crucible

HRL Tungsten Heater Wire
(0.46mm Dia.)

Alumina Cement
(Norton EA-139)

Closed End Alumina Tubing
(1mm ID x 1 1/2mm OD)

Alumina Thermocouple Tubing
(2-hole 0.1mm ID x 1mm OD)

Boron Nitride Support

Thermocouple Leads
(Pt-30% Rh/Pt-6% Rh)
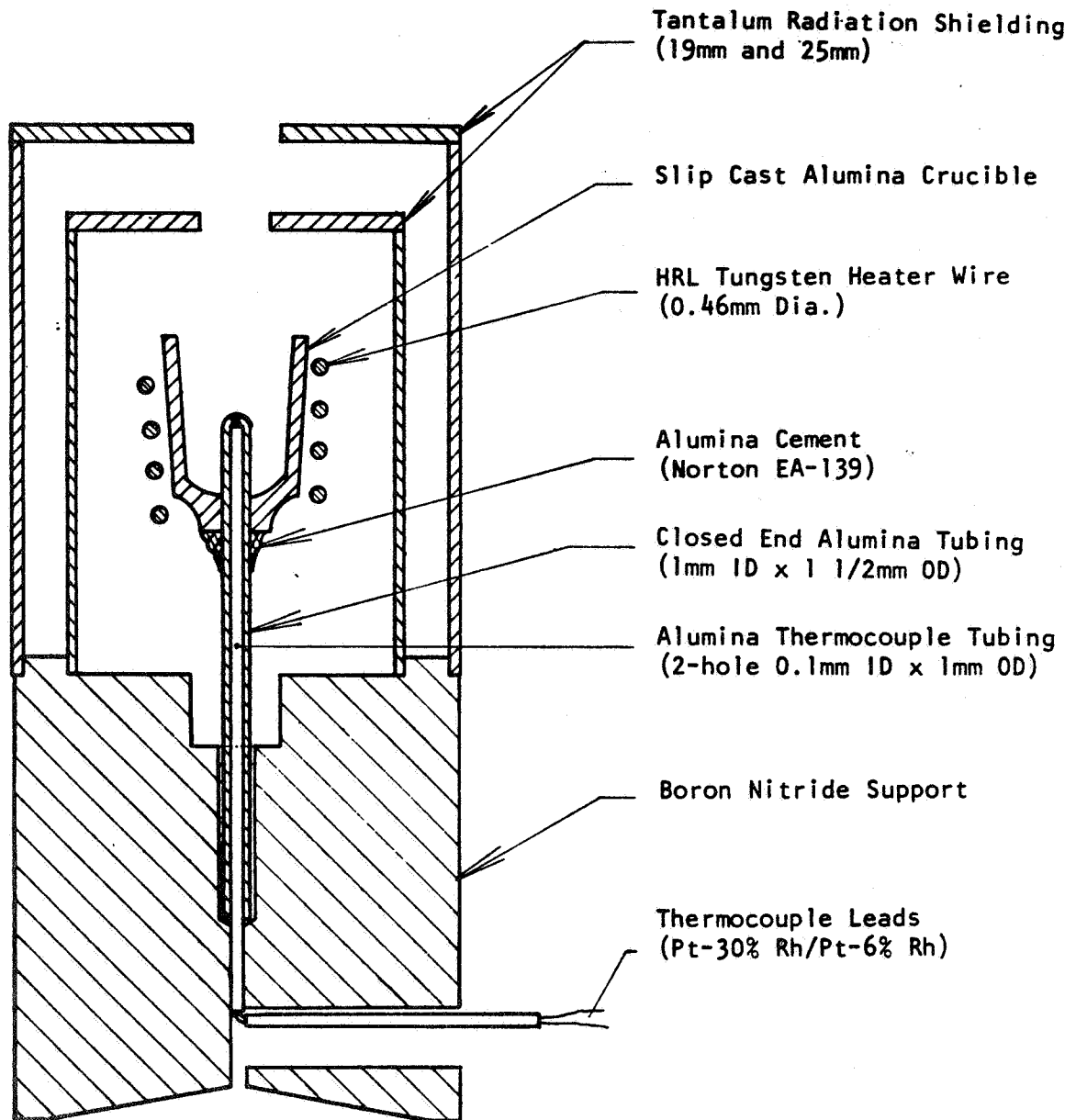
Figure 4. Furnace developed to
prepare standard SnO and SnO_2 films
for calibration of sputter rates.

42
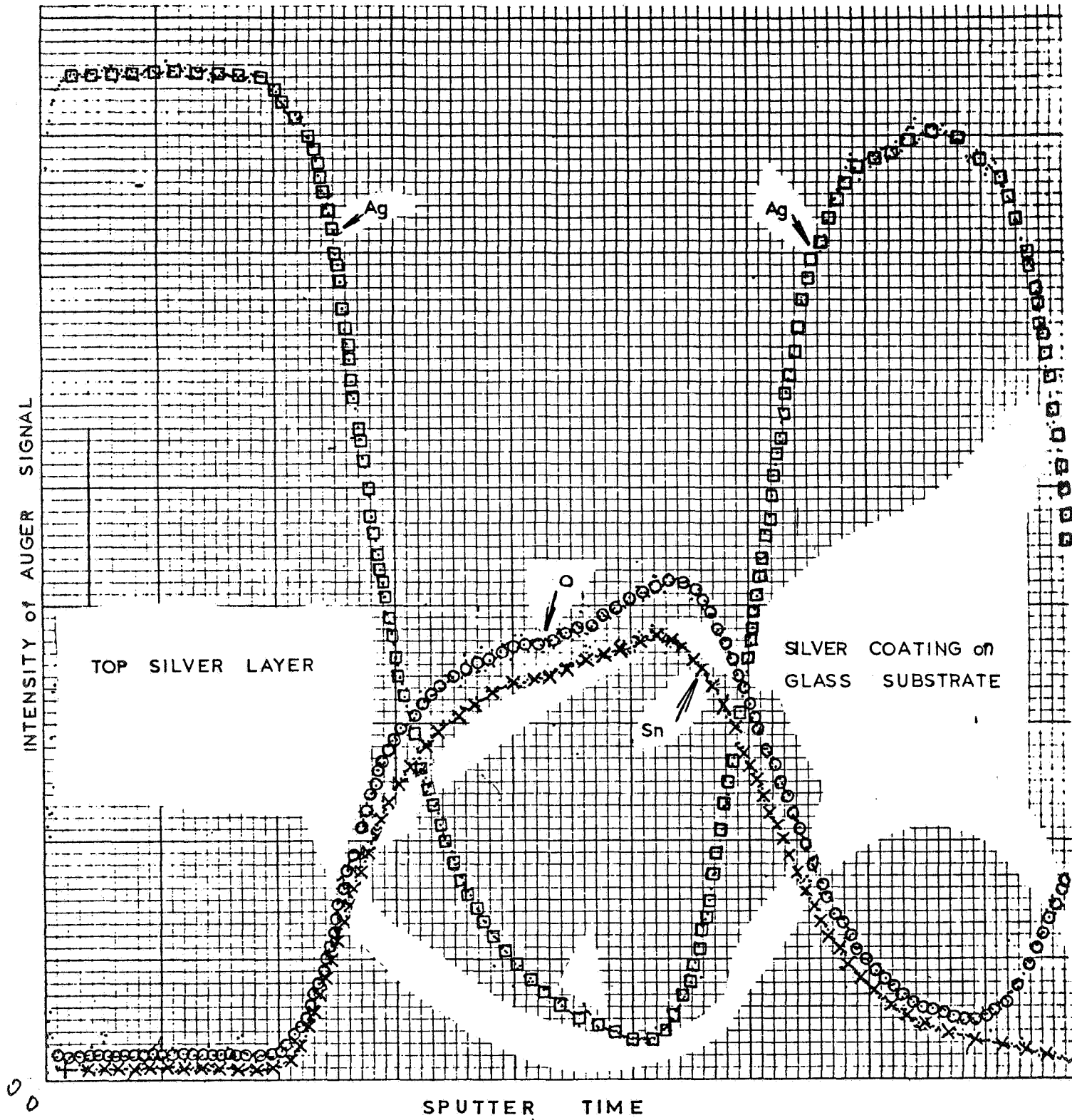
Figure 5. Typical depth profile of
SnO/O$_2$ standards.

Sample
Manipulator

Ion
gun

Heater

Thermocouple

Auger, ELS
Analyser

Physics
Division

Al Bevolc

Ion
Gun

Auger, ELS
Analyser

NASA
Project

Max Noack

Heater

Sample
Manipulator

Thermocouple
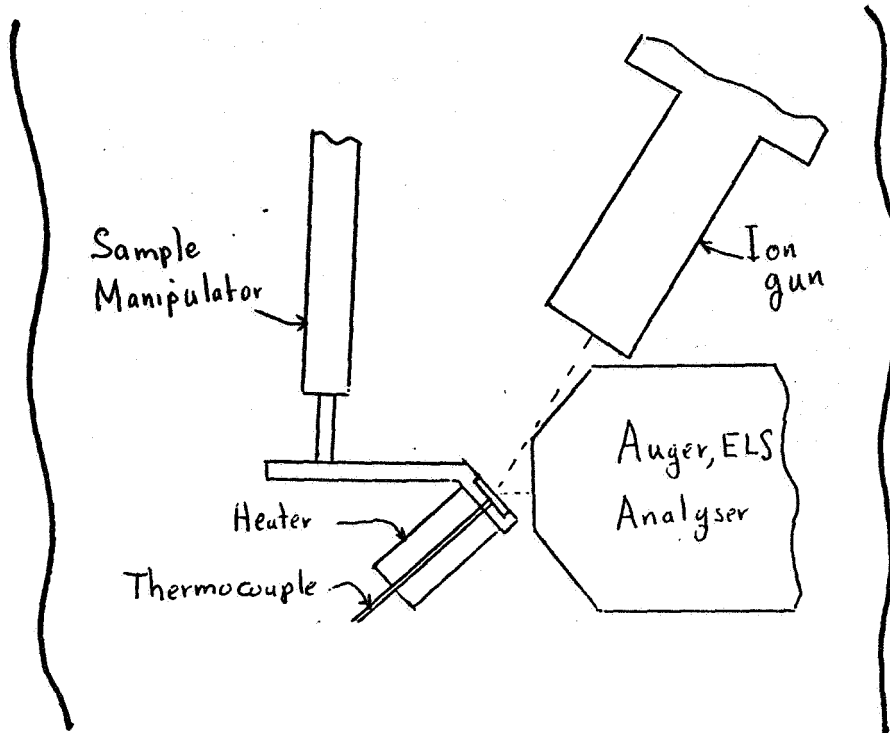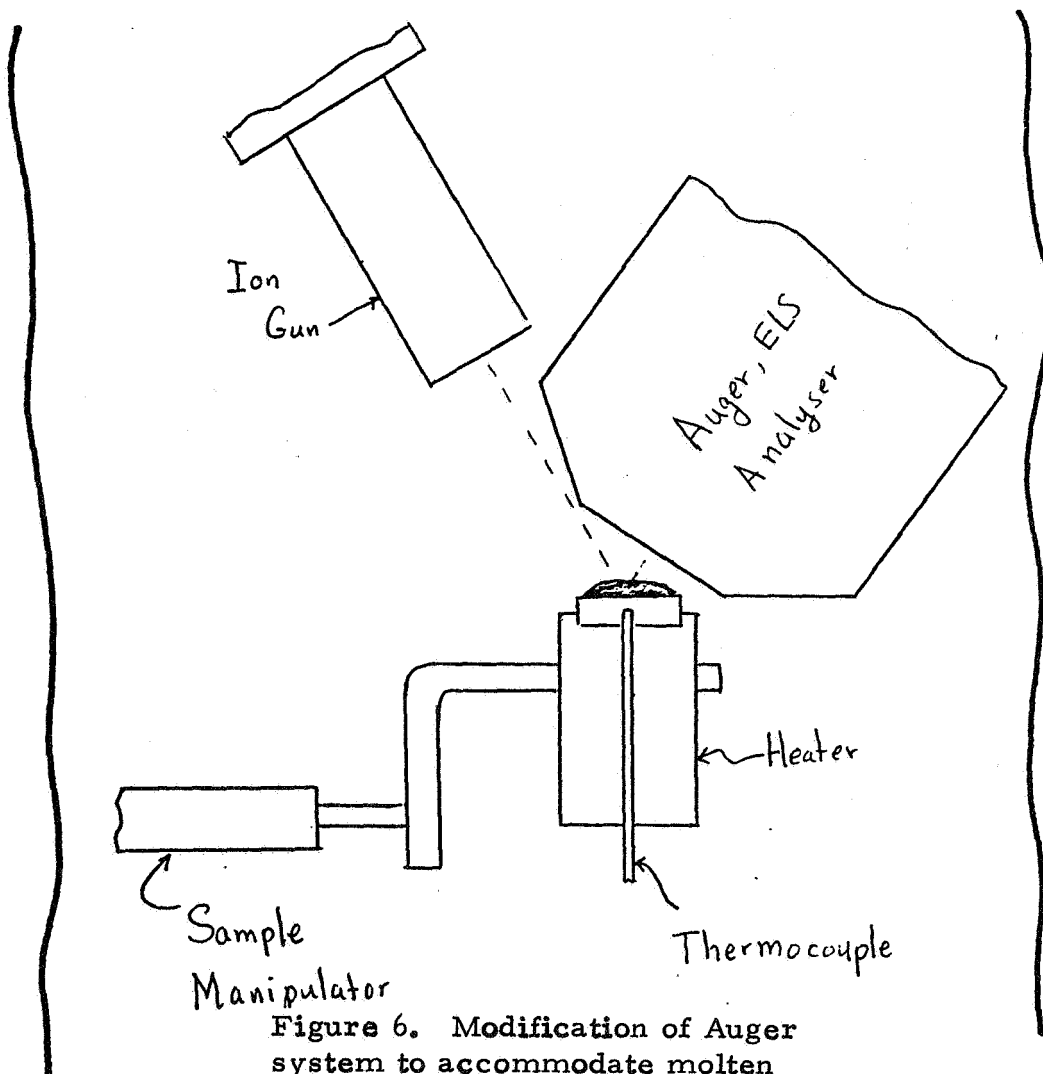
Figure 6. Modification of Auger
system to accommodate molten
samples.   44
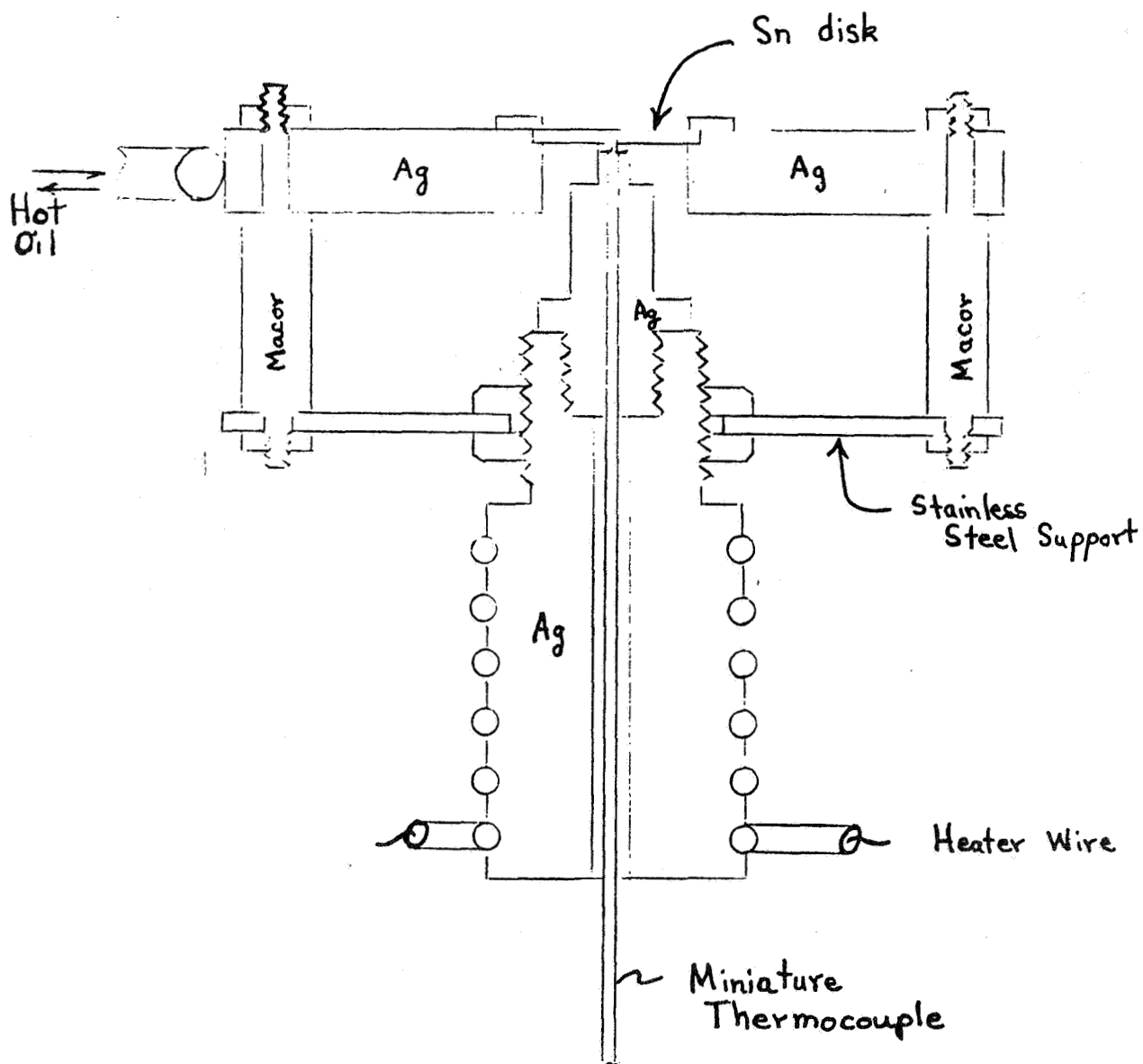
Figure 7.

Preliminary design
Disk Zone Heater Assembly

45

Figure 8

46

14 mm diam. recess milled into stainless steel plate

Stainless Clad Heater

Silver rod

Extension adjustment screws

Insulated connectors

Thermocouple

Figure 9. Sample manipulator and heater assembly for apparatus to study surface of molten Sn.

Figure 10. Gas-handling system for
Auger analysis of molten Sn surfaces.

THERMOCAPILLARY FLOWS AND THEIR STABILITY

Steve Davis and George Homsy

The final talk in session A was a summary of the work recently started by Prof. Steve Davis, Northwestern, and Prof. George ("Bud") Homsy, Stanford. The following is a summary prepared by Professor Homsy.

Our work on thermocapillary flows has just recently begun, and so I will briefly cover our progress over the last few months and indicate our future directions. The work described below is due in part to Mr. M. Smith and Drs. A. Sen and M. Floryan.

General Remarks

Thermocapillary flows represent a relatively little-studied area of interfacial fluid mechanics, and, although many of the general principles are in hand, there is not yet a great store of experimental and theoretical knowledge of 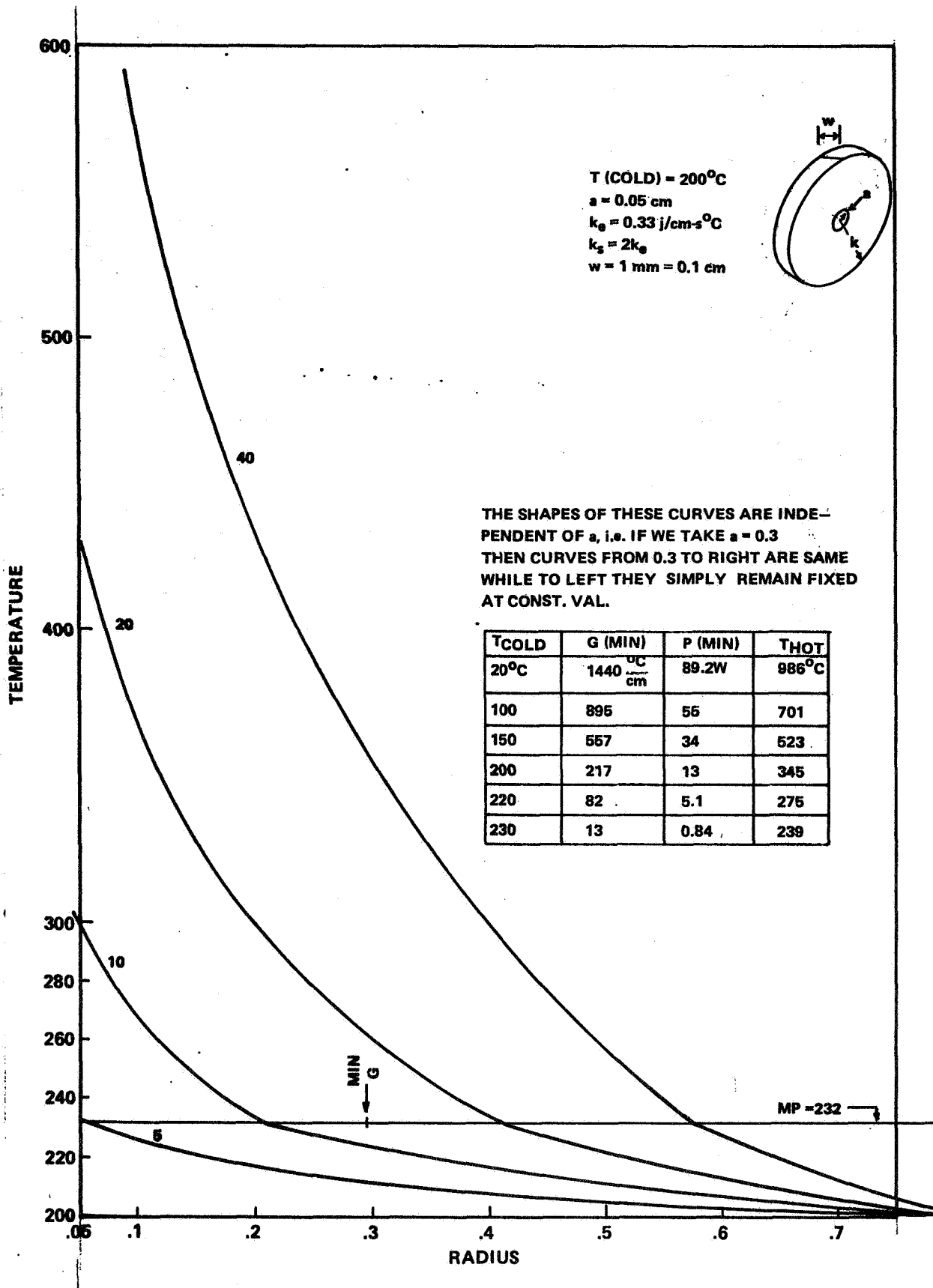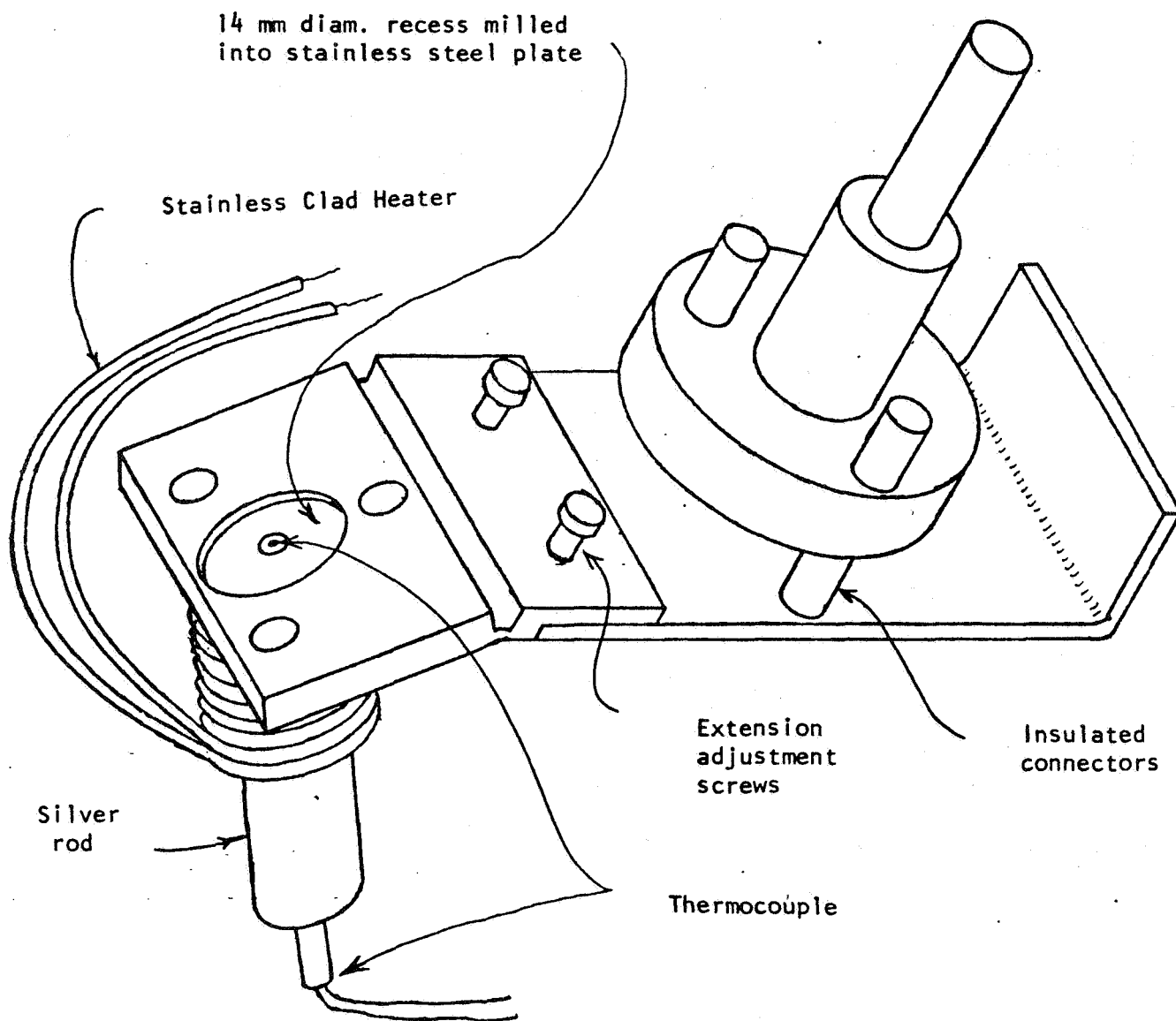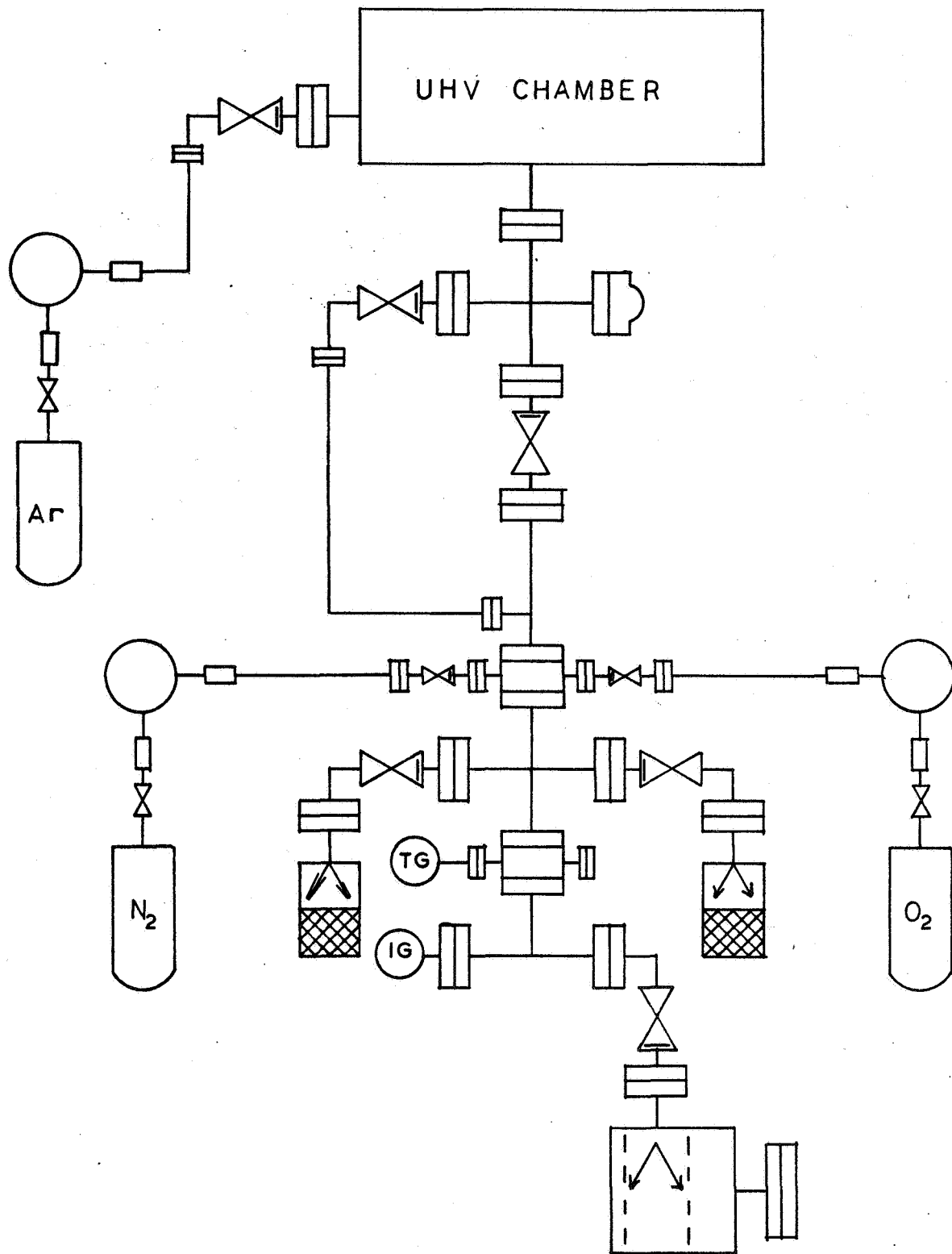these systems. It seems reasonable to expect, however, that the strength and nature of the convective flows will have a strong dependence upon the dimensionless group,

$$Ma = \frac{\Delta\sigma L}{\mu K} \quad ,$$

which is a Marangoni number based upon a characteristic length, L, and an imposed surface tension difference, $\Delta\sigma$. Furthermore, as Ostrach has shown for this class of flows, Ma is equivalent to a Peclet number. Thus we expect a progression of regimes:

$$\text{Conduction Domination} \longrightarrow \text{Steady Convection} \longrightarrow \text{Steady Boundary Layer Convection}$$

$$\text{Oscillatory Convection} \longrightarrow \text{Interfacial Turbulence}$$
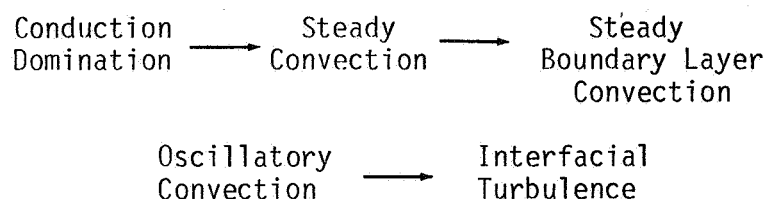
as the Marangoni number increases. Not all regimes will occur for all geometries, etc., and the transition points between regimes will clearly depend upon all parameters of the problem. Furthermore, as shown by Ostrach, the thermocapillary Reynolds number is

$$Re = Ma/Pr \quad ,$$

and thus we see immediately that thermocapillary flows in low Prandtl number liquid materials for which convection is important, $Ma \geq 0(1)$, are also ones in which fluid inertia will be important.

One may also show quite generally that the degree of departure of the free surface from the rest state (i.e., the state determined by isothermal capillary statics) will be dependent upon a capillary number, which in the present context takes the form

$$Ca = \frac{\Delta \sigma}{\sigma_0} \quad ,$$

where σ_0 is the mean tension. Since $Ca < O(1)$, distortions due to thermocapillary-driven flows may be in many cases adequately described by perturbation analyses about the rest state. (For an example of the effect of surface deformability on instability points, see Davis and Homsy, JFM 98, 527, 1980.)

The general objectives of our program are to:

1. Describe steady convective flows for geometries of varying complexity. This in general involves the solution of nonlinear free boundary problems.

2. Determine the stability of these flows to more complicated (perhaps time dependent) modes of fluid motion. These include shear flow and free surface instability modes, with possible coupling between them.

3. Describe, in as much detail as possible, the effect of surface chemical species, including impurities which act as surfactants and insoluble oxide films, on the convective patterns and their stability.

In order to illustrate this in more detail, I would like to discuss our recent preliminary results on three problems.

Thermocapillary Convection in a Trough
(Sen and Davis, Bull. Am. Phys. Soc. 25, 1101, 1980)

We have considered the problem sketched below:

Hot   Cold
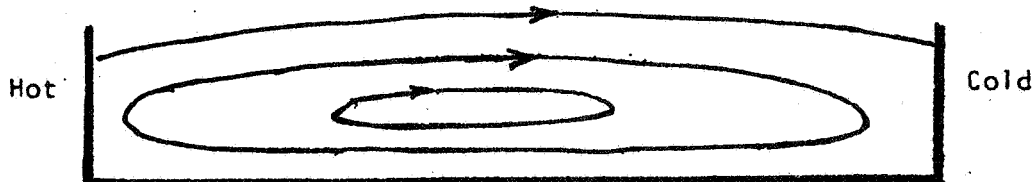
The parameters of this problem are:

$A = H/L$ aspect ratio

$Ma = \Delta\sigma L/\mu k$ = Marangoni number

$Pr = \nu/k$ = Prandtl number

$Ca = A\Delta\sigma/\sigma_0$ = capillary number

$Bi = hL/k$ = surface Biot number

In addition, the contact between liquid and solid must be prescribed. We have considered the two cases of (i) fixed contact angle and (ii) pinned (fixed) contact lines as being probable extreme cases.

We have solved this problem by asymptotic expansions for shallow troughs ($A \ll 1$). The results consist of a nearly parallel flow in the main regions of the container, with turning flows near the ends. The flow field is as sketched below:
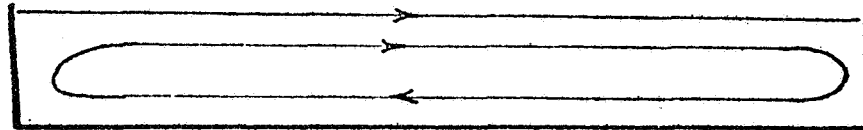
(a) Circulation
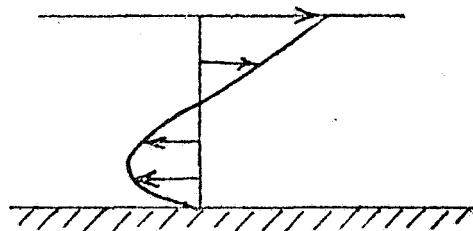
(b) Velocity distribution in the central region

In addition, we sketch the surface deflection for the cases (i) and (ii) above:
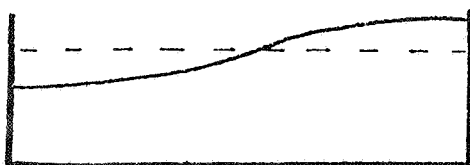
(i) Fixed contact angle
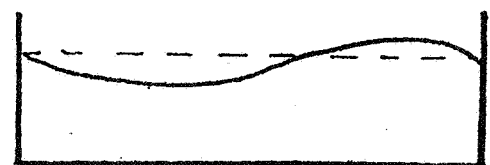
(ii) Fixed contact lines

51

The conclusions obtained thus far may be summarized as:

1. There is a region of parallel flow in the center region of the trough; the existence of this parallel flow depends upon Ma and A in a way which is analytically explicit.

2. Surface deflections may be calculated as perturbations from the rest state and, in two dimensions, are generally negative (positive) above hot (cold) currents.

3. Dynamic contact angle phenomena may be modelled.

Stability of a Parallel Thermocapillary Flow
(Smith and Davis, Bull. Am. Phys. Soc. 25, 1077, 1980)

As we have seen, the flow in shallow troughs may be approximated as nearly parallel in the regions removed from the end walls. The stability of such a flow, treated as being unbounded, is obviously of interest, as it may determine the onset of oscillatory convection in a shallow trough of finite size.

We have investigated the stability of the simplest of such parallel flows, in which

$$T_0 = -x + \frac{Ma}{6} (1 - y^3)$$

$$u_0 = y$$

$$v_0 = 0$$

$$h_0 = 1$$

A sketch of this base state is:

(a) Isotherms   (b) Velocity Profile
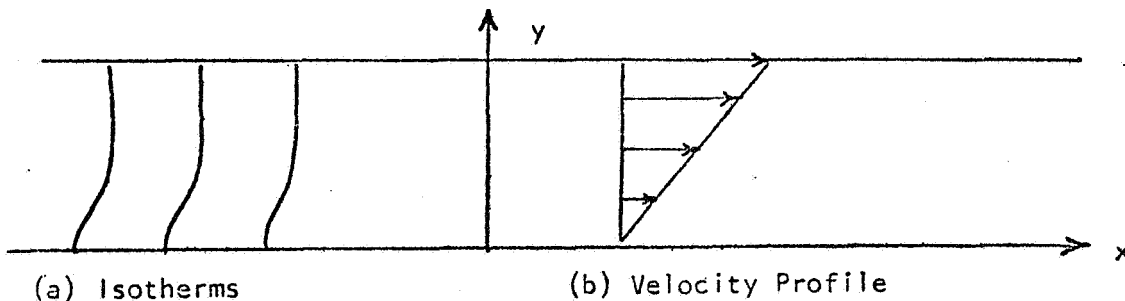
The linear stabililty of this flow is described by solutions to the governing equations in which perturbatins are taken to be of the form of travelling waves, i.e., proportional to exp {σt + i (kx - ct)}. To find the region between stability and instability (i.e., σ = 0), we solve the Orr-Sommerfeld equation, the linearized energy equation, and we include the coupling of temperature and velocity through the interfacial conditions.

It is easy to show that for no surface deformation (Ca ≡ 0) and small Ma, the flow is stable, and we thus expect the stability limit to depend strongly on capillary number, Ca. In preliminary calculations for Ca = 0.2, Pr = 3 x 10^{-3}, we find a critical Reynolds number Re ≃ 72 and a critical wave number k_c ≃ 2.0 at which the wave speed of the neutral wave is approximately 1/3 the surface speed. This instability is primarily of the shear flow type, since Ma_c = Re_c Pr ≃ 0.2; i.e., the temperature is determined primarily by conduction. In addition, it illustrates the coupling between shear instabilities and free surface modes. Future work will include a full parameter study of the stability of this simple flow, as well as the parallel flow which occurs in the shallow trough.

Thermocapillary Convection in Axisymmetric Capillary Bridges
(Floryan and Davis, Bull. Am. Phys. Soc. 25, 1101, 1980)

Convection in axisymmetric capillary bridges between solids with fixed contact lines represents challenging problems, since the isothermal rest state may have two nontrivial radii of curvature. Consider, for example, a bridge of unit aspect ratio (L = D), containing varying volumes of fluid. The family of rest states will appear as sketched:
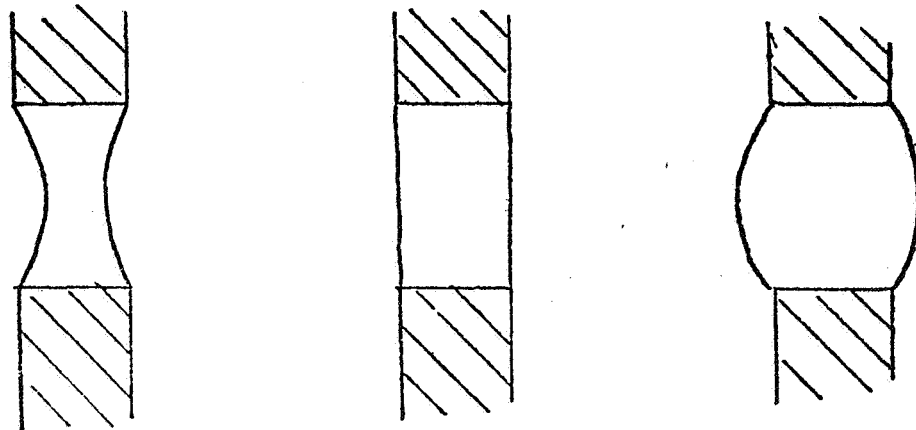
Consider the case in which the solids supporting the bridge are at different temperatures. Then the steady thermocapillary flows will be toroidal circulations as sketched below.

53

We have recently obtained preliminary numerical results for
this problem, including the effect of surface deformation
(Ca $\neq$ 0), by the method of finite elements. Details of this
work will be forthcoming.

III. INDUSTRIAL FLOAT ZONE CRYSTAL GROWTH

FLOAT ZONE SILICON FOR IR DETECTORS

E. L. Kern

Dr. E. L. Kern, Hughes Aircraft Company, was asked to give an overview of the state of the art of processing silicon for use as infrared detectors and to consider what sort of improvements in the process could be obtained in a low-g environment. He began by summarizing the various requirements for the different types of Si detector materials.

For visible or near IR, the material of choice is high-resistivity Si, with resistivities from 5 to 30 kΩ-cm. Avalanche photodiodes and PIN diodes to detect light in the 0.9 to 1.06 μm range use p-type Si with resistivities in this range. These are used in very sensitive imaging arrays, laser range finders and guidance detectors. The high-purity requirements require a float zone process to avoid crucible contamination problems. The performance depends greatly on the uniformity of the material which, in turn, depends on the solidification process.

In the 3 to 5 μm range the interest lies primarily in Si:In and Si:Tl with dopant concentrations up to 10^{17} cm^{-3}. These dopant levels are difficult to achieve because of their limited solubilities and high segregation coefficients. Constitutional supercooling becomes a problem in the solidification process.

In the 8 to 14 μm range, Si:Ga is required in concentrations of 10^{16} to 10^{17} cm^{-3}. Here the problem is not so much getting the Ga into the Si, but in controlling the uniformity and impurities. For example, there must also be a uniform background of P in concentrations of 10^{11} to 10^{12} cm^{-3}. Less P than this, such that the residual boron is not overcompensated, requires operating temperatures below 8°K. Higher concentrations kill the majority carrier lifetime.

For 18 to 22 μm, shallow dopants such as As, B, and P are required. In all cases, the emphasis is on a high degree of uniformity, especially for focal plane array applications. Starting arrays with 32 x 32 elements are presently available, and 64 x 64 arrays are under development. Ultimately, arrays with 10^6 or more elements will be required. The signal processing requirements from such an array are formidable at best, and the additional burden of having to correct for varying sensitivities must be avoided if possible. This is the primary driver for improved homogeneity in detector materials.

Good carrier lifetime is important in obtaining the required detectivity and demands control of defects and impurities. In addition, most spaceborne detector materials as well as solar cells and signal processing devices must also have good radiation resistance. Defects caused by energetic particles will heal unless they are pinned by impurities. It is believed that electrically neutral impurities

such as C and O may be responsible for pinning such defects. Therefore, these concentrations should be kept as low as possible for radiation-resistant material.

Dr. Kern summarized the various techniques for producing detector grade Si; i.e., Czochralski, float zone, and cold crucible method. In float zone, the grown crystal is usually 2.5 to 5 cm diameter. RF heating is used, and the work coil is shaped to provide an hourglass melt configuration approximately 25 mm diameter at the narrowest region. This is shown schematically in Figure 1. Figure 2 is an actual photograph of a crystal being grown by the float zone process. Figure 3 is a typical float zone growth facility.

The primary advantage of the float zone process is the purity levels that can be achieved. Crucible contaminants are avoided, and volatile constituents can be driven off by making several zone passes in vacuum before the final growth pass. The growth pass is usually made in Ar with carefully controlled pull rate and neck-down after seeding to obtain dislocation-free material.

The primary problem with float zone material is the inhomogeneities in the composition of the material. Figure 4 compares the radial spreading resistance profile of Hughes detector grade intrinsic silicon with material grown by Wacker. Although the Hughes material is much more uniform on a macroscopic scale, both materials exhibit substantial fluctuations on a microscale which would affect the performance of a device such as a focal plane array. The axial uniformity of the Hughes material is shown in Figure 5.

With heavily doped Si, the microscopic inhomogeneities are even more pronounced. Figure 6 shows the radial profile of a slice of float zone Si:Ga. Figure 7 shows details of the structure of the striations in an etched silica of the wafer. Notice that the large (50 percent) variations tend to repeat every 280 μm. This translates into 230 μm in the growth direction ($\langle 111 \rangle$), which is the distance traveled by the ingot during one rotational period. These fluctuations may be attributed to the gap in the work coil which is located between the RF feed points. The resulting asymmetry in radiated power causes growth fluctuations in the material as it rotates.

Superimposed on the rotational striations is a series of smaller fluctuations corresponding to differences of 20 percent with a periodicity corresponding to 333 μm in the growth direction. These are attributed to thermal fluctuations and are believed to be the result of some sort of convective instability. The result of these striations on detector performance may be seen in Figure 8.

Czochralski growth produces much more uniform material, as may be seen by comparing Figure 9 with Figure 10. The rotational striation from the work coil is, of course, eliminated, and it also appears that the thermal fluctuations have been greatly reduced. Figure 11 shows a

FLOAT ZONE
CRYSTAL GROWTH

POLYCRYSTAL
ROD

R.F. ZONING
COIL

⊥ ROTATIONAL AXIS
AND CRYSTAL AXIS

MOLTEN ZONE

VACUUM OR
ARGON GAS
ATMOSPHERE

DISLOCATION FREE
SIGNAL CRYSTAL

GROWTH RATE
2 TO 5 mm/min
(5 - 12 in/h)

ROTATIONAL, COIL AND CRYSTAL
AXES MUST COINCIDE

SEED
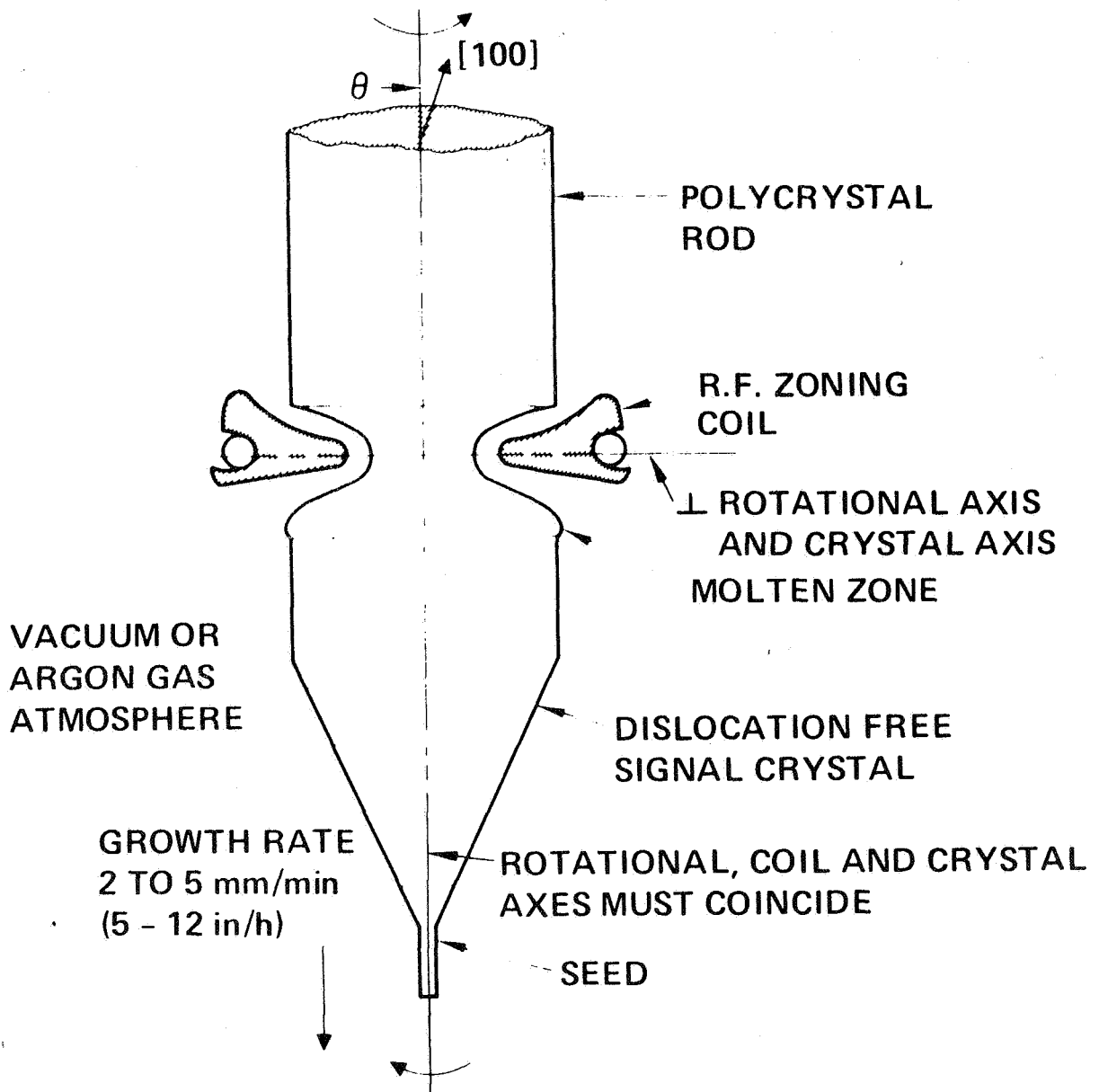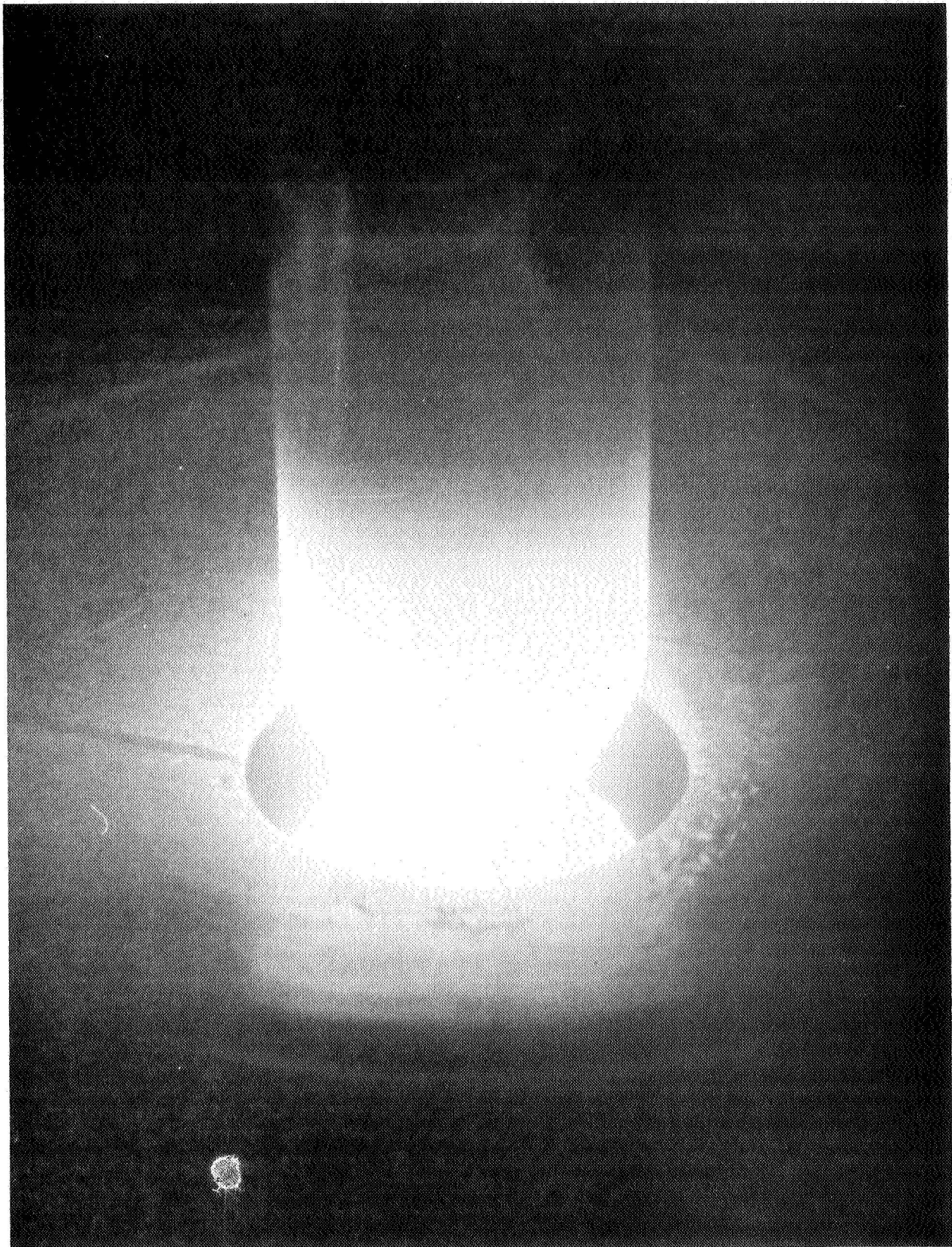
Figure 1

Figure 2. Crystal being grown by float zone process.

60
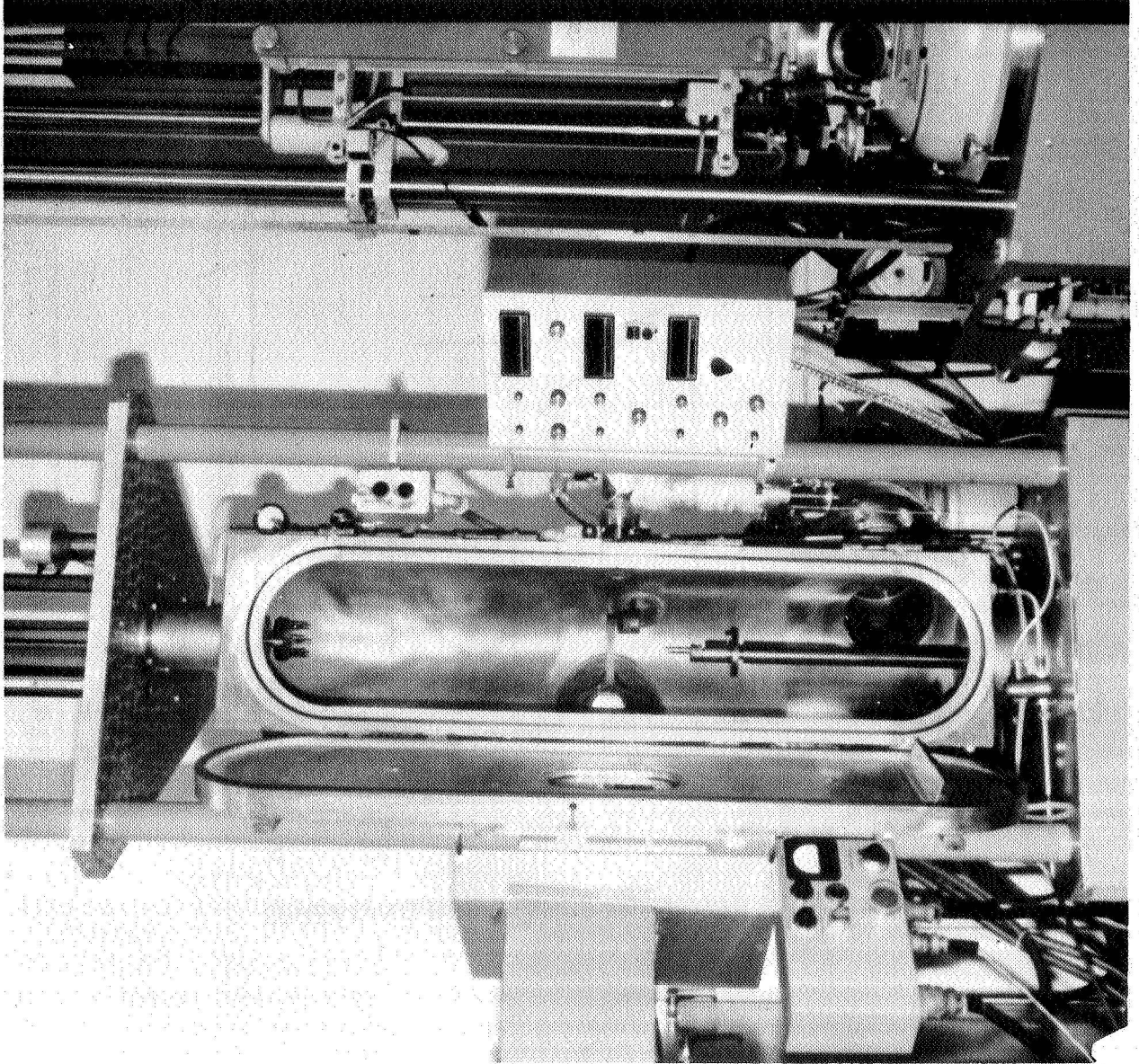
Figure 3. Float zone growth facility.

61

HUGHES DETECTOR GRADE SILICON HAS MUCH LOWER RADIAL SPREADING RESISTANCE GRADIENT
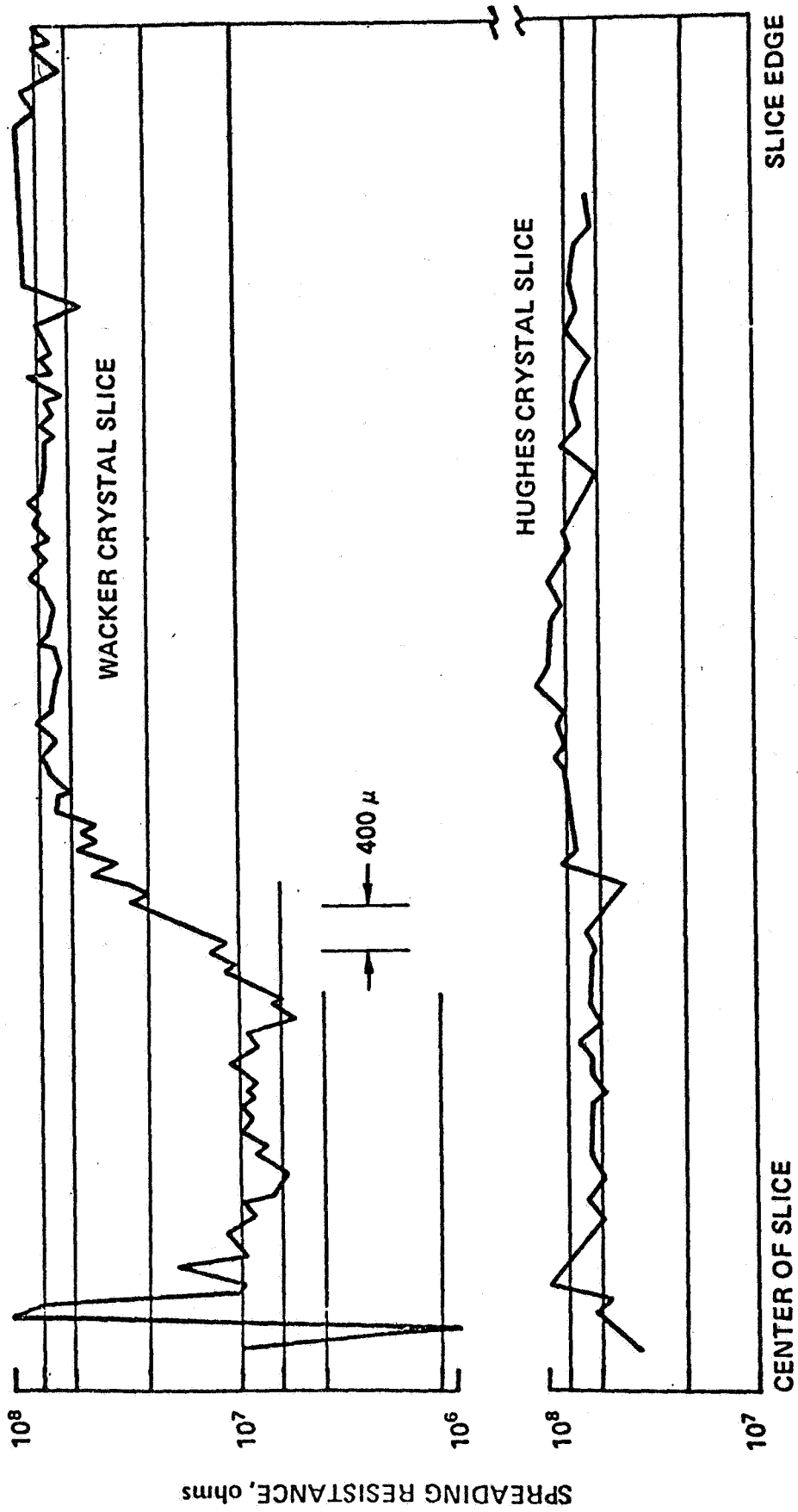
Figure 4. Hughes detector grade intrinsic silicon.

62
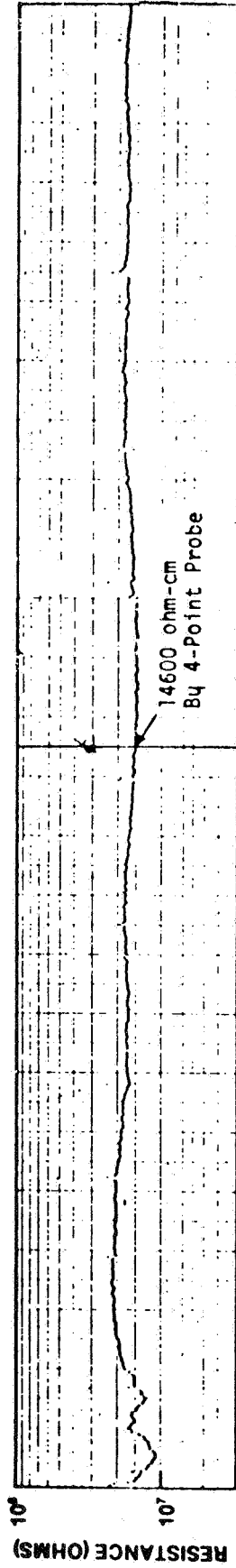
Spreading Resistance Profile of Polished Wafer

Figure 5

SPREADING RESISTANCE PROFILE
FLOAT–ZONED Si:Ga <100>

SPREADING RESISTANCE PROFILE
FLOAT–ZONED Si:Ga <100>
2 in. diam RADIAL PROFILE
40 μm STEPS II TO <110> FLAT
CRYSTAL Z-20401 (AT HRL)

FIRST PART OF TRACE
SECOND
THIRD
800 μm

DISTANCE ALONG DIAMETER OF SLICE →

SPREADING RESISTANCE, ohms

Figure 6

HUGHES
HUGHES AIRCRAFT COMPANY
RESEARCH LABORATORIES

4766–7

64
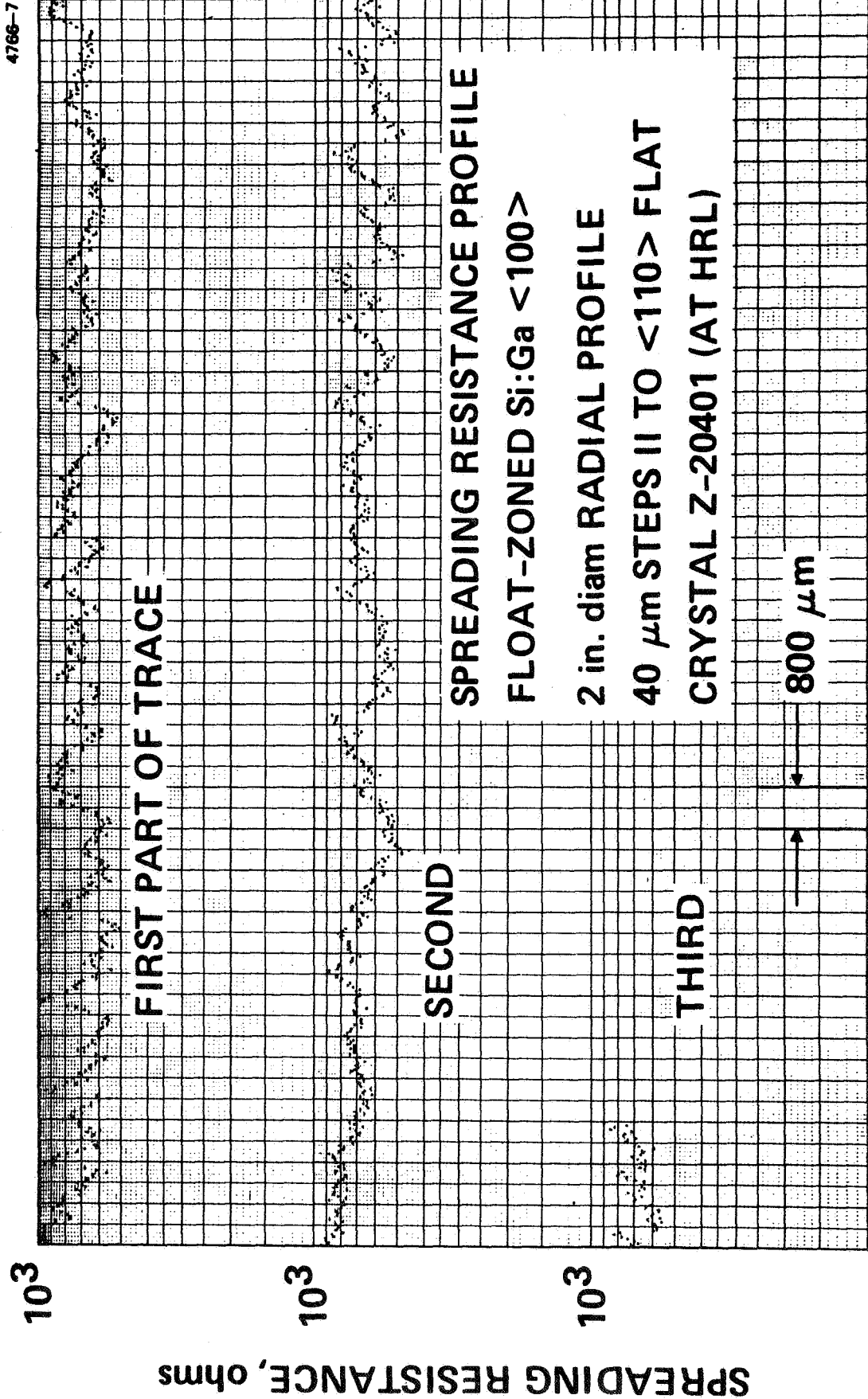
Si:Ga SPREADING RESISTANCE

[100] SLICE CUT FROM [111] INGOT

2 PARALLEL PLOTS 10 μm APART/POINTS TAKEN 5 μm APART

THERMAL FLUCTUATIONS
20% CONC DIFFERENCE

270μ

280μ

50% CONC DIFFERENCE
1.5 → 2.5 x 10^{16}

280μ

280μ
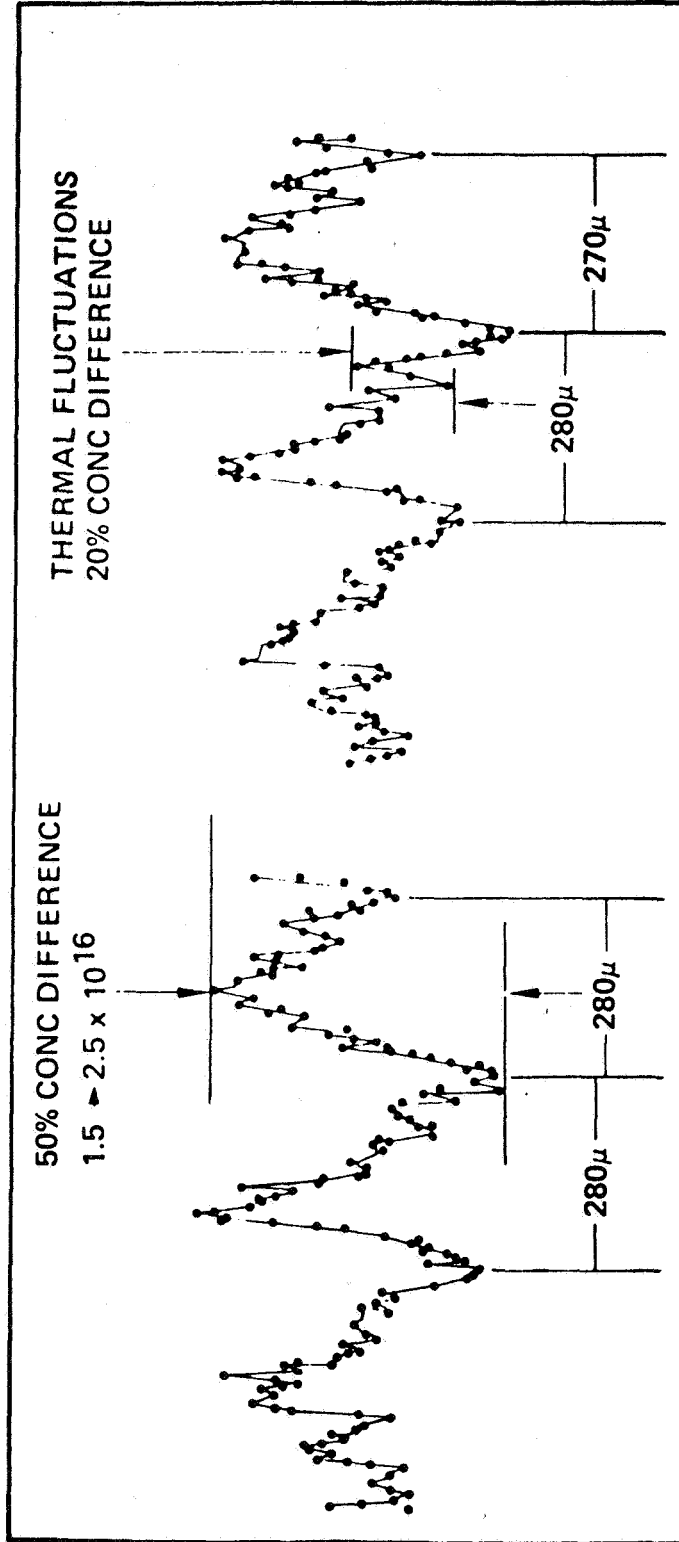
MAJOR STRIATIONS 280 μm APART → 230 μm IN <111>DIRECTION

MINOR THERMAL FLUCTUATIONS 40 μm APART → 33 μm IN <111>DIRECTION

Figure 7

65
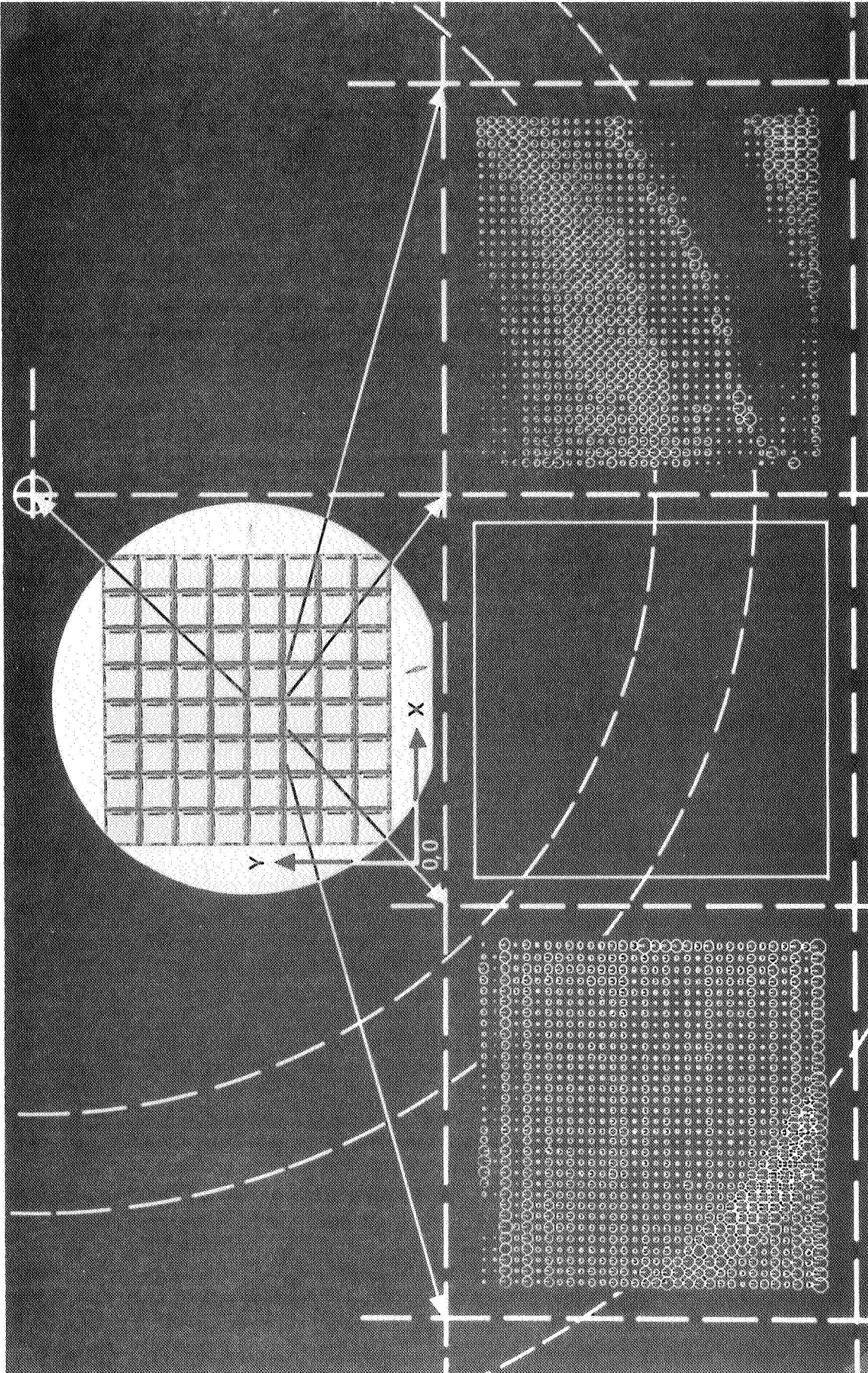
Figure 8. Si:In wafer striations (2101 lot 20, wafer D, parts 3,3 and 5,3; ingot C003 - Hughes).

66

SPREADING RESISTANCE PROFILE
CZOCHRALSKI GROWN Si:In <100>

HUGHES

HUGHES AIRCRAFT COMPANY
RESEARCH LABORATORIES
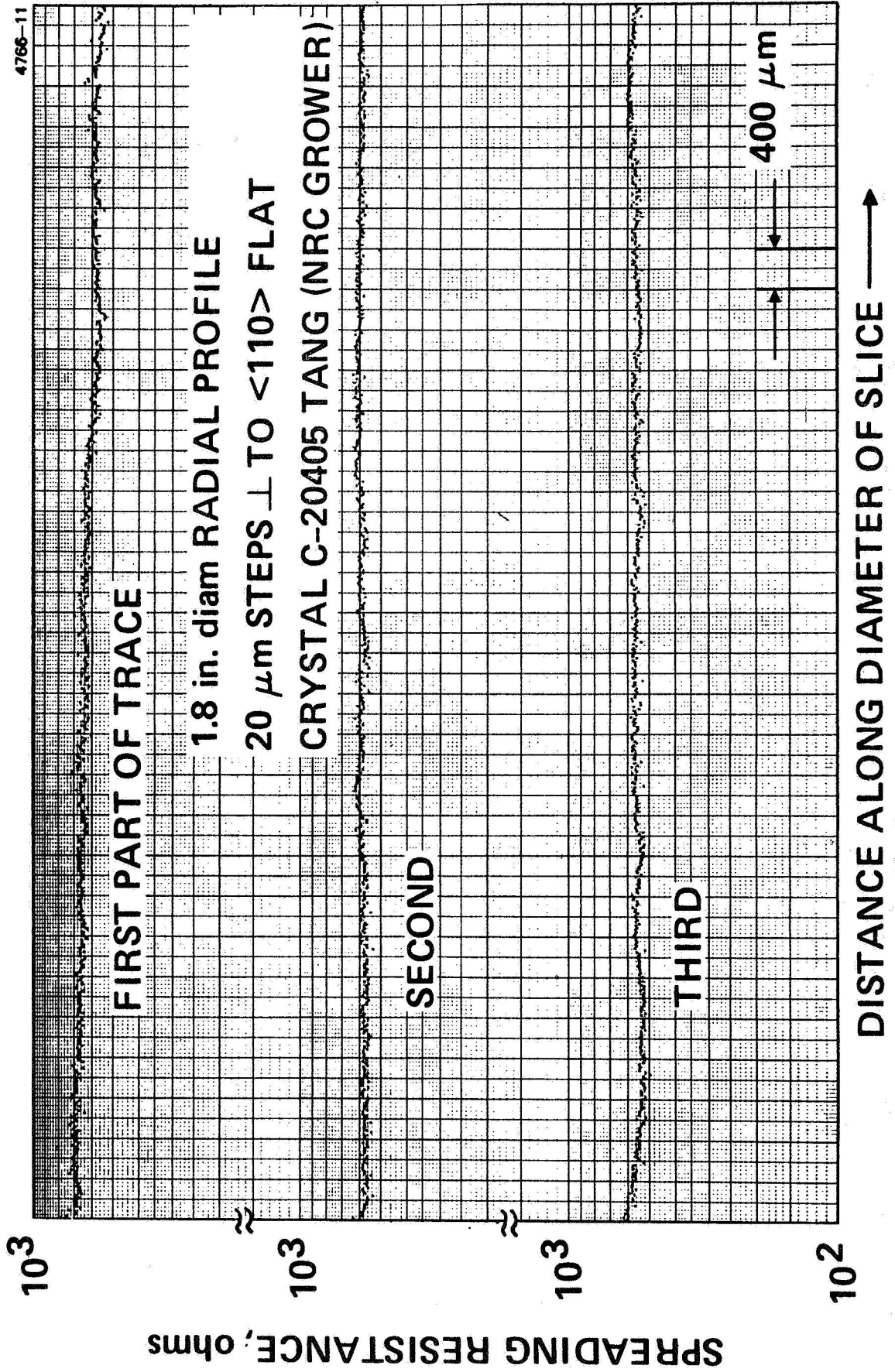
4766-11

FIRST PART OF TRACE

1.8 in. diam RADIAL PROFILE

20 μm STEPS ⊥ TO <110> FLAT

CRYSTAL C-20405 TANG (NRC GROWER)

SECOND

THIRD

400 μm

10^3

10^3

10^3

10^2

SPREADING RESISTANCE, ohms

DISTANCE ALONG DIAMETER OF SLICE ——▶

Figure 9

67

SPREADING RESISTANCE PROFILE
FLOAT-ZONED Si:In <111>

1.2 in. DIAMETER RADIAL PROFILE

20 μm STEPS

CRYSTAL Z–20101

800 μm

SPREADING RESISTANCE, ohms

10^3 10^3 10^3

DISTANCE ALONG DIAMETER OF SLICE

Figure 10

HUGHES

HUGHES AIRCRAFT COMPANY
RESEARCH LABORATORIES
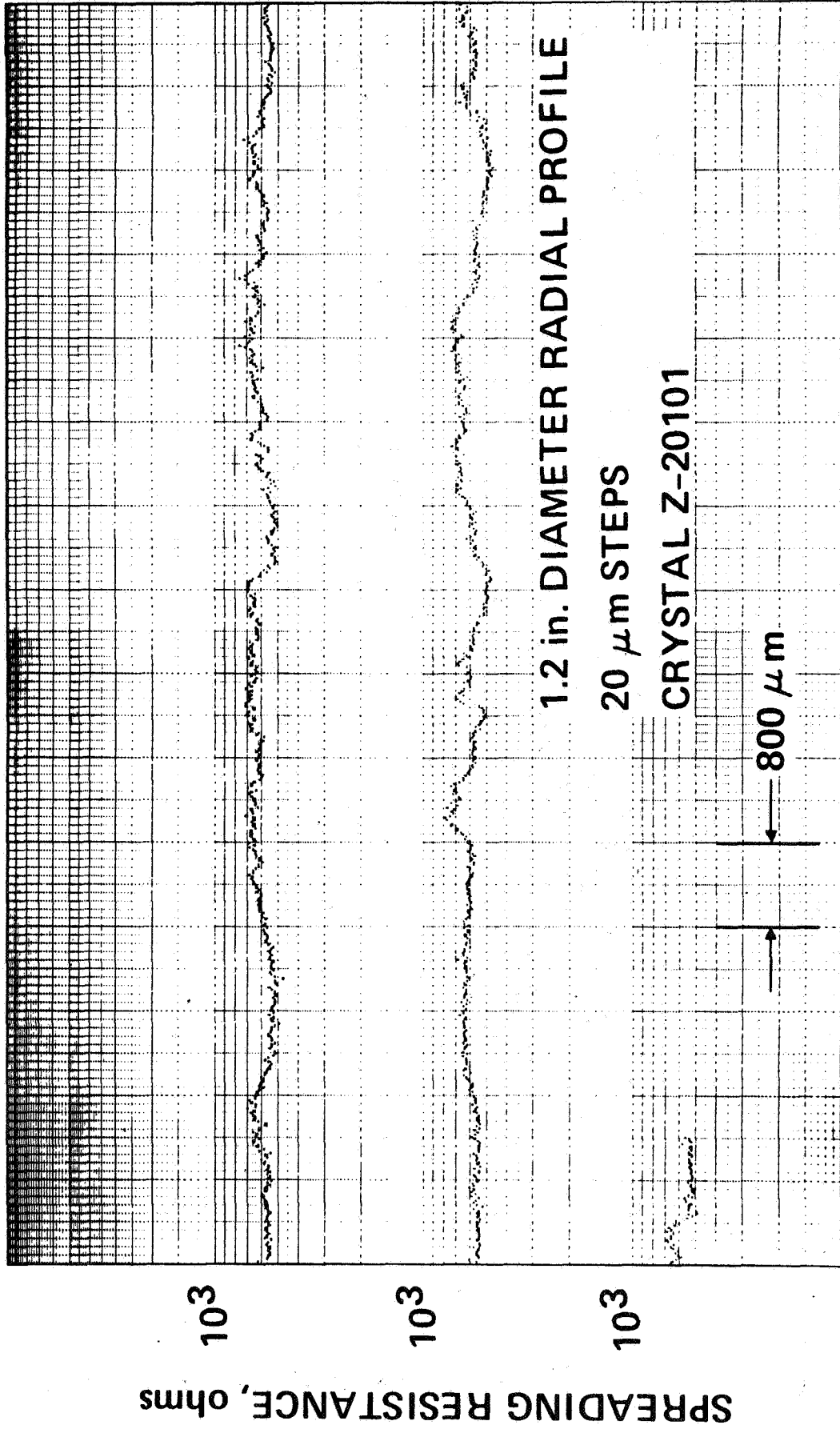
4766–10

Si:In <100> CZOCHRALSKI GROWN

MICROPRECIPITATES THROUGHOUT
CRYSTAL 3.0×10^{17} AND POLYCRYSTALLINE

2.0×10^{17} MICROPRECIPITATES START

$[I_N] = 1.0 \times 10^{17}$

1.75 inch DIAMETER

CRYSTAL 20302
$k_{eff} = 1.1 \times 10^{-3}$

Figure 11

HUGHES

HUGHES AIRCRAFT COMPANY
RESEARCH LABORATORIES

4140–12

M-10935

cross section of an ingot of Si:In that illustrates the difficulty in growing heavily doped Si:In. Because of the low k_{eff}, the concentration of In in the melt increases during the growth process. Microprecipitates begin when the concentration reaches 2.0×10^{17} cm^{-3} because of compositional supercooling. When the concentration reaches 3.0×10^{17} cm^{-3}, the material becomes polycrystalline and microprecipitates are found throughout. The most serious problem with Czochralski-grown Si, however, is the crucible impurities. These are primarily O, C, B, and P. While these can be tolerated in many devices (indeed, well over 90 percent of Si used for device manufacture is grown by the Czochralski method), they severely limit majority carrier lifetimes and cannot be tolerated in high-performance optical and infrared devices.

One technique that has sought to overcome the crucible contamination problem is the so-called cold crucible method. The melt is supported on the sides by a combination of copper cold fingers and RF levitation. At the bottom the melt is supported either by a H_2O cooled pedestal or by a rod of Si feed stock. In this technique molten Si contacts only solid Si, just as in the float zone process. Growth, however, is by pulling a crystal from a molten pool, just as in the Czochralski method. Figure 12 shows a cold crucible assembly.

This technique combines the best features of float zone with Czochralski. Its primary weakness is the high thermal gradient associated with the heat loss through the solid. This requires considerable superheating of the molten Si, which tends to drive off the volatile dopants such as In, Ga, or Tl.

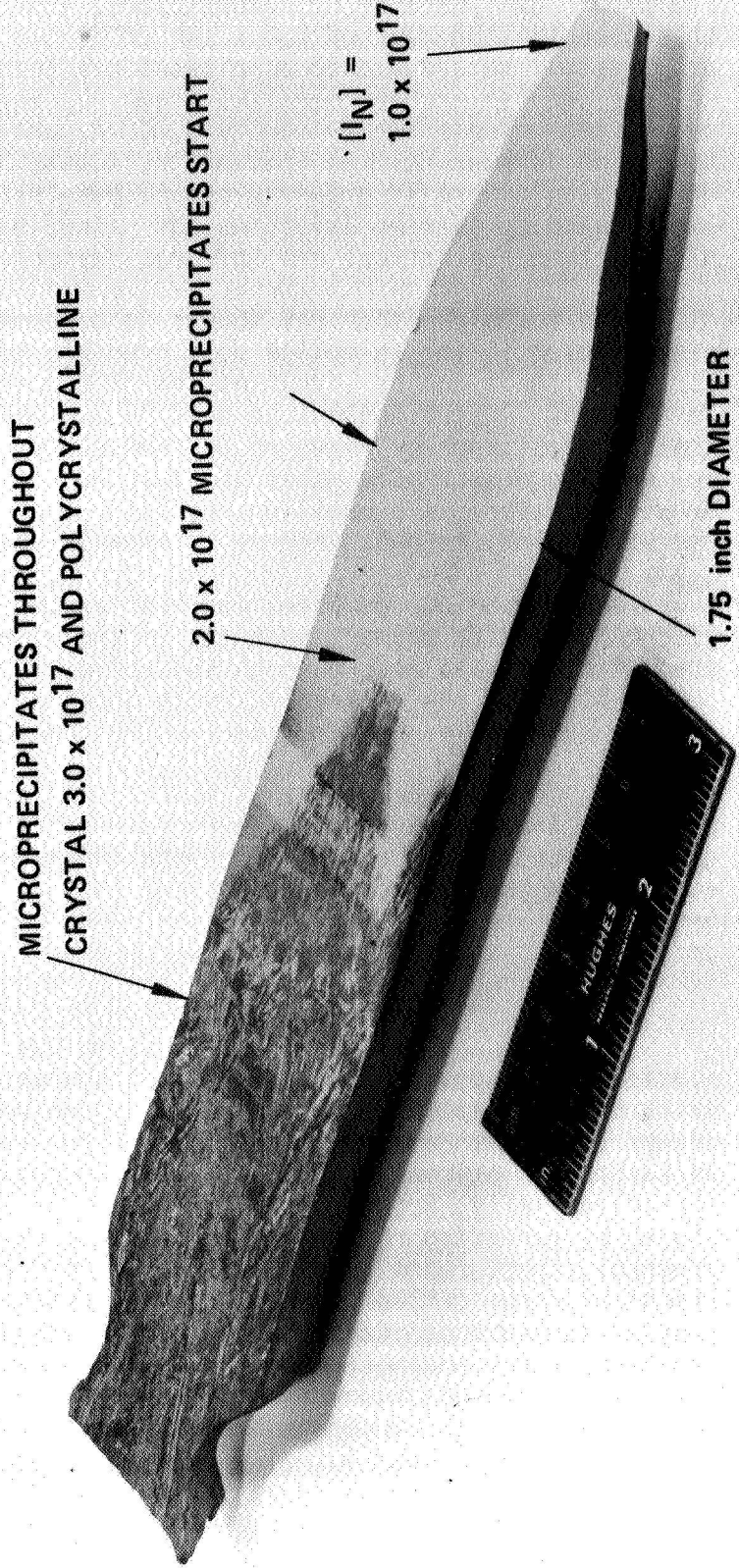Dr. Kern pointed out that most of the industrial advances in growth technology have come about empirically and that analysis of the growth process has not kept pace with these developments. Idealistic modeling of the melt dynamics has led to some understanding, but it is very incomplete. Physical constants, such as emissivities, viscosities and surface tensions, are not known, making a precise energy and dynamic analysis impossible. Real zone shapes have not yet been analyzed.

Even the analysis of impurities, in the ranges of interest for electrooptical devices, is inadequate; however, there are prospects which need developing. The sensitivity and spatial resolution for groups III and V dopants in silicon and for nonionizing impurities such as carbon and oxygen are of particular concern. Ga and In can be mapped spatially, according to the extent of ionization at room temperature, by spreading resistance in a semiquantitative manner. Boron and phosphorus background impurities in the 10^{11} to 10^{13} atoms/cm^3 range can be measured by Hall effect, but only with 1 cm spatial resolution. Carbon and oxygen in the 10^{12} to 10^{14} atoms/cm^3 range are not presently measurable, although a wavelength-modulated infrared absorption technique appears promising. Methods which measure light absorption or emission (photoluminescence) or charge detrapping (DLTS) are appropriately sensitive to impurity and

COLD CRUCIBLE ASSEMBLY
IN CHAMBER

HUGHES

Figure 12

71
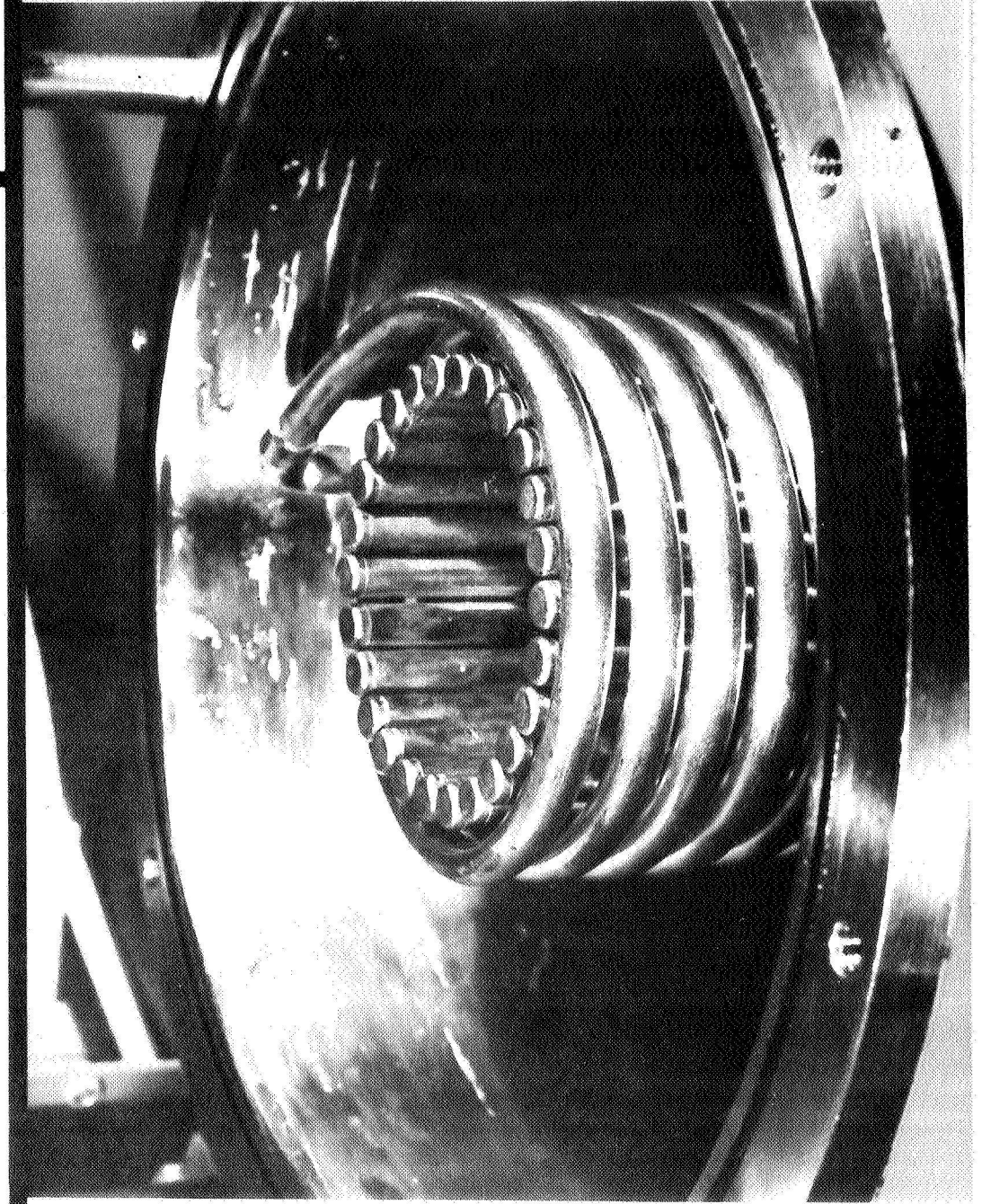
defect sites, but chemical and physical identification must still be correlated.

Dr. Kern believes that flight experiments in float zone crystal growth hold some exciting possibilities. The freedom of molten zone configurations provided for by the absence of hydrostatic pressure could be used to advantage in providing better control of the heat flow, surface area, and thermal gradient at the interface. He recommended that such an effort should initially concentrate on the Si:Ga system and later extend to Si:In.

The characteristics of the silicon float-zone melt need to be accurately modeled. This understanding of heat balance and flow, of isotherm shapes, of density (including a density possible inversion), and of surface tension variations with temperature will lead to better methods of controlling the growth conditions. In particular, the instantaneous growth velocity should remain constant. This requires the development of an RF heating coil without the present slot and could require the use of a dc magnetic field to suppress melt flows. These improvements should be designed, constructed, and tested in float zone experiments. The effects of frequency on levitation should also be modeled and tested to maximize melt volume.

The emissivity of molten and solid silicon is not adequately known and needs to be measured. Real float zone shapes should be modeled for dynamic and steady-state characteristics, and additional melt parameters should be measured where necessary for accurate modeling.

The overall impurity levels and spatial variation of dopants need to be characterized using resistivity and spreading resistance, IR absorption, and striation decoration. Occasional analysis by Hall effect and other methods can be used to confirm concentrations. Striation decoration would be used to define the growth interface shape as it changes from seeding to steady state growth conditions.

The phase diagram of the Si:Ga system near the maximum solubility limit needs to be better defined, especially as it is a retrograde solubility. Solar cells require Ga up to 5×10^{17} atoms/cm^3 (0.1 ohm-cm). Such information is needed to determine segregation coefficients and to estimate conditions resulting in constitutional supercooling. This will establish the time-temperature conditioning required for growing the crystals and will provide information on maximum concentration and feasible growth rates.

Such an effort can be expected to provide valuable in-depth understanding to the present Si growth technology as well as to offer the prospect of obtaining superior detector material grown in a low-g environment.

FLOAT ZONE REFINING: SPACE PROBLEMS AND SOLUTIONS -- A SPECULATIVE PROPOSAL

G. L. Gill

Dr. Gerald Gill, President of Westech Systems, Inc., represents the major supplier of float zone apparatus in the U.S. He was asked to consider how he might go about designing a float zone facility for use in the Shuttle. He is presently developing a system in conjunction with Hughes Aircraft to be delivered to the Army for the automatic growth of 60 cm long boules of Si up to 10 cm diameter. The facility is 21 ft tall, weighs 17,000 lb (without the sand ballast), and consumes 60 kW power. As a point of reference, the facility will cost approximately $500K without the automation which will be developed by Hughes. The total price is expected to be approximately $1.2 million.

One of the major problems in the development of a space facility is the enormous power required to melt moderate diameter floating zones. Dr. Gill reported that typically 27 kW input to the RF oscillator was required to pass a zone through an 8 cm diameter Si rod. Additional power will be required to make up the power conversion losses to go from Shuttle dc power to the high voltage required for the oscillator input. If substantial 400 Hz power were available, the conversion losses would be lower. With only 5 kW input, it was estimated that only 2 kW would be available at the work coil; and, based on the performance of an early Siemans system, Dr. Gill estimated that only 1 cm diameter crystals could be accommodated. Some improvements which may be possible, such as the use of ferrite core transformers to minimize losses may save some 20 percent of the system losses. Also, it may be possible to minimize radiation losses from the zone itself by use of reflectors. However, it does not appear that crystals much larger than 1.5 cm diameter can be grown in space until more power is available.

Dr. Gill recommended a 3-phase program with overlapping phases. In Phase I, a process study would be conducted using a "standard" zone refiner to explore coil design and power transfer efficiency studies and to develop the necessary remote and/or automatic operations that would be required for space applications. Phase II would run concurrently with Phase I and would consist of the design and construction of a prototype system that would optimize power transfer and test the remote operation of the actual flight system. Design could begin as soon as 8 to 12 months after Phase I, and construction could begin in the 14- to 18-month time frame. Total time required was estimated to be 36 months from Phase I go-ahead.

Most of the thinking was predicated on RF heating primarily because that is the most widely used technique for heating silicon. Several of the major issues that must be resolved are: (1) How much stirring is produced by RF heating? (2) Can the slot be eliminated by coupling into a single turn coil? (3) What is the optimum zone shape

and coil design for low-g operation? Other means of heating might be considered but appear to have various shortcomings. E-beam heating is perhaps the most efficient but requires a good vacuum and is not compatible with the Ar atmosphere used to achieve dislocation-free growth. Various radiant heating schemes may be possible but generally have lower overall efficiency than RF.

Other issues that must be considered are the requirement to change samples, seeding and initiating growth automatically or by remote viewing and manipulation, isolation from vibration, and control of spills in low-g. Several systems have been automated to control growth automatically once the seeding operation has been successfully completed, but no one has yet developed a system for changing samples or for seeding and initiating growth without direct operator intervention.

Vibration isolation is a major problem in industrial float zone growth, which accounts for the fact that most commercial units are mounted on isolation pads and are heavily ballasted to reduce vibration. Since free surfaces are inherent to the process, any small vibration will cause distortion of the zone shape and may result in growth fluctuations.

Spills of a molten zone also occur even under the most careful operations. In conventional practice on Earth, the nature of the spill is predictable, and damage can be minimized by appropriate precautions. However, in space, if the zone becomes detached, there is no way to know where it may go.

It appears that the problems of building an automated or remotely operated float zone growth facility are formidable but manageable. Westech would be interested in working with NASA to develop such a facility.

PRACTICAL ASPECTS OF SILICON FLOAT ZONE CRYSTAL GROWTH

T. F. Ciszek

Dr. T. F. Ciszek, Solar Energy Research Institute (SERI), was invited to give a presentation on some of the practical aspects of growing Si by the float zone process, particularly with regard to the control of purity and defects. The text of his presentation follows.

Introduction

The float zone (FZ) growth method for silicon crystallization has advantages and disadvantages when compared to the other principal growth method, the Czochralski (CZ) technique. CZ growth is attractive for the following reasons: large diameters, high single crystal yields, low thermal gradients, low operator skill requirements, efficient power utilization, and low feed material costs. Some areas where FZ growth is advantageous include high purity, axial resistivity uniformity (on a macroscale), visibility of the growth region, low consumable material costs, and high growth rates.

Ironically, one of the reasons FZ material has not found more application in the device industry is because of its low oxygen levels and, hence, the alterations required in processing techniques. Other reasons include the generally higher cost of the process due to lower single crystal yields, and the generally smaller FZ diameters compared to CZ technology. The main fields of application include power devices, where high breakdown voltages are attainable, and radiation detectors, where control over undesired impurities is essential.

Growth Ambient and Purity Considerations

FZ growth may be carried out in vacuum, inert gas, and reducing gas environments. The ambient has an influence on defect generation and the ability to maintain single, dislocation-free growth. Both vacuum and reducing atmospheres are poor choices in this regard. Purification, however, can be significantly influenced by growth in a vacuum ambient because many impurities have a large evaporation coefficient, g, which acts in conjunction with the effective segregation coefficient, k, to achieve purification:

$$\frac{C_n}{C_o} = \left(\frac{k}{k + g}\right)^n \left[1 - (1 - k - g)\ e^{-(k+g)x}\ Z_n\right]$$

where

$$Z_n = n - \sum_{s=1}^{n-1} (n - s)(k + g)^{s-1}\ e^{-s(k+g)}\ \frac{(s + x)^{s-2}}{s!}$$

$$\left\{(s - 1)x + (s + x)[1 - (k + g)x]\right\}$$

and

    n = number of zone passes

    x = distance along rod in zone lengths

    C_0 = original uniform impurity concentration

    C_n = concentration after n passes.

Reasonably flat profiles are seen for the dopants boron, phosphorus, arsenic, and gallium after several zone passes. If g is < 0.1, evaporation does not strongly affect the impurity profile.

Growth Characteristics

Large Si FZ crystals must be dislocation-free to avoid complete degeneration of the single crystal structure during growth. To initiate dislocation-free growth, a necked region typically < 3 mm in diameter and > 20 mm in length is grown from the seed. This creates mechanical stability problems as the crystal weight increases.

Dislocation-free silicon is partially singular and partially rough in its growth morphology. The (111) planes with three nearest in-plane neighbor atoms tend to be singular and are the low-surface-free-energy planes. When the freezing isotherm is nearly parallel to (111), supercooling on the order of 5° to 10°C and accompanying facets occur on the interface. Two-dimensional surface nucleation and rapid lateral growth are characteristic of this region of the interface. Normal growth predominates on the remainder of the interface. Dopant incorporation is significantly enhanced on the singular regions of the interface if k is far from one. External crystal surface morphology is also affected by singular regions near the periphery of the solid/liquid interface. Particularly for <111> crystals, longitudinal meandering bulges form on the crystal surface.

Defect Characteristics

Dislocations are gross defects in float zone crystals. During growth in a vacuum ambient, they can be nucleated by particulate solid silicon which had previously been vapor deposited on the work coil and other surfaces near the liquid zone. Once nucleated, dislocations multiply and rapidly degrade the single crystal. One theory also postulates that evaporation roughening of the hot crystal surface just below the interface enhances the probability of dislocation nucleation. In any ambient, thermomechanical stresses exceeding the critical shear stress will nucleate dislocations. Multiplication can occur at much lower stress values.

In dislocation-free crystals, localized or point-like defects are present in a helically striated arrangement and are called swirl

defects. Much study has been devoted to this defect because it can influence device performance, especially if it is associated with impurities. Such defects were first believed to be vacancy clusters. A later model proposed vacancy/oxygen complexes. Current thought is that silicon self-interstitials are the source of the defects. Collapse of the interstitials gives rise to dislocation loops of several microns in size. There is still debate over the interstitial incorporation mechanism, explanation of the time/temperature behavior of the defects, and the role of impurities. Carbon may play a role in their behavior.

Other silicon defects include hydrogen cluster formation when a hydrogen ambient is used, and large-area etching depressions covering perhaps the central one-third of large-diameter (> 50 mm) wafers. The hydrogen clusters are harmful to devices; the etching depressions generally are not.

A clean argon ambient, a low axial temperature gradient, good rotational thermal symmetry, fast growth rates, and low carbon levels all contribute to controlled defect-free growth. There is no apparent limit to crystal size, provided that (1) the external zone length does not exceed 25 to 30 mm while melting through the interior of the feed rod, (2) heat of fusion can be extracted from the interface region, and (3) thermomechanical stresses can be held to sufficiently low levels.

FUTURE FLOAT ZONE DEVELOPMENT IN INDUSTRY

R. M. Sandfort

Dr. Sandfort, Monsanto Company, represents a major industrial supplier of float zone Si. He was invited to summarize the present industrial requirements for float zone silicon and to comment on developments desired by the industry in the future. The text of his presentation follows.

The five most significant problems faced today by the float zone crystal growth method in industry are:

1. Economic

2. Larger Diameter

3. Resistivity Uniformity

4. Control of Carbon

5. Swirl Defects

I would like to consider these one at a time.

First Factor: Economic

Historically, float zone (FZ) and Czochralski (Cz) materials were sold indiscriminately into the IC market and the power device market. However, as both markets have become more sophisticated, their unique requirements have been recognized. Float zone material is now sold mainly into a specialized market which requires high reverse break-down voltages. Very little FZ material is sold into the IC market.

The same reason why FZ material is preferred for power device applications, its low oxygen content, is the reason why it is not preferred for the IC market.

Oxygen in Cz material tends to precipitate on native defect sites at a rate which is a function of the thermal history of the material. These precipitates can be thought of as causing local sharp band energy fluctuations. The result is a lowering of the break-down voltage. Float zone material, which has a very low oxygen concentration, is thus able to support break-down voltages of a few thousand volts or more.

By contrast, this precipitated oxygen in Cz material is advantageous as an internal gettering mechanism for many fast diffusing atomic species which limit MOS recovery time.

Therefore, because the FZ material has been found less suitable to IC applications and since the IC market has expanded much more

78

rapidly in recent years than the power device market, the FZ business has not been as attractive economically. Coupled with this is the fact that the float zone crystal growth process has been a more difficult one from an operator standpoint. More operator skill has been required, greater demands on poly quality have existed, and less zone refining equipment has been available commercially. Thus, fewer companies have elected to participate in the FZ material business, which has slowed technical development. The area has been particularly unattractive to those companies lacking backward integration into poly silicon.

Second Factor: Increased Diameter

Many power devices are made from an entire wafer of silicon. For years this has meant a reluctance for some device makers to change to larger diameter wafers. However, with the advent of microprocessor-controlled laser scribers, device sized polygons can be scribed from larger wafers. This, plus an emerging market for larger power devices, has meant a need for larger diameter ingots.

For companies operating a pedestal pulling type of process, which appears to be limited theoretically to ingots approximately 2.5 to 3 inches in diameter, this has meant a major change in their process.

Even for conventional float zone, larger diameters are difficult. The chamber size must be larger, the power levels are higher, the opportunity for high voltage plasma and discharge phenomena is greater, the ingot end losses are higher, and the crystal can no longer be supported by the seed alone.

Solutions to all these problems must be found on a continuing basis as diameters are increased.

Third Factor: Resistivity Control

As the device maker has become more sophisticated in his ability to improve his device performance, he has found the need for ever tighter control over resistivity variations. This tighter control is both axial and radial.

The answer for many of these device applications is neutron transmutation doping (NTD) which is capable of uniform doping to about ± 10 percent. Because this process presumes a uniform volume distribution of Si^{30}, the only sources of resistivity variation are nonuniform neutron flux profile in the reactor and unpredictable fluctuations in polycrystalline base level.

For some applications requiring tight resistivity control and high minority carrier lifetime, NTD may not be the answer. Associated with the momentum exchange occurring during a collision of a neutron with the silicon lattice is a measurable amount of lattice damage.

This damage can have a marked effect on minority carrier lifetime, lowering it by more than an order of magnitude under some conditions. A post-doping heat treatment is used to anneal out some of this damage in order to reestablish a reasonable minority carrier lifetime. But for some applications, this lifetime value is still too low. There is an on-going need then to develop methods other than NTD for achieving better dopant distribution in float zone ingots. Research on those growth parameters which control microsegregation of dopant is important.

Fourth Factor: Control of Carbon

In recent years, increasing concern has been voiced by power device makers over the roll of carbon in float zone material. Particularly from Japan and Europe have come reports that carbon must be held to less than a few parts per million.

Impurity control has always been one of the key advantages of the float zone crystal growth method. The level of impurities such as carbon which are reasonably strongly segregated by the crystallization process theoretically can be lowered to arbitrarily low values. Practically, however, there is an economic limit to the number of zone passes which can be made.

Also, there is an insidious aspect of carbon in that it can enter the ingot once in the form of contaminated poly or mishandling by an operator, or it can enter the ingot continuously from a contaminating zone refiner. Carbon levels will have to be reduced in the future. The various avenues of carbon entry into the ingot must be located and measures taken to eliminate them.

Fifth Factor: Swirl Defects

For some applications of float zone material, such as in vidicon tubes and CCD imagers, it is important to control the surface defect level. A swirl-type defect, which is similar to the shallow pit developed in Cz slice surfaces after an appropriate etch, sometimes exists in float zone material as well. This defect is quite different in appearance from what was referred to as swirl in float zone some years ago.

Only preliminary conjectures have been developed to date on the reasons why this defect forms and how to control it. But it is expected that this problem will receive significantly greater research attention in the near future.

I have tried to summarize for you five areas of major concern to industrial float zone material suppliers. The answers to these concerns, whether found in government R&D labs or those of private industry, could markedly benefit the electronics industry.

FLOAT ZONE GROWTH OF Si IN LOW-G

K. M. Kim

Dr. Kim, IBM East Fishkill Labs, is an industrial research scientist who has substantial experience in many aspects of growth of Si and Ge by float zone as well as the Czochralski method. He was asked to describe some of his work on zone stability and to comment on possible advantages he could see for conducting float zone growth experiments in a low-g environment.

Dr. Kim described a series of experiments to measure the maximum stable length of a floating zone in Si and in sapphire.[1] In the absence of hydrostatic pressure, the maximum stable length was predicted by Lord Rayleigh to be πd, where d is the diameter of the melt. Coriell, Hardy, and Cordes analyzed the stability as a function of Bond number. The Bond number, $B = \rho g d^2/4\gamma$ is the ratio of hydrostatic pressure to surface tension and can be made small by reducing either g or the diameter. Kim used small diameter (1 to 2 mm) float zones in Si and sapphire to test the theory at low Bond numbers, which is fluid dynamically equivalent to performing a larger scale experiment in low gravity.

The zones were melted by a CO_2 laser with a beam splitter, as shown in Figure 1. Approximately 100 watts of laser power was required to melt a 1 mm rod of Si, whereas only 60 watts was required to melt sapphire. This is because of the greater absorption of sapphire at 10.6 μm.

The results are shown in Figure 2 and indicate excellent agreement with the analysis of Coriell, Hardy, and Cordes. Also, it is interesting to note how closely the zero-g limit may be approached by using small zone diameters.

Dr. Kim's comments on float zone experiments to be performed in low-g are as follows:

> Float zone silicon crystal growth has developed steadily since the early 1950's. However, there are still problem areas to be investigated and to be improved further.

> Today float zone silicon crystals of 100 mm in diameter are routinely grown. Further increase in the diameter is limited mainly by the availability of suitable polycrystalline feed rods

---

1. These experiments are described in more detail in Dr. Kim's recent article, "Maximum Stable Zone Length in Float-Zone Growth of Small-Diameter Sapphire and Silicon Crystals," K. M. Kim, A. B. Dreeben, and A. Schujko, J. Appl. Phys. 50 (6), June 1979, 4472-4474.
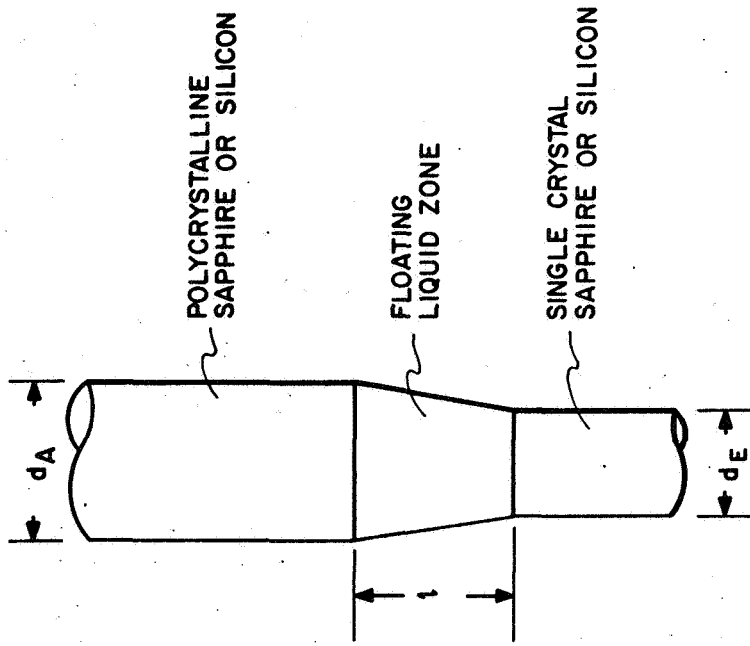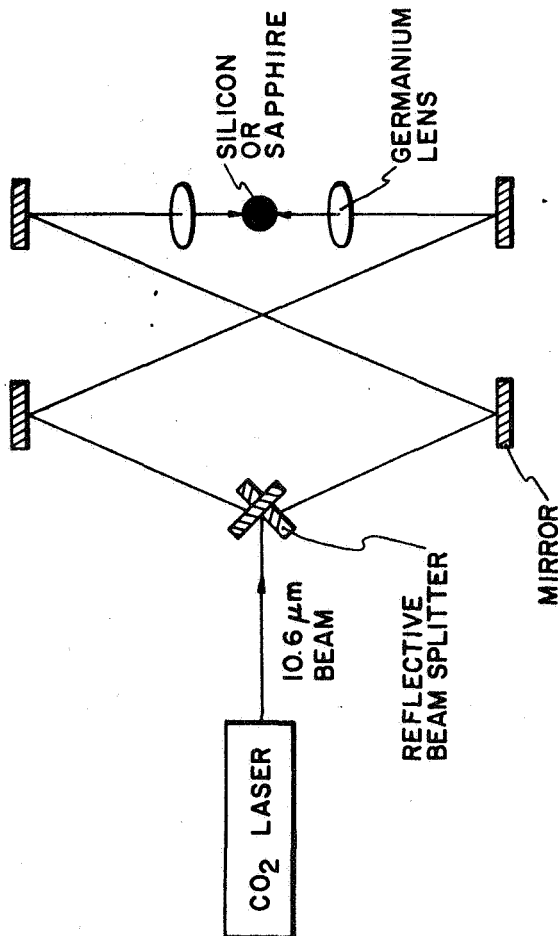
Figure 1. Heating apparatus for float zone experiment.
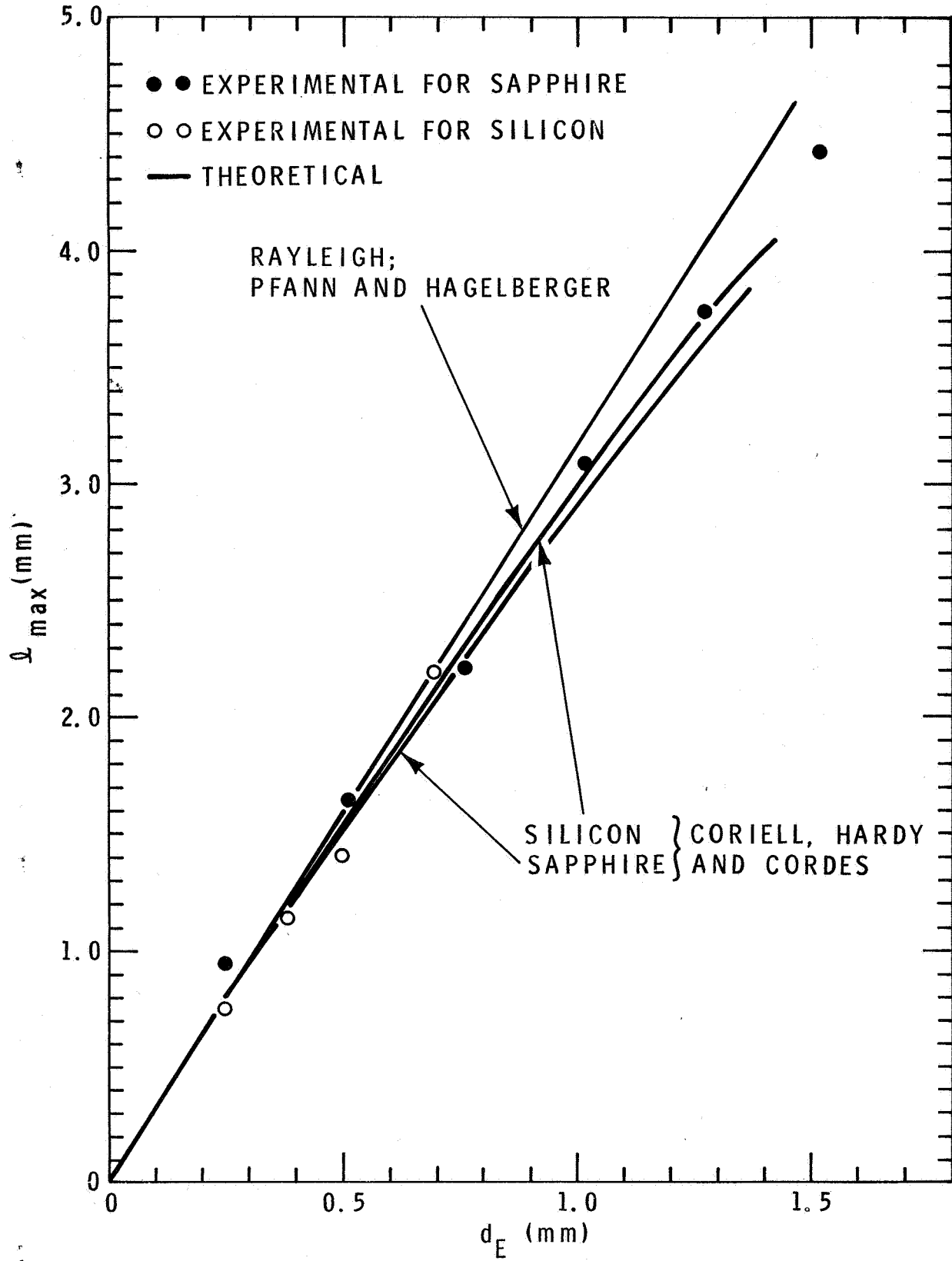
Figure 2. Maximum stable zone length versus diameter.

and the economy of the growth process. Dislocation density of the large diameter crystals is literally zero. In fact, zero-D growth is the necessary condition for growing single crystalline in large diameter crystals of any significant length. This is due to the fact that even a single dislocation in the growing crystal would multiply immediately under the thermal stress present during the large diameter crystals, and this would lead to polycrystalline growth.

Several problem areas which need improvement may be summarized as follows:

1. Uniformity of radial segregation of dopant (for n-type silicon, neutron transmutation doping can be used beneficially to alleviate this problem).

2. Control of microdefects, point defects and low-level impurities, including carbon, oxygen and metals.

3. Automation of the growth process in order to eliminate the high operator dependency in the process and, thus, to improve the economy and reproducibility.

The uniformity of dopant segregation and also the distribution and formation of microdefects should be highly influenced by the fluctuation of the microscopic growth rate due to the fluid flow in the floating zone. Float zone growth of silicon in space may provide some favorable conditions with regard to the first two items. The automation which is already in progress in the semiconductor industry, especially in the Czochralski silicon growth, could be speeded up in the development efforts, if additional support becomes available as a part of the NASA program.

For successful float zone silicon growth in the space lab, it seems to be highly desirable to study first various aspects of the float zone silicon growth. This study should include theoretical modeling, measurement of thermophysical properties of silicon, and well-defined experiments which will delineate some specific aspect of the float zone process. Some suggestions may be summarized as follows:

1. Investigation of thermal convection, capillary-driven flow, and RF-induced flow in case of RF power source which is now used mostly in the semiconductor industry and also might be considered for the space lab application.

2. Critical review of the thermophysical properties of silicon, especially liquid silicon, which include kinematic viscosity, thermal diffusivity, heat capacity, coefficient of volume

expansion, emissivity, and diffusion coefficient of the dopants and impurities. Some of these parameters may have to be remeasured precisely; also, their dependence on the temperature has to be investigated.

3. Influence of the various fluid flows in (1) on the distribution of the dopant, impurities, point defects and microdefects in the crystal because of their perturbation of the microscopic growth rate and/or mass, thermal boundary layer at the growth interface should be investigated precisley. Such correlations have to be made on a one-to-one basis in time, which has been established in some cases; for instance, in the crystal growth in InSb under a destabilizing thermal gradient.

Results of the preceding studies would lead us to an intelligent design and planning of the float zone silicon growth experiment in the space lab.

PROBLEMS WITH STATE-OF-THE-ART FZ SILICON

L. Jastrzebski

Dr. Jastrzebski, RCA Labs, Princeton, represents an industrial user of float zone Si. He discussed an application in which CCD optical imaging arrays with 250,000 elements are being fabricated from the best commercially available float zone Si, boron doped to 10 Ω-cm. Two image defects were described which appear to be related to the starting material. These are shown in Figure 1.

The striation effect appears to be caused by resistivity and recombination center variations. Figure 2 shows up to 30 percent variations in resistivity measured across the sample. Similarly, Figure 3 shows 15 percent or higher variations in density of recombination centers from deep levels. These correlate well with EBIC and DSPS measurements, as may be seen in Figure 4.

Dr. Jastrzebski believes that studies of the relationships between growth kinetics and material properties have been neglected, particularly with regard to the cause and control of deep centers. It was stated that this may be the ultimate material limitation of VSLI technology. In GaAs, deep centers appear to be related to growth rate fluctuations. It was speculated that in Si deep centers may be related to clusters of point defects which, in turn, are somehow related to growth kinetics. Any insight that could be gained in understanding this process would be welcomed by industry.

The following comments were provided by Dr. Jastrzebski after the meeting:

1. Modeling of growth kinetics.

   I have been impressed by the extensive and exhausted effort which has been devoted to calculate the flow pattern in the melt. If surface measurements can be extended to high temperature materials (I do not see any reason why not) it seems that the quantitative hydrodynamic models can be developed which should allow to predict growth kinetics during float zone growth of electronic materials.

   So far the shape of the melt during float zone process has not been taken into account. To what extent will this influence the calculations? I would suggest, at least roughly, to estimate this effect.

2. Missing link.

   Analysis of the relationships between growth kinetics and material properties seems to be completely missing from the present investigations. Even if growth kinetics can be predicted, can we predict material properties?

It is well known which effect growth kinetics would have on distribution of simple impurities. It is not known what is the relationship between growth kinetics and formation on the growing interface of point defects or impurities clusters, e.g. boron oxygen or carbon complexes. Also, our knowledge about the effect which impurity clusters and point defect complexes will have on the electronic characteristics of silicon (this is important for device performance) is practically not existing.

This comment is not a criticism of the NASA program but rather an expression of my concern on emphasis which are placed by the crystal growth community on the research topics.

3. Industrial importance.

It should be proven in the first place that the striation free silicon (no microscopic variations in impurities and deep level concentration) can be grown in space. Striations in CCD imagers (due to microscopic variations in recombination center concentration and resistivity) are one of the major problems affecting performance of these devices. There are different ways to get around this problem (epitaxial layers, different device design, and changes of processing steps) but it seems that the CCD imager technology will benefit first and immediately from the striation free float zone silicon grown in space. Although, to consider any real industrial applications, at least three inch in diameter crystals are required. The CCD imagers can afford the higher cost of silicon wafers because in this circuit cost of silicon wafers is a very small part of the circuit price.

Power devices seem to be the second category of devices which can benefit from striation free silicon. Although in this case the economic aspects will be probably more important in the final considerations. I would suggest to consult people working in the power devices industry to establish if there are any special type of devices which require p type striation free silicon and can bare the high cost of starting material.

VLSI

Silicon with high concentration of oxygen (in the order of $10^{18} cm^{-3}$) is required for the production of ICs. Requirement for material homogeneity for VLSI circuits has not yet been established. It is likely that inhomogeneous distribution of impurities and deep centers in the presently available silicon can lead to unacceptable variations in the threshold voltages of transistors, to large back gate trans-conductance or high 1/f noise level which cannot be tolerated in some high performance VLSI circuits. If striation free silicon can be grown in space one can imagine the possibility of growing float zone silicon with high controllable oxygen concentration which could be used for this high performance circuit.

Conclusions

The part of the program devoted to modeling of hydrodynamics is impressive indeed (I also included here surface measurements). It seems that the research on the relationship between growth kinetics and material properties did not receive enough attention.

It is a real need in the electronic industry for striation-free material, especially for CCD imager technology. At the present time it is unknown if for certain high performance VLSI circuits striation free float zone silicon intentionally doped with oxygen will be required.

It seems to me that the major objective of the present program should be the demonstration that striation-free silicon could be grown in space.

CCD IMAGER DEFECTS OBSERVED ON TV MONITOR
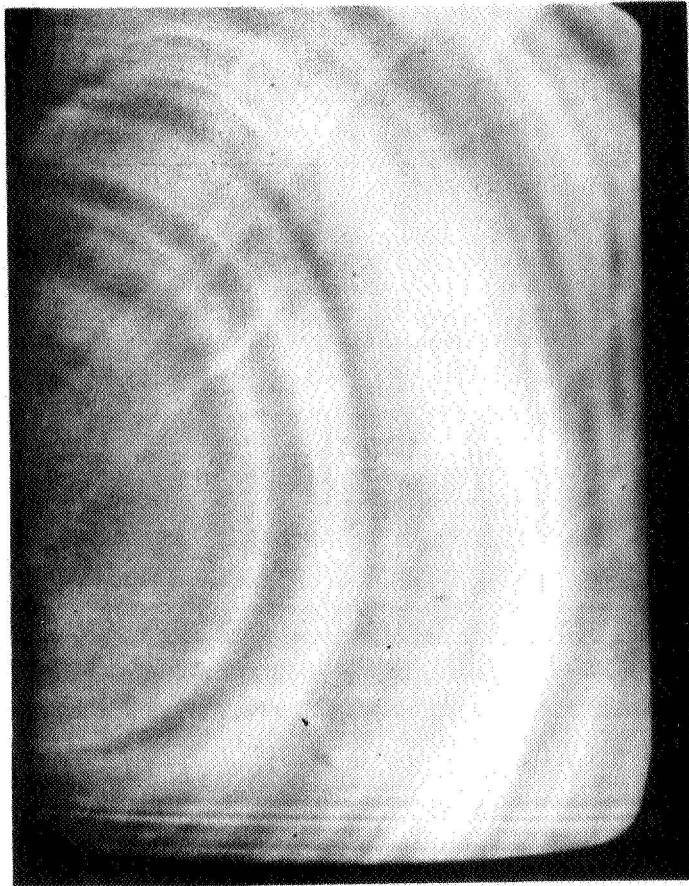
STRIATIONS — RESISTIVITY AND
RECOMBINATION·CENTER VARIATIONS
DUE TO STARTING MATERIAL
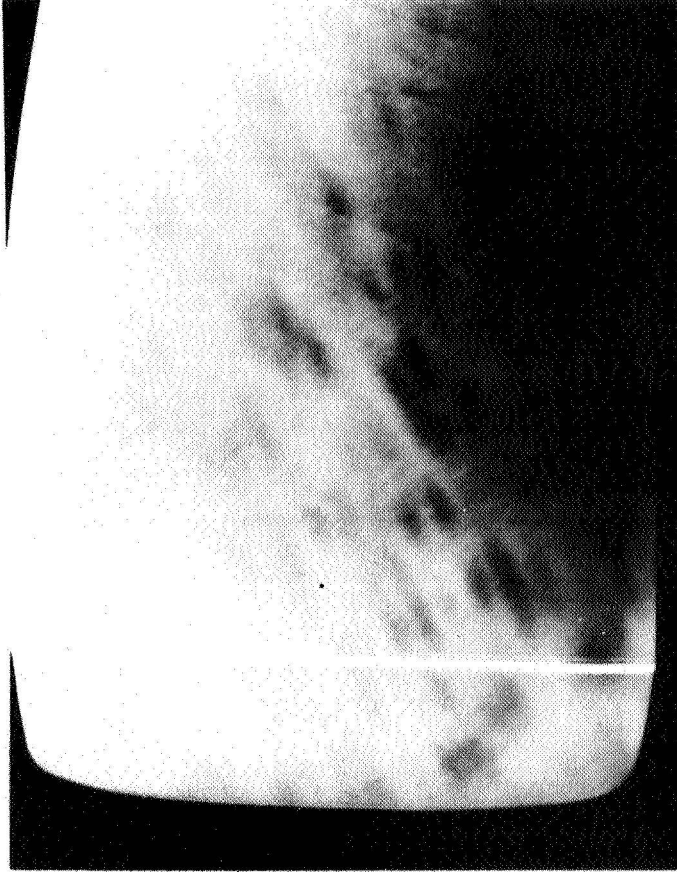
DIRTY-WINDOW EFFECT

DUE TO
POLYSILICON-GATE
GAP CHARGING

Figure 1

89
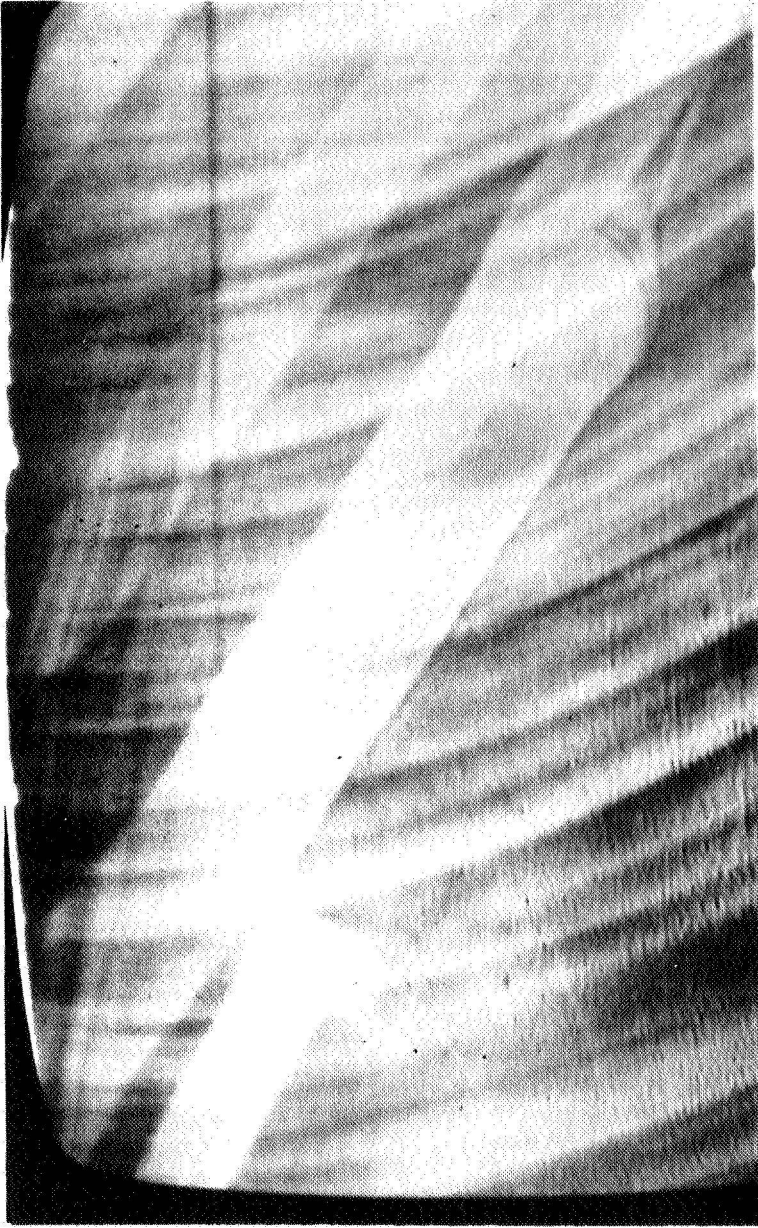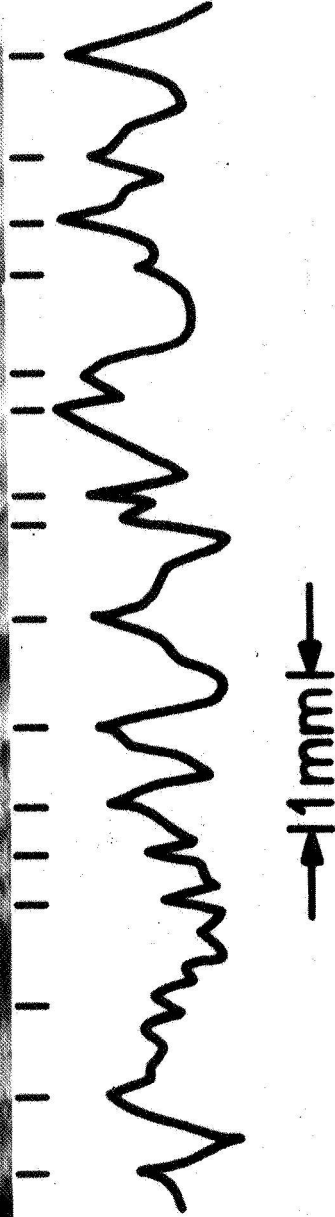
Figure 2. Correlation of resistivity variations with image defects.

90

(a)

(b)

$$\frac{\Delta N_{Rec}}{N_{REC}} \Big| 5\%$$

|1mm|
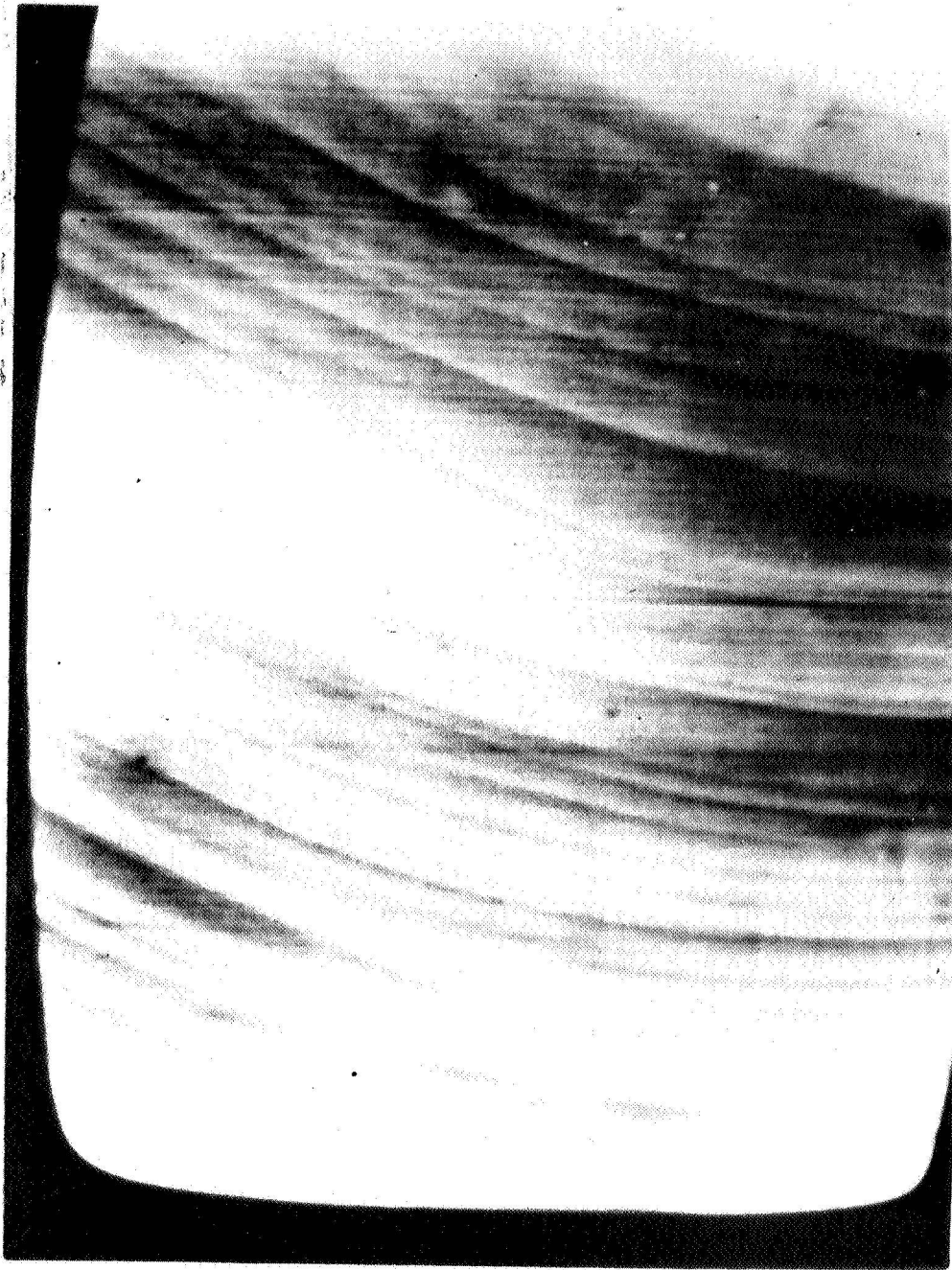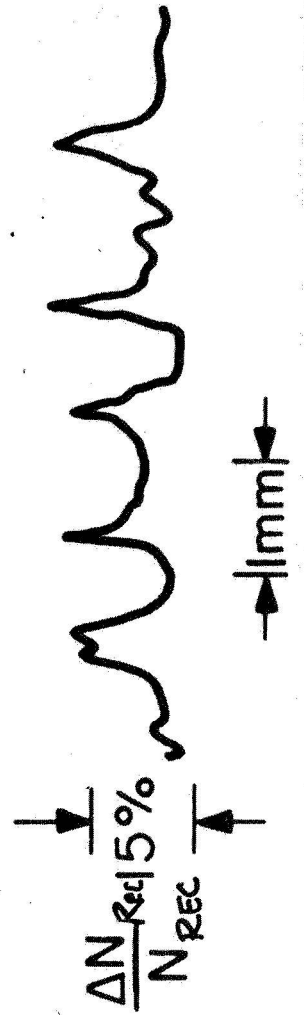
Figure 3. Correlation of variations in recombination centers from deep levels with image defects.

(a)

$\dfrac{\Delta N_{Rec}}{N_{Rec}}$ 15%

(b) EBIC

400 μm

$\dfrac{\Delta N_{Rec}}{N_{Rec}}$ 15%

(c) DSPS

$\dfrac{\Delta N_{Trap}}{N_{Trap}}$ 5%
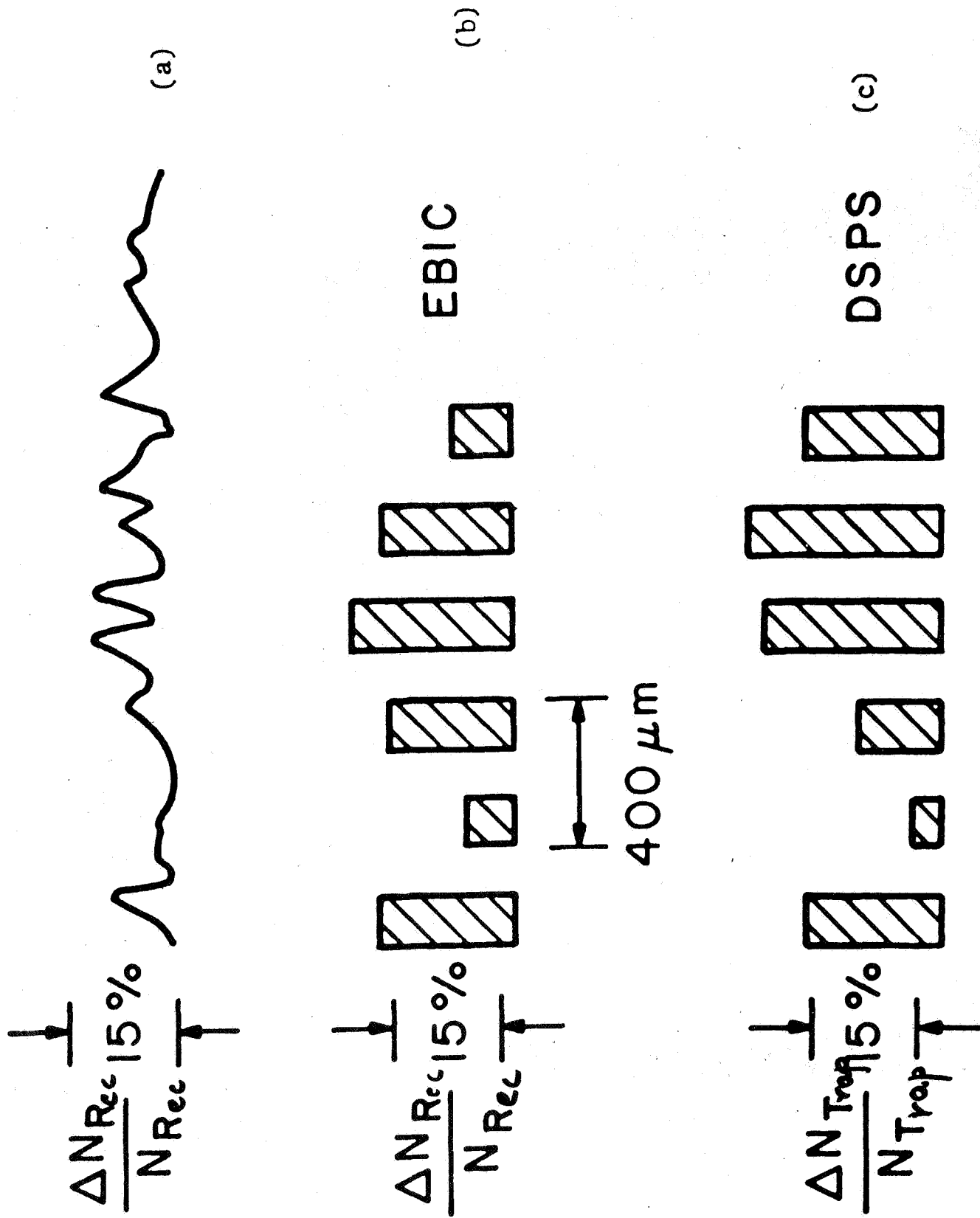
Figure 4. Correlation of recombination centers from deep levels with EBIC in DSPS measurements.

IMPORTANCE OF CONVECTIVE FLOWS IN FLOAT ZONE PROCESSES

W. Wilcox

A few summary comments on the importance of convective flows in the float zone process were offered by Dr. W. Wilcox, Clarkson College of Technology. Dr. Wilcox and one of his graduate students, Dr. Chang, published the first paper calling attention to the large surface tension-driven flows possible in the float zone process of Si, provided the surface remains pure. Dr. Wilcox stated that their original paper contained some mistakes of which they had become aware since its publication but that the general conclusions were still valid. The major issues at present are:

1. Since RF induction heating is utilized in most industrial float zone applications, how much stirring is caused by this heating? Can it be avoided by appropriate changes in coil design or zone configuration? Is surface tension or natural convection significant in such processes?

2. Assuming RF-induced stirring can be avoided (either by appropriate coil design or by use of an alternative heating technique), does the surface of the zone actually move because of surface tension effects for materials of technical importance? Or does the presence of trace impurities or oxide films on the surface prevent such movement?

3. For those materials whose free melt surface does move because of surface tension effects, what sort of measures can be taken to inhibit movement without producing inferior crystals, e.g., due to inclusions of oxide particles?

4. Can the heat source be made sufficiently symmetrical so that crystal and feed rotation will not be required?

5. Can a more efficient heating system be found, or can reflectors be used to reduce the heat loss so that high melting materials can be float zoned in space with modest powers?

IV. SUMMARY

R. J. Naumann

At first impression there seemed to be little correlation between the research presently being sponsored by NASA and the types of problems the industrial community is dealing with. One attendee stated:

> There seems to be a chasm — The Grand Canyon — between the expressed objective and the research being performed. .... The research appears to be aimed at studies of convection and at technologically unimportant materials. In addition, the fluid mechanics work seems to have been directed to totally different geometries from floating zone melting.

Given the facts that present industrial float zone efforts are primarily dedicated to large diameter Si and that they employ RF heating and highly distorted zone shapes, it seems unlikely that surface tension-driven flow is of much concern since the process is probably dominated by RF stirring. Also, it was stated by several presenters that the float zone configurations and procedures are arrived at empirically rather than by careful analysis. Not only are the real geometries very complicated, but it was pointed out by several presenters that our ability to model the process is limited primarily by our lack of knowledge of thermophysical properties. Also, it appeared that the industrial producers had most of their problems under reasonable control, especially those pertaining to seeding and growing large diameters, maintaining requisite purity, and obtaining dislocation-free growth.

The one major deficiency of current technology appears to be the ability to produce uniformly doped material, free of radial segregation, growth rate striations, and microdefects such as clustering of point defects or impurity clusters of B, O, or C complexes. Clearly, uniformly doped Si can be obtained by transmutation doping, but this can only produce P as a dopant and is, therefore, of limited value for device application. It was evident from several presentations that presently available material leaves much to be desired for the fabrication of large focal plane arrays for both visible and near-IR applications. It appears, therefore, that the direction of the NASA program should be toward control of radial segregation and growth rate fluctuations and understanding the mechanism of microdefect production. The subject of Marangoni convection is certainly involved, but the emphasis may be misplaced.

Other major issues need to be considered as well. These are:

1. The major cause of striations in presently available float zone silicon appears to be the growth rate fluctuations induced by the asymmetrical heating from the slot in the RF work coil. Can this be eliminated by inductively coupling into a continuous ring heater, or by other heating methods?

2. What is responsible for the smaller fluctuations that are not attributed to the slotted work coil? Is this some sort of convective instability? Is it gravity dependent? Can it be modeled?

3. What are the relative contributions to stirring of the melt in the zone from the RF heating, natural convection, Marangoni convection? How are melt interface, growth kinetics, and distribution of dopants, impurity, cluster, point defects, and microdefects influenced by these flows? Is there any perceived advantage to having a quiescent melt in which transport is dominated by diffusion?

4. What is the nature of the surface of the molten Si zone? Is the surface subject to Marangoni convection, or is surface flow prevented by oxide layers? Can this be controlled?

It would seem that these issues must be resolved in order to provide the rationale for proceeding with a major space experiment. Some precursory experiments may be necessary to provide the necessary information, but it appears that most of the issues could be addressed by well-planned ground-based investigations.

APPENDIX

PAPERS RELATING TO DR. MANN'S WORK ON RIPPLONS

A. RIPPLON SCATTERING USING GRATING HETERODYNE SPECTROSCOPY

R.S. Sirohi[*], R.V. Edwards and J.A. Mann, Jr.
Case Western Reserve University
Chemical Engineering Department
Cleveland, Ohio 44106

Abstract:

Heterodyne photon spectroscopy is used for the study of the viseo-elastic properties of the liquid interface by studying the scattering from thermal ripplons. A theory of a heterodyne apparatus based on a grating is presented, and the heterodyne condition is given in terms of the parameters of the experimental set-up. Emphasis has been placed to the study of the instrumental function and its influence on the measurement data. It is shown that the instrumental function is not always gaussian, but its functional form depends on the parameters of the experimental set-up. An algorithm is suggested to arrive at the center frequency and half width at half height of the spectrum from the noisy experimental data, and applied to the measurement data obtained from ethanol and water surfaces.

---

* Permanent Address:
  Indian Institute of Technology
  Physics Department
  Madras-600 036 (India)

1. Introduction

The scattering of light from thermally excited capillary waves was first predicted by Smoluchowski[1] and experimentally observed by Mandelshtam[2], and Raman and Ramdas[3]. These surface wave fields can be studied by measuring the statistical properties of light scattered from the fluctuating interface by using either homodyne or heterodyne photon spectroscopy. A review article by Cummins and Swinney[4] contains a detailed analysis of these measurement techniques. Essentially one measures photo-current and processes it either in time or frequency domain. The spectrum of photo-current has been used to measure the properties of the liquid interface[5] and to study monolayers on the surface[6,7].

In many studies using heterodyne spectroscopy, the local oscillator beam was generated by scattering from dust particles in the experimental set up, or from inserting rough optical elements, such as a teflon wedge, partly in the beam, and the angular selectivity was achieved by inserting a pin-hole in front of the detector. Bouchiat et al.[8] was able to achieve sufficient angular resolution by using an incident beam normal to the surface and an annular aperture in front of the detector. The maximum collection efficiency was obtained with minimum effect on the shape of the spectrum. Some of the researchers have used optimal grating for generating local oscillator beam from the diffraction of the reflected beam[6,9,10]. A recent paper by Härd et al.[10] describes the theory and experiments using grating for generating the local oscillator signal. Since the optical properties of grating can be defined and controlled, we believe it to be a superior optical element for obtaining efficient heterodyne operation.

In this paper we develop the theory of the grating heterodyne apparatus by following the propagation of a gaussian beam consistently through the entire optical arrangement. Two different configurations which are equally well suited for heterodyne spectroscopy are analyzed. The influence of finite beam size which leads to instrumental broadening on the spectrum of photo-current has been discussed. An algorithm for computing the center frequency and half width at half height parameters of the Lorentzian spectrum function from the measured spectrum is given and applied to the measured spectra of water and ethanol respectively. Although the basic approach is the same as that of Hård et al.[10], we have given exact expressions for the heterodyne conditions for two separate experimental arrangements. Emphasis is laid on the influence of instrumental function on measurement data. Our analysis shows that the instrumental effects are seriously large in the range of incident angles suggested by them. We also present an algorithm to obtain parameters of interest from noisy data.

The operation of grating heterodyne apparatus is as follows: A beam of light incident at the liquid surface is scattered by thermally excited capillary waves (ripplons). Just above the surface there are specularly reflected and scattered fields; the scattered field is easily detectable in a very narrow angular range about the specularly reflected beam; the scattered irradiance falls as $1/|\sin\theta - \sin\theta_{scatt}|^2$ where the angles are computed from the normal to the surface. The reflected and scattered fields pass through a grating, which is designed for high transmittance. Therefore, the scattered field is assumed to propagate unattenuated, but the specularly reflected beam suffers diffraction. Various orders thus produced

propagate in well defined directions, and a lens brings the diffracted field to focus at its focal plane where one spot is observed for each order. If, for example, the grating is parallel to the liquid surface and is located very near to it, the component of the scattered field from surface ripplons characterized by the same wave vector as that of the grating will propagate in the same direction and will completely superpose on the focal plane, as the focal spots will be of identical sizes. If a photo-detector is placed at the focal plane, photo-mixing takes place. In order to minimize the effect of homo-dyne, the local oscillator beam is stronger by many orders of magnitude than the ripplon scattered field. The method of fabricating gratings of desired diffraction efficiencies is discussed in Section 6.

2. Theory

The field distributions at the detector plane, and consequently the photo-current, depend on the geometric and physical parameters of the experimental set up as well as the statistical properties of the ripplon field on the surface. We have analyzed two configurations (henceforth called A and B); in configuration A, the surface is illuminated by a lightly convergent beam, while in configuration B it is illuminated by a collimated beam. The schematics for both the configurations are shown in Figure 1a and 1b.

The field at $x_1 - y_1$ plane, just before the lens, is expressed by

$$V_-(x_1;y_1;t) = \frac{\sqrt{P_o}}{\sqrt{2\pi\sigma^2}} \cdot e^{-(x_1^2 + y_1^2)/4\sigma^2} \cdot e^{i(\omega t + \phi)}, \tag{1}$$

where P_o is the power in the incident beam, and $1/e^2$ points in irradiance distribution are separated by 4σ. The coordinate systems is centered on the lens. The lens L has an amplitude transmittance $t(x_1,y_1)$ given by

101

$$t(x_1, y_1) = e^{-i\frac{K}{2f}(x_1^2 + y_1^2)} \quad , \tag{2}$$

where f is its focal length and $\vec{K} = (2\pi/\lambda)$ wave vector of the light.

Under Fresnel approximation, the field $V_-(x,y;t)$ at the surface x-y can be expressed as

$$V_-(x,y;t) = -\frac{i\lambda}{R_o} \cdot e^{i KR_o} \cdot e^{i(\omega t + \phi)} \cdot \cos\theta \cdot \sqrt{\frac{P_o}{2\pi\sigma^2}} \cdot e^{\frac{i K}{2R_o}(x^2\cos^2\theta + y^2)}$$

$$\cdot e^{i Kx \sin\theta} \cdot \iint e^{-\frac{(x_1^2 + y_1^2)}{2p_1^2}} \cdot e^{-\frac{iK}{R_o}(x x_1 \cos\theta + y y_1)} dx_1 dy_1 \quad , \tag{3}$$

where

$$\frac{1}{2p_1^2} = \frac{1}{4\sigma^2} + \frac{iK}{2f} - \frac{iK}{2R_o} \quad .$$

At the surface, the beam widths along x and y directions will be different. x-y plane represents the equilibrium liquid surface. The ripplons on the surface are small amplitude (~ 10 Å) decaying waves produced by thermal fluctuations and at any instant of time equal number of ripplons travel in both positive and negative x or y directions. Mode-mode coupling has not been observed and will be ignored. The surface may therefore be characterized by the super-position of travelling waves in the form of

$$g(x,y;t) = \iint a_{K_s}(t) \cos(K_{sx}x + K_{sy}y + \phi_{K_s}) dK_{sx} dK_{sy} \tag{4}$$

where $\vec{K}_s$ is the wave-vector of the surface wave, ϕ_{K_s} the initial phase and $a_{K_s}(t)$ is the amplitude. For the sake of simplicity we assume initially a surface supporting a wave of single $\vec{K}_s$, namely

$$a_{K_s}(t) \cos (K_{sx}x + K_{sy}y + \phi_{K_s})$$

and include the influence of all $\vec{K}_s$'s at a later stage. The field distribution just above the surface, after scattering, can be put in the form of

$$V_+(x,y;t) = V_{+d}(x,y;t) + V_{+s}(x,y;t),$$

where $V_{+d}(x;y;t)$ is the specularly reflected field. If we denote the amplitude reflectance of the surface by $r_\perp(\theta)$, as the field is assumed to be polarized in a plane perpendicular to the plane of incidence (i.e., the electric vector of the field $V_-(x,y;t)$ lies in the surface. But for this statement vector nature of light is not needed). The specularly reflected field V_{+d} is, therefore, given by

$$V_{+d}(x,y;t) = r_\perp(\theta) V_-(x,y;t).$$

The direct field propagates to the grating plane and is diffracted by the grating to form diffraction orders at the focal plane u–v. We characterize the grating by an amplitude transmittance $\tau(x_2,y_2)$ which is given by

$$\tau(x_2,y_2) = b_0 + b_1 \cos (K_0 x_2 + \phi_0), \tag{5}$$

where $\vec{K}_0$ is the grating wave-vector, ϕ_0 its initial phase and b_1 is the modulation. In practice $b_1 \ll b_0$ and $b_0 \simeq 1$. The grating is very weak and hence is nearly transparent. Usually a binary grating, for reasons of ease of fabrication, is used in the experimental set up. It is straightforward to include the binary grating in the analysis. The field distribution at the u–v plane will contain three orders; strong zero-order due to the b_0 term and two ± 1 orders on either side of the zero-order. Since in heterodyne

spectroscopy we use one of the first orders as local oscillator, it is adequate to write expressions for the fields in these orders only. The field distribution $V_d^{-1}(u,v;t)$ in -1 order is

$$V_d^{-1}(u,v;t) = -\frac{i}{\lambda f} \cdot r_\perp(\theta)\, b_1\, \overline{\sqrt{2\pi\sigma^2 P_o}} \cdot e^{iKf} \cdot e^{i(\omega t + \phi - \phi_o)}$$

$$\cdot\, e^{-i\frac{K}{2}\frac{(R_o+L)(R_1-L)}{f}(\frac{K_o}{K})^2} \cdot e^{i\frac{K}{2f}(u^2+v^2)} \cdot e^{-iK\frac{uh}{R_1-L}(\frac{K_o}{K})}$$

$$\cdot\, e^{-\sigma^2\frac{K^2}{f^2}\left[\{u + (R_1-L)\frac{K_o}{K}\}^2 + v^2\right]} \quad , \tag{6}$$

and the field distribution $V_d^{+1}(u,v;t)$ in $+1$ order is

$$V_d^{+1}(u,v;t) = -\frac{i}{\lambda f} \cdot r_\perp(\theta)\, b_1\, \overline{\sqrt{2\pi\sigma^2 P_o}} \quad e^{iKf} \quad e^{i(\omega t + \phi + \phi_o)}$$

$$\cdot\, e^{-i\frac{K}{2}\frac{(R_o+L)(R_1-L)}{f}(\frac{K_o}{K})^2} \cdot e^{i\frac{K}{2f}(u^2+v^2)} \cdot e^{iK\frac{uh}{R_1-L}(\frac{K_o}{K})}$$

$$\cdot\, e^{-\sigma^2\frac{K^2}{f^2}\left[\{u - (R_1-L)\frac{K_o}{K}\}^2 + v^2\right]} \quad , \tag{7}$$

where

$$h = \frac{(R_o+L)(R_1-L)}{f} \quad .$$

While evaluating the integrals leading to these expressions, it is assumed that the grating and the lens are large compared to the beam size. The integrals are, therefore, evaluated between infinite limits. These expressions show that the spots have gaussian distributions and are centered at

$u = \pm(R_1-L)\frac{K_o}{K}$ and $v = 0$. The $1/e^2$ points are separated by $2f/\sigma K$. It can be shown that the total power in each of the spots is $r_\perp^2(\frac{b_1}{2})^2 P_o$.

The scattered field $V_{+s}(x,y;t)$ propagates through the grating, almost unattenuated, to the focal-plane. We can express the field at u-v plane

104

using Born's approximation, i.e.,:

$$V_{SK}(u,v;t) = b_o \, a_{K_s}(t) \, \frac{4\pi}{\lambda^2} \frac{(n^2-1)\cos^2\theta}{[(n^2-\sin^2\theta)^{1/2}+\cos\theta]^2} \iint V_-(x,y;t) \, \frac{e^{i\,Kr}}{r} \cdot$$

$$\cos(K_{sx}x + K_{sy}y + \phi_{K_s}) \, dx \, dy \,, \tag{8}$$

where n is the refractive index of the bulk liquid.

The distance r can be expressed, under Fresnel approximation, by

$$r = R_1 - x \sin\theta + \frac{(x^2\cos^2\theta + y^2)}{2R_1} + \frac{(u^2+v^2)}{2R_1} + \frac{x\,u\cos\theta + yv}{R_1} \,.$$

The parameter b_o is the d.c. transmittance of the grating. This integral can be evaluated to give

$$V_{SK}(u,v;t) = C \, e^{\frac{iK}{2f}(u^2+v^2)} \cdot e^{-i\frac{K}{2}\frac{R_o R_1}{f}\left(\left(\frac{K_{sx}}{K\cos\theta}\right)^2 + \left(\frac{K_{sy}}{K}\right)^2\right)} [e^{-i\phi_{K_s}} \cdot$$

$$e^{iK\frac{R_o}{f}\{u\frac{K_{sx}}{K\cos\theta} + v\frac{K_{sy}}{K}\}} \cdot e^{-\frac{\sigma^2 K^2}{f^2}\left[(u - \frac{R_1 K_{sx}}{\cos\theta \, K})^2 + (v - R_1\frac{K_{sy}}{K})^2\right]} + e^{i\phi_{K_s}} \cdot$$

$$e^{-iK\frac{R_o}{f}\{u\frac{K_{sx}}{K\cos} + v\frac{K_{sy}}{K}\}} \cdot e^{-\frac{\sigma^2 K^2}{f^2}\left[(u + \frac{R_1}{\cos\theta}\frac{K_{sx}}{K})^2 + (v + R_1\frac{K_{sy}}{K})^2\right]}], \tag{9}$$

where the constant C is defined as

$$C = \frac{4\pi}{\lambda 2} \frac{\sqrt{2\pi\sigma^2 P_o}}{f} b_o \, a_{K_s}(t) \, \frac{(n^2 - 1)\cos^2\theta}{[(n^2-\sin^2\theta)^{1/2} + \cos\theta]^2} \cdot e^{iK(R_o + R_1)} \cdot e^{i(\omega t + \phi)} \,.$$

The first and second terms in the square bracket are respectively − 1 and +1 diffraction orders of the surface wave. From the geometry of the set up, it can be seen that the −1 order will propagate in the direction of +1 order of the grating or vice versa. The physical extents of the diffraction spots are about the same. It is interesting to note that the spatial distribution of the scattered

105

field under Born's approximation remains essentially gaussian. The power in each diffraction spot of the field scattered from the surface is

$$\frac{4\pi^2}{\lambda^2} P_o b_o^2 |a_{K_s}(t)|^2 \frac{(n^2 - 1)^2 \cos^4\theta}{[(n^2 - \sin^2\theta)^{1/2} + \cos\theta]^4} .$$

The power is independent of focal length of the lens, and depends on the physical properties of the liquid, angle of incidence, and the wavelength of light used.

Photo-current calculations:

The photo-current i(t) due to the two fields propagating in the same direction and incident on the photo-cathode is proportional to the total irradiance and can be expressed by

$$\frac{\eta_c e}{h\nu} \int |V_d^{+1} + V_{SK}^{-1}|^2 \, dudv,$$

where η_c is the quantum efficiency of the photocathode, e is the electronic charge and $h\nu$ is the energy of a photon of frequency ν. The integration is carried on the surface of the photo-cathode. V_d^{+1} is the field distribution in +1 order from grating and V_{SK}^{-1} is the field distribution in the -1 order from surface waves. In practice $V_d^{+1} \ggg V_{SK}^{-1}$, so that there is no appreciable homodyne contribution. The photo-current has a very strong d.c. part and an a.c. part which we call signal. The expected value of photo-current (signal) is given by

$$<i_{K_s}> = \frac{\eta_c e}{h\nu} \int < V_d^{+1}V_{SK}^{-1*} + V_d^{+1*}V_{SK}^{-1}> \, dudv. \tag{10}$$

After substituting the expressions for the fields, the expected value of the photo-current is found to be

$$\langle i_{K_s}(t)\rangle = \frac{16\pi^2}{hc}\eta_c e\left(\frac{-i}{\lambda^2 f^2}\right) r_\perp(0)\, b_0 b_1 P_0\, \sigma^2\, \langle a_{K_s}(t)\rangle\, \frac{(n^2-1)\cos^2\theta}{[(n^2-\sin^2\theta)^{1/2}+\cos\theta]^2}\cdot$$

$$\iint e^{-\frac{\sigma^2 K^2}{f^2}\left[(u-\frac{R_1}{\cos\theta}\frac{K_{sx}}{K})^2 + (v-\frac{R_1}{K}K_{sy})^2 + \{u-(R_1-L)\frac{K_0}{K}\}^2 + v^2\right]}\cdot \cos(\phi_0+\phi_{K_s}+\phi')\,dudv, \tag{11}$$

where

$$\phi' = \phi_1+\phi_K = \phi_1 + K\,u\left[\frac{K_0}{K}\frac{R_0+L}{f} - \frac{R_0}{f}\frac{K_{sx}}{K\cos\theta}\right] - K\,v\,\frac{R_0}{f}\left(\frac{K_{sy}}{K}\right), \text{ and}$$

$$\phi_1 = -\frac{K}{2}\frac{(R_0+L)(R_1-L)}{f}\left(\frac{K_0}{K}\right)^2 + \frac{K}{2}\frac{R_0 R_1}{f}\left[\left(\frac{K_{sx}}{K\cos\theta}\right)^2 + \left(\frac{K_{sy}}{K}\right)^2\right].$$

The phase ϕ_K is dependent on u and v coordinates. The cos term appearing in the integral is expressed by

$$\cos(\phi_0+\phi_{K_s}+\phi_1+\phi_K+\tfrac{\pi}{2}) = \frac{1}{2}\left[\, e^{i(\phi_0+\phi_{K_s}+\phi_1+\frac{\pi}{2})}\, e^{i\phi_K} + e^{-i(\phi_0+\phi_{K_s}+\phi_1+\frac{\pi}{2})}\, e^{-i\phi_K}\right]$$

and the integral is then evaluated.* After little manipulation, the expected value of photo-current is found to be

$$\langle i_{K_s}(t)\rangle = \frac{2\pi\eta_c e}{hc}\, r_\perp(0)\, b_0 b_1 P_0\, \langle a_{K_s}(t)\rangle\, \frac{(n^2-1)\cos^2\theta}{[(n^2-\sin^2\theta)^{1/2}+\cos\theta]^2}$$

$$e^{-K_0^2\frac{\sigma^2}{2}\frac{f^2 L^2}{(4\sigma^4 K^2 R_1^2 + R_0^2 f^2)}}\cdot e^{-\frac{4\sigma^4 K^2 R_1^2 + R_0^2 f^2}{8\sigma^2 K^2 f^2}\left[(K_0\frac{4\sigma^4 K^2 R_1(R_1-L)+R_0(R_0+L)f^2}{4\sigma^4 K^2 R_1^2 + R_0^2 f^2} - \frac{K_{sx}}{\cos\theta})^2}$$

$$+ K_{sy}^2\right] \tag{12}$$

$$\cdot\cos\Phi_1 ,$$

where $\Phi_1 = \phi_0 + \phi_{K_s} + \phi_1 + \psi + \pi/2$, and

$$\psi = K\left[\left(\frac{K_0}{K}\frac{R_0+L}{f} - \frac{R_0}{f}\frac{K_{sx}}{K\cos\theta}\right)\left(\frac{R_1}{2}\frac{K_{sx}}{K\cos\theta} + \frac{R_1-L}{2}\frac{K_0}{K}\right) - \frac{R_1}{2}\frac{R_0}{f}\left(\frac{K_{sy}}{K}\right)^2\right].$$

The maximum value of $\langle i_{K_s}(t)\rangle$ occurs when

$$K_0\frac{4\sigma^4 K^2 R_1(R_1-L) + R_0(R_0+L)f^2}{4\sigma^4 K^2 R_1^2 + R_0^2 f^2} = \frac{K_{sx}}{\cos\theta}, \text{ and } K_{sy} = 0. \tag{13}$$

---

*The $\pi/2$ term is due to $(-i)$ factor in the constant.

107

In practice $4K^2\sigma^4R_1^2 >> R_o^2f^2$, which means that the lens is kept close to the

surface ($R_1 \simeq f$), the above condition becomes

$$K_o \frac{R_1-L}{R_1} = \frac{K_{sx}}{\cos\theta} \ . \tag{14}$$

If the grating is kept very close to the liquid surface ($L \simeq 0$) then

$K_o = \dfrac{K_{sx}}{\cos\theta}$, a conclusion which can be obtained from elementary considerations.

Under the assumption $4K^2\sigma^4R_1^2 >> R_o^2f^2$, the photo-current $<i_{K_s}(t)>$ is

given by

$$<i_{K_s}(t) = \frac{2\pi\eta_c e}{hc} \ r_\perp(\theta) \ b_o b_1 P_o \ <a_{K_s}(t)> \frac{(n^2-1)\cos^2\theta}{[(n^2-\sin^2\theta)^{1/2}+\cos\theta]^2} \ .$$

$$\cdot \ e^{-L^2/2L_{ol}^2} \cdot e^{-\frac{\sigma'^2}{2}[(K_o\frac{R_1-L}{R_1} - \frac{K_{sx}}{\cos\theta})^2 + K_{sy}^2]} \cdot \cos\Phi_1, \tag{15}$$

where

$$L^2_{ol} = 4(\frac{K}{K_o})^2 (\frac{R_1}{f})^2 \sigma^2, \text{ and } \sigma'^2 = \sigma^2(\frac{R_1}{f})^2.$$

The term $e^{-L^2/2L^2_{ol}}$ leads to attenuation of the signal. Its influence can

be lessened by increasing the magnitude of L_{ol}. An examination of the expression

for L^2_{ol} leads to the conclusion that larger value of σ and a coarse grating

would relax the condition of keeping the grating close to the surface. However

this is achieved at the price of impairing the spatial resolution.

Before proceeding to the processing of photo-current, it is appropriate

at this juncture to write the expression for the expected value of photo-current

for configuration B. Unlike in configuration A, the initial field distribution

is taken at any arbitrary plane distant R_o from the surface. The surface

is illuminated by the collimated beam, and the grating is located a distance L

from the surface. Following the procedure adopted for configuration A, the

expected value of photo current is given by

$$\langle i_{K_s}(t) \rangle = \frac{16\pi^2 \eta_c e}{hc} \cdot \frac{(-i)}{\lambda^2 f^2} \cdot r_\perp(\theta) \, b_o b_1 P_o \cdot \sigma^2 \, \langle a_{K_s}(t) \rangle \frac{(n^2-1)\cos^2\theta}{[(n^2-\sin^2\theta)^{1/2}+\cos\theta]^2}$$

$$\iint e^{-\frac{\sigma^2 K^2}{f^2}[(u-f\frac{K_{sx}}{K\cos\theta})^2 + (v-f\frac{K_{sy}}{K})^2 + (u-\frac{R_o+L}{R_o+R_1}\cdot f \cdot \frac{K_o}{K})^2 + v^2]} \cos(\phi_o+\phi_{K_s}+\phi_B')\, du\, dv \qquad (16)$$

where

$$\phi_B' = \phi_B + Ku[\frac{K_o}{K}\frac{R_o+L}{f} - \frac{K_{sx}}{K\cos\theta}\cdot\frac{R_o}{f}] - Kv\frac{R_o}{f}\frac{K_{sy}}{K} = \phi_B + \phi_{BK}, \text{ and}$$

$$\phi_B = -\frac{K}{2}[(R_o+L)(\frac{K_o}{K})^2 - R_o\{(\frac{K_{sx}}{K\cos\theta})^2 + (\frac{K_{sy}}{K})^2\}].$$

The phase ϕ_{BK} is dependent on u,v coordinates. Expressing cos function in exponential form, the integral is easily evaluated to give

$$\langle i_{K_s}(t) \rangle = \frac{2\pi\eta_c e}{hc}\cdot r_\perp(\theta)\, b_o b_1 P_o \, \langle a_{K_s}(t) \rangle \frac{(n^2-1)\cos^2\theta}{[(n^2-\sin^2\theta)^{1/2}+\cos\theta]^2} \cdot e^{-K_o^2\frac{\sigma^2}{2}(\frac{R_o+L}{R_o+R_1})^2\frac{R_1^2}{4\sigma^4K^2+R_o}}$$

$$e^{-\frac{4\sigma^4K^2+R_o^2}{8\sigma^2K^2}[(K_o\frac{R_o+L}{R_o+R_1}\frac{4\sigma^4K^2+R_o(R_o+R_1)}{4\sigma^4K^2+R_o^2} - \frac{K_{sx}}{\cos\theta})^2 + K_{sy}^2]} \cos\Phi_2, \qquad (17)$$

where $\Phi_2 = \phi_o + \phi_{K_s} + \phi_B + \Psi_B + \frac{\pi}{2}$, and

$$\Psi_B = K[(\frac{K_o}{K}\frac{R_o+L}{R_o+R_1}\cdot\frac{f}{2} + \frac{K_{sx}}{K\cos\theta}\cdot\frac{f}{2})(\frac{R_o+L}{f}\cdot\frac{K_o}{K} - \frac{R_o}{f}\cdot\frac{K_{sx}}{K\cos\theta}) - \frac{R_o}{2}(\frac{K_{sy}}{K})^2].$$

The maximum of $\langle i_{K_s}(t) \rangle$ occurs when

$$K_o\frac{R_o+L}{R_o+R_1}\cdot\frac{4\sigma^4K^2+R_o(R_o+R_1)}{4\sigma^4K^2+R_o^2} = \frac{K_{sx}}{\cos\theta}, \text{ and } K_{sy} = 0. \qquad (18)$$

If we assume that $4\sigma^4K^2 \gg R_o^2$ or $R_o(R_o+R_1)$, the above condition reduces to

$$K_o\frac{R_o+L}{R_o+R_1} = \frac{K_{sx}}{\cos\theta}. \qquad (19)$$

This relation has an arbitrariness due to R_o, which is the distance of any chosen plane from the liquid surface. This arbitrariness disappears when $L = R_1$, i.e., the grating and the lens are coincident. Then the condition (19) simplifies to

$$K_o = \frac{K_{sx}}{\cos\theta}. \qquad (20)$$

109

Under this situation, the expected value of photo-current is given by

$$\langle i_{K_s}(t)\rangle = \frac{2\pi\eta_c e}{hc}\cdot r_\perp(0)\ b_o b_1 P_o\ \langle a_{K_s}(t)\rangle\frac{(n^2-1)\ \cos^2 0}{[(n^2-\sin^2 0)^{1/2}+\cos 0]^2}\cdot e^{-L^2/2L_{o2}^2}\cdot$$

$$e^{-\frac{\sigma^2}{2}\ [(K_o-\frac{K_{sx}}{\cos\theta})^2 + K_{sy}^2]}\cdot\cos\phi_2, \qquad (21)$$

where

$$L_{o2}^2 = 4\ (\frac{K}{K_o})^2\sigma^2\ .$$

Comparison of photo-current expressions for configurations A and B shows that they are similar. However, there are following two noticeable differences:

a) The heterodyne condition does not require the knowledge of L for configuration B.

b) The value of L_o is geometry independent for configuration B.

3. Calculation of Photo-Current Auto-Correlation Function

The expected value of photo-current $\langle i_T(t)\rangle$ for configuration A and B, when the laser beam is scattered from the surface characterized by $g(x,y;t)$, can be written in an abbreviated form as:

$$\langle i_T(t)\rangle = \int \langle a_{K_s}(t)\ F\ (K_o' - K_{sx}, K_{sy})\ \cos\phi_i\rangle\ dK_{sx}\ dK_{sy}\ , \qquad (22)$$

where

$$F(K_{oi}' - K_{sx}, K_{sy}) = Q\ e^{-L^2/2L_{oi}^2}\cdot e^{-\frac{\sigma_i^2}{2}\ [(K_{oi}' - K_{sx})^2 + K_{sy}^2\cos^2\theta]},$$

and

$$Q = \frac{2\pi\eta_c e}{hc}\cdot r_\perp(\theta)\ b_o b_1 P_o\ \frac{(n^2-1)\ \cos^2\theta}{[(n^2-\sin^2\theta)^{1/2}+\cos\theta]^2}\ .$$

The subscript i takes values 1 or 2 for configurations A and B respectively. The parameters σ_i and K_{oi}' are defined as

110

$$\sigma_1^2 = \frac{\sigma'^2}{\cos^2\theta} \quad ; \quad K'_{oi} = K_o \frac{(R_1-L)}{R_1} \cos\theta \quad \text{for configuration A, and}$$

$$\sigma_2^2 = \frac{\sigma^2}{\cos^2\theta} \quad ; \quad K'_{o2} = K_o \cos\theta \quad \text{for configuration B.}$$

The autocorrelation function $R_1(K'_{oi};\tau)$ of the photo-current is expressed as

$$R_I(K'_{oi};\tau) = \quad <i_T(t)\, i_T(t+\tau)>$$

$$= \iint <a_{K_s}(t)\, a_{K_s'}(t+\tau) \cos\Phi_i(t) \cos\Phi_i(t+\tau)> F(K'_{oi} - K_{sx},K_{sy}) \cdot$$

$$F(K'_{oi} - K'_{sx},K'_{xy}) \, d\vec{K}_s \, d\vec{K}_s' \quad . \tag{23}$$

If we assume that

a) the phase Φ_i is statistically independent of the amplitude $a_{K_s}(t)$ and is uniformly distributed between 0 and 2π, and

b) the scattering at $\vec{K}_s$ is statistically independent of scattering at any other $\vec{K}_s$ vector, say $\vec{K}_s'$, we can show that (see Appendix):

$$<a_{K_s}(t)\, a_{K_s'}(t+\tau) \cos\Phi_i(t) \cos\Phi_i(t+\tau)> = \frac{1}{2} <a_{K_s}(t)\, a_{K_s'}(t+\tau)> \, \delta(\vec{K}_s - \vec{K}_s').$$

Therefore the photo-current autocorrelation function $R_1(K'_{oi};\tau)$ is now expressed as

$$R_I(K'_{oi};\tau) = \frac{1}{2} \iint <a_{K_s}(t)\, a_{K_s}(t+\tau)> \, F^2(K'_{oi} - K_{sx},K_{sy}) \, dK_{sx} \, dK_{sy} \quad . \tag{24}$$

4. Instrumental Broadening

It is obvious that the beam size has a profound influence on the autocorrelation function and consequently on the spectrum of the photo-current. Usually a correction for the instrumental function is applied to

111

the observed spectrum. A simple relationship between the half widths of the observed spectrum, and the expected Lorentzian spectrum is given in terms of instrumental width for the case of a gaussian instrumental function by Härd et al.[10]. The instrumental function can be far from gaussian depending on the experimental configuration. Further an upward shift in the mean frequency of ripplons was observed when the ethanol surface was illuminated with a narrow beam at large angles of incidence. In order to understand these observations and to clear the confusion existing in the literature from the point of view of an experimentalist, the study of instrumental broadening was undertaken.

The power spectrum of the photo-current is obtained by taking the Fourier transform of its autocorrelation function. It is given by

$$S(K_{oi}';\omega) = \frac{1}{2} \int F^2(K_{oi}' - K_{sx}, K_{xy}) \, A(\vec{K}_s;\omega) \, dK_{sx} \, dK_{xy}, \tag{25}$$

where $A(\vec{K}_s;\omega)$ is the power spectrum of $<a_{K_s}(t) \, a_{K_s}(t+\tau)>$, i.e.,

$$A(\vec{K}_s;\omega) = \int < a_{K_s}(t) \, a_{K_s}(t+\tau)> \, e^{-i\omega\tau} \, d\tau \quad . \tag{26}$$

The spectrum $A(\vec{K}_s,\omega)$ can be characterized by two parameters: 1) a center frequency parameter ω_{K_s} and 2) the width parameter Γ_1. The latter parameter may be a function of ω_{K_s}. The center frequency parameter contains the dependence on the scattering vector $\vec{K}_s$. At any particular $\vec{K}_s$, ω_{K_s} and Γ_1 are determined by the physical properties of the scattering material. $A(\vec{K}_s;\omega)$ can be written as

$$A(\vec{K}_s;\omega) = \int A(\omega,\omega',\Gamma_1(\omega')) \, \delta(\omega' - \omega_{K_s}) \, d\omega' \quad . \tag{27}$$

112

Substituting eq. (27) into eq. (25) and inverting the order of integration we get

$$S(K'_{oi};\omega) = \frac{1}{2} \int d\omega' \, A(\omega,\omega',\Gamma_1(\omega')) \int_{-\infty}^{\infty} F^2(K'_{oi} - K_{sx}, K_{sy}) \, \delta(\omega' - \omega_{K_s}) \, dK_{sx} \, dK_{sy} \quad . \quad (28)$$

The inner integral yields a function of K'_{oi}, ω', σ_x and Γ_1, and can be denoted the Instrumental function, $S_I(K'_{oi};\omega)$.

$$S_I(K'_{oi};\omega) = \frac{1}{2} \int_{-\infty}^{\infty} F^2(K'_{oi} - K_{sx}, K_{sy}) \, \delta(\omega' - \omega_{K_s}) \, dK_{sx} \, dK_{sy} \quad . \quad (29)$$

The function $S_I(K'_{oi};\omega)$ contains the influence of the optical parameters on the measurement outcome. Once it is computed, the expected output for any function $A(\vec{K}_s;\omega)$ can be computed. This format can also be used for auto-correlation functions.

If we consider scattering from ripplons, then the dispersion equation

$$\omega_{K_s} = \left(\frac{\gamma}{\rho} Y_1 \right)^{1/2} |\vec{K}_s^{3/2}| = \beta |\vec{K}_s^{3/2}| \quad (30a)$$

relates the center frequency ω_{K_s} and wave vector $\vec{K}_s$ of the ripplons. The parameters γ and ρ are the surface tension and density of the liquid and Y_1 is a dimensionless group whose value lies between 0.95 and 1.05 and can be calculated exactly[11].

After substituting for F^2, we obtain

$$S_I(K'_{oi};\omega) = \frac{1}{2} Q_i^2 \iint e^{-\sigma_x^2(K'_{oi}-K_{sx})^2} \cdot e^{-\sigma_y^2 K_{sy}^2} \cdot \delta(\omega - \beta(K_{sx}^2 + K_{sy}^2)^{3/4}) \, dK_{sx} \, dK_{sy} \quad . \quad (30b)$$

where $Q_i = Q \, e^{-L^2/2L_{oi}^2}$, and $\sigma_x^2 = \sigma'^2/\cos^2\theta$; $\sigma_y^2 = \sigma'^2 = \sigma_x^2 \cos^2\theta$ for configuration A.

Let $y = \beta(K_{sx}^2 + K_{sy}^2)^{3/4}$: $y \geq 0$. So,

$$K_{sy} = [\,(\tfrac{y}{\beta})^{4/3} - K_{sx}]^{1/2} \quad : (\tfrac{y}{\beta})^{2/3} \geq K_{sx} .$$

After carrying out integration over K_{sy}, we obtain

$$S_I(K'_{oi};\omega) = \frac{1}{3} Q_i^2 \frac{\omega^{1/3}}{\beta^{4/3}} \int_{-(\omega/\beta)^{2/3}}^{(\omega/\beta)^{2/3}} \frac{e^{-\sigma_x^2(K'_{oi}-K_{sx})^2} \cdot e^{-\sigma_y^2[(\omega/\beta)^{4/3}-K_{sx}^2]}}{[(\omega/\beta)^{4/3} - K_{sx}^2]^{1/2}} \, dK_{sx}. \quad (31)$$

By change of variable this equation can be put in a form more suitable

for numerical computation:

$$S_I(K'_{oi};\tilde\omega) = \frac{1}{3} Q_i^2 \frac{\omega_{oi}^{1/3}}{\beta^{4/3}} \tilde\omega^{1/3} \int_{-\frac{\pi}{2}}^{\frac{\pi}{2}} e^{-q^2[(1-\sin\bar\phi\,\tilde\omega^{2/3})^2 + \Gamma^2\cos^2\bar\phi\,\tilde\omega^{4/3}]} \, d\bar\phi , \quad (32)$$

where $\tilde\omega = \dfrac{\omega}{\omega_{oi}}$; $\Gamma^2 = \sigma_y^2/\sigma_x^2 = \cos^2\theta$, $q = \sigma_x K'_{oi}$ and $\omega_{oi} = \beta K'^{3/2}_{oi}$.

The parameter q is a measure of the number of oscillations of the grating

projected onto the surface.

It is indeed possible to obtain a series solution of this integral.

However, in the present form it is tractable numerically. This integral

is evaluated for a set of values of q and θ. The distribution $S_I(K'_{oi};\tilde\omega)$

departs from gaussian form. It is found that for larger values of $q(\geq 25)$,

$S_I(K_{oi}';\tilde\omega)$ can be represented by a gaussian function excellently. For

medium values of $q(3<q<10)$ the gaussian fit is modest. Nevertheless, it is

a description of the spectrum with which an experimentalist is quite familiar.

The mean frequency $\tilde\omega_m$ and the width parameter $\tilde\sigma_I(\sigma_I/\omega_{oi})$ as a function of q

for a set of values of θ are plotted in Figure 2. There is an increase in

the mean frequency with decrease of q for all values of θ. The increase is

rapid with larger angle of incidence. A point to bear in mind is that a

114

larger value of q is desired to minimize this influence. A value of $q(\geq 20)$ may be satisfactory for measurements up to an incident angle of 60°. From the point of optimum signal to noise ratio, Härd et al.[10] arrived at a best value of θ around 70°. Unfortunately in this range of angles, the instrumental function departs considerably from gaussian particularly for small values of q, and the increase in the mean frequency is noticeably larger.

An exact analytical form of the instrumental function does exist in the form of an infinite series involving Bessel functions of increasing orders. This series converges rather slowly. The exact form of $S_I(K_{oi}';\tilde{\omega})$ is given by

$$S_I(K_{oi}';\tilde{\omega})= \frac{\pi}{3}Q_i^2\,\tilde{\omega}^{1/3}\,\frac{\omega_{oi}^{1/3}}{\beta^{4/3}}\cdot e^{-q^2(1-\tilde{\omega}^{2/3})^2}\cdot e^{-2q^2\tilde{\omega}^{2/3}}\sum_{n=0}^{\infty}\frac{(2n-1)\text{---}3.1}{n!\,2^n}(\tilde{\omega}^{2/3}\sin^2\theta)^n I_n(2q^2\tilde{\omega}^{2/3}).$$

(3

where $I_n(z)$ is modified Bessel function of order n.

For large values of q and smaller values of θ, the instrumental function is well represented by a gaussian function. This limiting form can be represented as

$$S_I(K_{oi}';\omega) = \frac{\pi}{3}\,Q_i^2\,\frac{\omega_{oi}^{1/3}}{\beta^{4/3}}\cdot e^{-\frac{4}{9}q^2(1-\tilde{\omega})^2}$$

(34)

We shall now incorporate the influence of instrumental width on the natural broadening. We assume for simplicity that the function $A(\vec{K}_s;\omega)$, when the light is scattered from the surface of a real fluid, is given by

$$A(K_s;\omega) = A\,\frac{\Gamma_1}{\Gamma_1^2 + (\omega-\omega')^2}\quad,$$

(35)

115

where Γ_1' $(=2\nu K_s^2)$ is the half width at half height and ω' is the Lorentzian frequency corresponding to the wave vector $\vec{K}_s$. It is trivial to extend this to more accurate representations of the spectrum[12]. This expression can be written in dimensionless form as

$$A(K_s;\hat{\omega}) = A\,\frac{\xi\tilde{\omega}^{4/3}}{\xi^2\tilde{\omega}^{8/3} + (\hat{\omega}-\tilde{\omega})^2}\,, \tag{36}$$

where $\hat{\omega} = \dfrac{\omega}{\omega_{oi}}$ and $\tilde{\omega} = \dfrac{\omega'}{\omega_{oi}}$, and the dimensionless width $\xi = \dfrac{2\nu K_{oi}'^2}{\omega_{oi}}$.

On substituting $A(K_s;\omega)$ in eq. (28) and doing algebraic manipulation, the power spectrum $S(K_{oi}';\hat{\omega})$ of the light scattered from the liquid surface can be expressed as

$$S(K_{oi}';\hat{\omega}) = \frac{1}{3}Q_i^2\,A\,\frac{\omega_{oi}^{1/3}}{\beta^{4/3}}\int_{\infty}^{\infty}\frac{\xi\tilde{\omega}^{5/3}}{\xi^2\tilde{\omega}^{8/3}+(\hat{\omega}-\tilde{\omega})^2}\int_{-\frac{\pi}{2}}^{\frac{\pi}{2}}e^{-q^2[(1-\sin\bar{\phi}\tilde{\omega}^{2/3})^2 + \Gamma^2\cos^2\bar{\phi}\,\tilde{\omega}^{4/3}]}\,d\bar{\phi}d\tilde{\omega}\,. \tag{37}$$

This integral has been evaluated numerically for a set of values of ξ and q, and for a range of angle θ.

5. Experimental Procedure

The experimentalist is interested in obtaining the parameters Γ_1 and ω_{K_s} from the measurements obtained. Even if the measured spectrum was noise-free, one would find:

a) a peak of the spectrum is not located at ω_{K_s}, and

b) the relation between the measured width and the parameter Γ_1 is non-trivial since it is an involved function of K_{oi}', σ_x and θ.

Real spectra are usually noisy and thus some kind of curve fitting algorithm is generally used. A popular procedure is to curve fit the measured spectrum with the theoretical spectrum using ω_{K_s} and Γ_1 as the adjustable parameters. We have not succeeded in formulating an efficient numerical algorithm for the theoretical spectrum. We offer the following algorithm as a good approximate method for extracting the parameters ω_{K_s} and Γ_1 from a measured spectrum:

a) Fit a three parameter gaussian distribution plus a constant base-line to the measured spectrum using a least squares fitting procedure. The fit function is of the type:

$$G(\omega,\omega_o,\sigma_M,B) = A + B\, e^{-\frac{(\omega-\omega_o)^2}{2\sigma_M^2}},$$

where A is the base line, B is a constant, ω_o is the mean frequency and σ_M is the standard deviation. This fit yields two useful parameters, ω_o and σ_M.

b) From the optical configuration, obtain $q(=\sigma_x K_{oi}'=K_o\sigma)$ and θ.

c) From the graph (fig. 2) obtain $\tilde{\sigma}_I = \sigma_I/\omega_o$ for the given q and θ. σ_I can also be computed by first evaluating $S_I(K_{oi}',\omega)$ for given q and θ and then doing a three parameter gaussian fit.

d) From the graph (fig. 3) or the formula (eq. 38), compute

$$\xi/\tilde{\sigma}_M = P(\frac{\tilde{\sigma}_I}{\tilde{\sigma}_M},\theta).$$

e) From the graphs like figs. 4 and 5 read $\tilde{\omega} = \omega'/\omega_o = f(q,\theta)$. Since q, θ and ω_o are known, ω' is known.

At this point, $\tilde{\sigma}_M$, $\tilde{\sigma}_I$ and θ are known and hence ξ(or Γ_1) can be computed.

117

In order to construct the parameters, for the fitting algorithm, the spectrum $S(K_{oi}', \hat{\omega})$ has been evaluated numerically for a set of values of ξ, q and θ. A gaussian distribution is then fitted over the spectrum $S(K_{oi}', \hat{\omega})$ using a least square procedure and the center frequency ω_0 and standard deviation σ_M are thereby obtained. There exists a functional relationship between Γ_1/σ_M and σ_I/σ_M which depends on θ. For the following four angles, the relationship can be expressed as

$$\frac{\Gamma_1}{\sigma_M} = 0.925372 \ (1 - \frac{\sigma_I^2}{\sigma_M^2}) \ \exp \ (a(\theta) \ \frac{\sigma_I^2}{\sigma_M^2}) \quad (38)$$

where $a(\theta)$ is given below:

θ	$a(\theta)$
0°	0
45°	-.011576
60°	-.060975
75°	-.226475

The constant 0.925372 is the ratio Γ_1/σ_M when a gaussian distribution is fitted to a pure Lorentzian distribution of half width at half height of Γ_1. The expression corresponding to $\theta = 0°$ is of the same form as that of Härd et al.[10] but has been expressed in terms of standard deviations rather than the half widths at half heights. The influence of angle θ is expressed through the exponential term. A plot of Γ_1/σ_M versus σ_I/σ_M for $\theta = 0°$, 60° and 75° has been illustrated in Figure 2. This graph may be utilized to obtain Γ_1/σ_M when σ_I/σ_M is known.

Another interesting feature of this fitting procedure is the shift in the center frequency of the gaussian with respect to that of Lorentzian distribution. The center frequency of the best fit gaussian distribution

118

is plotted as a function of Γ_1/σ_M for a range of angle 0 and for two extreme values of interest of q, namely 6 and 25 in Figures 4 and 5. For smaller values of q there is very large upward shift of the center frequency, particularly for larger angle of incidence. For some values of θ there is a downward shift of the center frequency as well, which is due to the fact that the damping is weighted heavily towards the smaller frequencies in the spectrum. One point of interest is that these departures from the mean frequency are significant only for smaller beam size and for angles greater than 60°. When beam size is such that q = 25, the maximum departure of center frequency is less than 0.8% even at an angle of 75°. For angles of incidence smaller than 60°, the departure is less than 0.1% and is practically independent of Γ_1/σ_M . It is therefore strongly recommended that the experimentalist chooses a sufficiently fat beam and arranges the experimental set-up so that the angle of incidence does not exceed 60° in order to minimize the instrumental effects.

As an example to demonstrate the method, we study scattering from ethanol surface. The original data were obtained as 400 point autocorrelation functions. These were then converted to 256 point digital spectra by a digital Fourier transform. The time and frequency parameters for the numerical procedure along with the optical parameters are given in the table below:

:Table:

	Ethanol
correlation time step	10 μsec.
spectrum frequency step	195.31 Hz
θ	7.2°
K_o	247 cm^{-1}
q	9.5

119

The parameters ω_o and σ_M obtained by three parameters gaussian fit

after the removal of base line from the measured spectrum of ethanol are

ω_o = 20322 rad/sec and σ_M = 3470 rad/sec. From Figure 2, the value of

σ_I for q = 9.5 is obtained to be σ_I = 2267 rad/sec. Further from Figure 3,

we obtain the value of Γ_1/σ_M corresponding to the value of σ_I/σ_M = 0.6532.

Therefore Γ_1 = 1841 rad/sec. The center frequency is 0.9987 ω_o. From these

measured data, we obtain the value of surface tension and viscosity of ethanol

as

$$\gamma = \rho \; \frac{\omega_o^2}{\left|(K_o \cos\theta)^3\right|} = 22.16 \text{ dynes/cm, and}$$

$$\nu = \frac{\eta}{\rho} = \frac{\Gamma_1}{2 K_o^2 \cos\theta^2} = 0.0153 \text{ S or } \eta = 0.0121 \text{ P.}$$

In these calculations, it is assumed that Y_1 = 1.00. The calculations

for the spectrum off   the water surface are performed in a similar fashion and

gave appropriate values of the surface tension and viscosity.

As a further check, the measured parameters were substituted into the

numerical scheme (eq. 37) for computing the spectra. Figures 6 and 7 show

the computed and measured spectra plotted together for ethanol and water.

The fit is excellent except at the low frequency edge. The error at the low

frequency end is due to the non-white noise present in the measurement system

and can be eliminated.

6. Fabrication of Gratings

Though the theory presented here utilizes sinusoidal grating, for

reasons of convenience in fabrication, a binary grating is used in practice.

120

Experience has shown us that a grating having a diffraction efficienty of less than 10^{-4} gives good results, although satisfactory correlograms have been obtained with gratings having the diffraction efficiency of 10^{-2}. The diffraction efficienty, $\eta_a(m)$ in m^{th} order of a binary grating of period 'd' and width of the opaque region 's' is given by

$$\eta_a(m) = (\frac{s}{d})^2 (M'-M'')^2 \left(\frac{\sin (\pi m\ s/d)}{\pi m\ s/d}\right)^2 ,$$

where M' and M'' are the extremal values of transmittance. For a binary grating M' is about unity and M'' = 0, while for grey grating M'' takes a finite value. It can be seen that the diffraction efficiencies of complimentary gratings are the same. Therefore a grating with narrow lines in transparent background is used for experiments. For such a grating, the sinc function can be approximated by unity for the first few orders. Thus

$$\eta_a(m) = (\frac{s}{d})^2 (M'-M'')^2 .$$

The diffraction efficiency can be controlled independently by two different mechanisms. We have fabricated gratings with s/d ranging from 0.1 to 0.0125. One can also exercise a fairly good control on (M' - M'') during development if an emulsion with larger latitude is used.

7. Discussion and Conclusion

The thrust of this paper is the analysis of the grating heterodyne apparatus which we believe to be superior for the measurement of the spectra of surface waves induced by natural fluctuations occurring at liquid-fluid interfaces. For simplicity we have assumed that the interface is between a simple liquid and its vapor. Even for that case we have used a simplified

line shape formula (eq. 35) as noted in a previous section.

We wish to point out that generalizations can be made easily without changing the theory we have developed and illustrated with simple systems. Firstly, our formulas can be easily adapted for liquid-liquid interfaces. If the upper phase is sufficiently thick, >ca 5 mm, the beam paths at the vapor-liquid and liquid-liquid interfaces will be sufficiently separated that one can compute the scattering geometry inside the liquid phase by Snell's law using the appropriate refractive index numbers. A simple modification of the equations containing the refractive index, e.g., eq. 11, to now read as the refractive index ratio is sufficient. The wave numbers of the incident and scattered light must be computed for the medium into which the scattering occurs.

The second generalization is that of the response function of the surface. Equation 4 is sufficiently general for small amplitude waves for which the modes are decoupled. However, we have used a rather simple response function which takes into account only the surface tension of a one component liquid, its density and viscosity. Equation 29 is still exact within the decoupled mode assumption. The formula for the center frequency, Equation 30a, is also correct because the dimensionless group, Y_l, can be computed once the response function for the surface is formulated as was first shown by Hansen and Mann[11]. The major approximation we have made for simplicity is to use the single Lorentzian line shape formula in Equation 35. We wish to emphasize that it is only a minor modification to use more accurate representations of the spectrum associated with the response function of the surface[12,14].

Of special interest is the extension of $A(\vec{K}_s;\omega)$ to the situation in which monolayers are adsorbed or spread on the interface. In that case, $A(\vec{K}_s;\omega)$ depends on the surface tension as well as the visco-elastic properties of the monolayer[13]. In principle, the order parameters will also be involved. Unfortunately, the center frequency is still given by Equation 30a for which the range of Y_1 is roughly $Y_1 \in (.9, 1.1)$, where Y_1 is a function of the bulk and surface properties associated with the scattering interface. In particular the center frequency shift is relatively insensitive to the surface visco-elastic coefficients.

The line shape is sensitive to the surface visco-elastic coefficients. Mann et al.[14] have shown some of the characteristics to be expected using the simple Lorentzian function and assuming that the classical boundary conditions for deriving the surface response function are correct. Bouchiat and Meunier [15] derive the dispersion function using appropriate boundary conditions for the correlation function coupling the vertical displacement of the interface and the vertical component of the bulk velocity field in the limit close to the surface. The power spectrum function is derived which is equivalent to what we need for Equation 35. Unfortunately they have not included the complications of a spread monolayer at the surface. So far as we know, the Mann et al. formulation of the capillary ripple problem[11,14,5] includes all of the information of interest about the surface response function of monolayer covered surfaces except certain orientation effects. The formulation of Bouchiat and Meunier[15] develops the appropriate power spectrum dispersion . These two formalisms can be combined rather easily so that accurate predictions can be made for $A(\vec{K}_s;\omega)$ for a large range of monolayer conditions. This work is left for future publications.

Our analysis here has generalized the range of validity over which the grating heterodyne technique can be used to obtain the true power spectrum characteristics of fluctuating interfaces. Our formulas are consistent with those of Härd et al.[10] in the limit of K_0 being very large and θ smaller than $45°$. However, this limit is rather restrictive in practical experimental work.

References

1. M.V. Smoluchowski, Ann. Physik $\underline{25}$, 225 (1908).

2. L.I. Mandelshtam, Ann. Physik $\underline{41}$, 609 (1918).

3. C.V. Raman and L.A. Ramdas, Proc. Roy. Soc. (London) $\underline{A103}$, 561 (1924).
   $\underline{A109}$, 150, 272 (1925).

4. H.Z. Cummins and H.L. Swinney, Progress in Optics [Ed. E. Wolf, Academic Press], Vol. $\underline{8}$, 133-200 (1970).

5. J.A. Mann, K.C. Porzio, "Capillarity: The Physical Nature of Fluid-Fluid Interface including the Problem of Biomembrane Structure". MTP International Review of Science, Series Two, Vol. 7, M. Kerker ed., Butterworths, London (1975).

6. D. Byrne and J.C. Earnshaw, J. Phys. D: Appl. Phys. $\underline{12}$, 1133 (1979).

7. D. McQueen and L. Lundström, J. Chem. Soc. Faraday Trans. $\underline{I69}$, 694 (1973).

8. M.A. Bouchiat, J. Meunier and J. Brossel, C.R. Acad. Sc. Paris (series B) $\underline{266}$, 255 (1968).

9. D. Byrne and J.C. Earnshaw, J. Phys. D: Appl. Phys. $\underline{10}$, L207 (1977).

10. S. Hård, Y. Hammerius and O. Nilsson, J. Appl. Phys. $\underline{47}$, 2433 (1976).

11. R.S. Hansen and J.A. Mann, J. Appl. Phys., $\underline{1}$, 152 (1964).

12. J. Meunier, D. Cruchon and M.A. Bouchiat, C.R. Acad. Sci. Paris (Series B) $\underline{268}$, 92, 422 (1969).

13. D. Byrne and J.C. Earnshaw, J. Phys. D: Appl. Phys. $\underline{12}$, 1145 (1979).

14. J.A. Mann, J.F. Boret, F.J. Dechow and R.S. Hansen, J. Coll. Interf. Sci. $\underline{37}$ (1), 14 (1971).

15. M.A. Bouchiat and J. Meunier, J. de Phys. $\underline{33}$ (2-3), C1-141 (1972).

Appendix

We wish to show that

$$<a_{K_s}(t) \, a_{K_s}'(t+\tau) \cos \Phi_i(t) \cos \Phi_i(t+\tau) > = \frac{1}{2} <a_{K_s}(t) \, a_{K_s}'(t+\tau)> \delta \, (\vec{K}_s - \vec{K}_s').$$

We make the following assumptions:

1) The phase Φ_i is statistically independent of the amplitude $a_{K_s}(t)$ and are distributed uniformly between 0 and 2π. Therefore we can replace $<\cos \Phi_i(t) \cos \Phi_i(t+\tau)>$ with its expected value $1/2$.

2) The scattering at $\vec{K}_s$ is statistically independent of scattering at any other vector $\vec{K}_s'$.

Let us express $<a_{K_s}(t) \, a_K'(t+\tau)>$ through the Fourier transform relation of the form

$$<a_{K_s}(t) \, a_{K_s}'(t+\tau)> = \frac{1}{(2\pi)^2} \int\int <a(x,y;t) \, a(x',y';t+\tau)> e^{-i(K_{sx}x+K_{sy}y)}$$

$$\cdot \, e^{-i(K_{sx}'x+K_{sy}'y)} dx \, dy \, dx' \, dy', \qquad \text{(A-1)}$$

where $a(x,y;t)$ is the space domain description of the amplitude $a_{K_s}(t)$.

If we make the following substitutions,

$$x' = x + \Delta x,$$

$$y' = y + \Delta y, \text{ or}$$

$$\vec{r}' = \vec{r} + \vec{\Delta r},$$

the above expression is rewritten as

$$<a_{K_s}(t) \, a_{K_s}'(t+\tau)> = \frac{1}{(2\pi)^2} \int\int <a(\vec{r};t) \, a(\vec{r}+\vec{\Delta r};t+\tau)> e^{-i(K_{sx}-K_{sx}')x}$$

$$\cdot \, e^{-i(K_{sy}-K_{sy}')y} \cdot e^{i K_{sx} \Delta x} \cdot e^{i K_{sy} \Delta y} dx \, d\Delta x \, dy \, d\Delta y. \quad \text{(A-2)}$$

126

The term $\langle a(\vec{r};t)\, a(\vec{r}+\Delta\vec{r};t+\tau)\rangle$ is seen to be the space-time correlation function for the surface scattering irradiance. If the system is homogeneous in two dimensions, we get

$$\langle a(\vec{r};t)\, a(\vec{r}+\Delta\vec{r};t+\tau)\rangle = H(\Delta\vec{r};\tau), \tag{A-3}$$

i.e., the system is statistically stationary both in time and space. The boundaries are not important at all.

Equation (A-2) can be rewritten as

$$\langle a_{K_s}(t)\, a_{K'_s}(t+\tau)\rangle = \frac{1}{(2\pi)^2}\iint H(\Delta\vec{r};\tau)\, e^{i(\vec{K}_s-\vec{K}'_s)\cdot\vec{r}}\cdot e^{i\vec{K}'_s\cdot\Delta\vec{r}}\, d\vec{r}\, d\Delta\vec{r}\ .$$

Carrying out the integration on $\vec{r}$ leads to

$$\langle a_{K_s}(t)\, a_{K'_s}(t+\tau)\rangle = \frac{\delta(\vec{K}_s-\vec{K}'_s)}{2\pi}\int H(\Delta\vec{r};\tau)\, e^{i\vec{K}'_s\cdot\Delta\vec{r}}\, d\Delta\vec{r}\ .$$

The integral can be recognized as Fourier transform of $H(\Delta\vec{r};t)$ and hence

$$\langle a_{K_s}(t)\, a_{K'_s}(t+\tau)\rangle = \langle a_{K_s}(t)\, a_{K'_s}(t+\tau)\rangle\, \delta(\vec{K}_s-\vec{K}'_s)\ .$$

Therefore we can sum up as

$$\langle a_{K_s}(t)\, a_{K'_s}(t+\tau)\, \cos\Phi_i(t)\, \cos\Phi_i(t+\tau)\rangle$$

$$= \langle a_{K_s}(t)\, a_{K'_s}(t+\tau)\rangle\, \langle\cos\Phi_i(t)\, \cos\Phi_i(t+\tau)\rangle$$

$$= \frac{1}{2}\langle a_{K_s}(t)\, a_{K'_s}(t+\tau)\rangle$$

$$= \frac{1}{2}\langle a_{K_s}(t)\, a_{K'_s}(t+\tau)\rangle\, \delta(\vec{K}_s-\vec{K}'_s)\ .$$
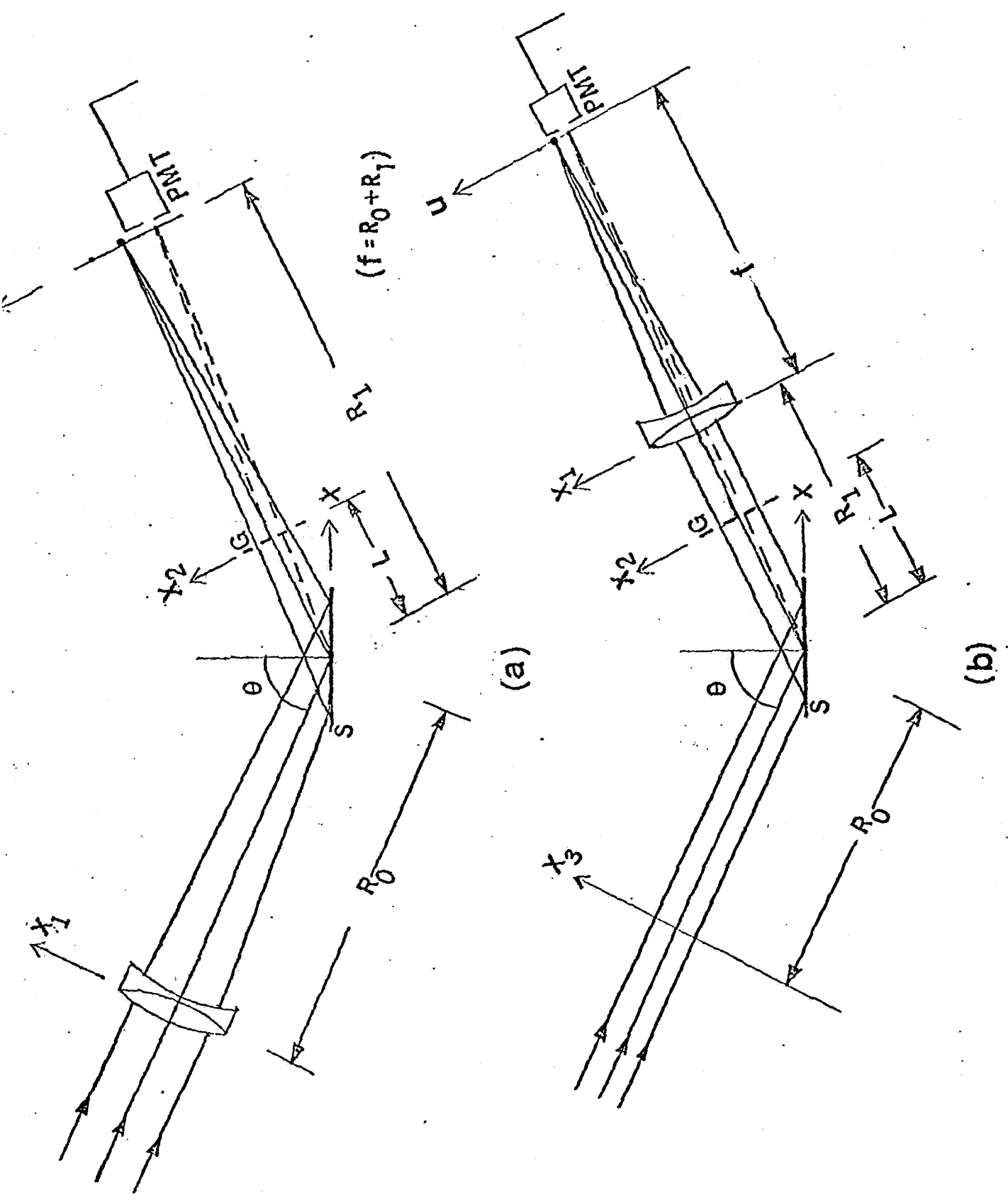
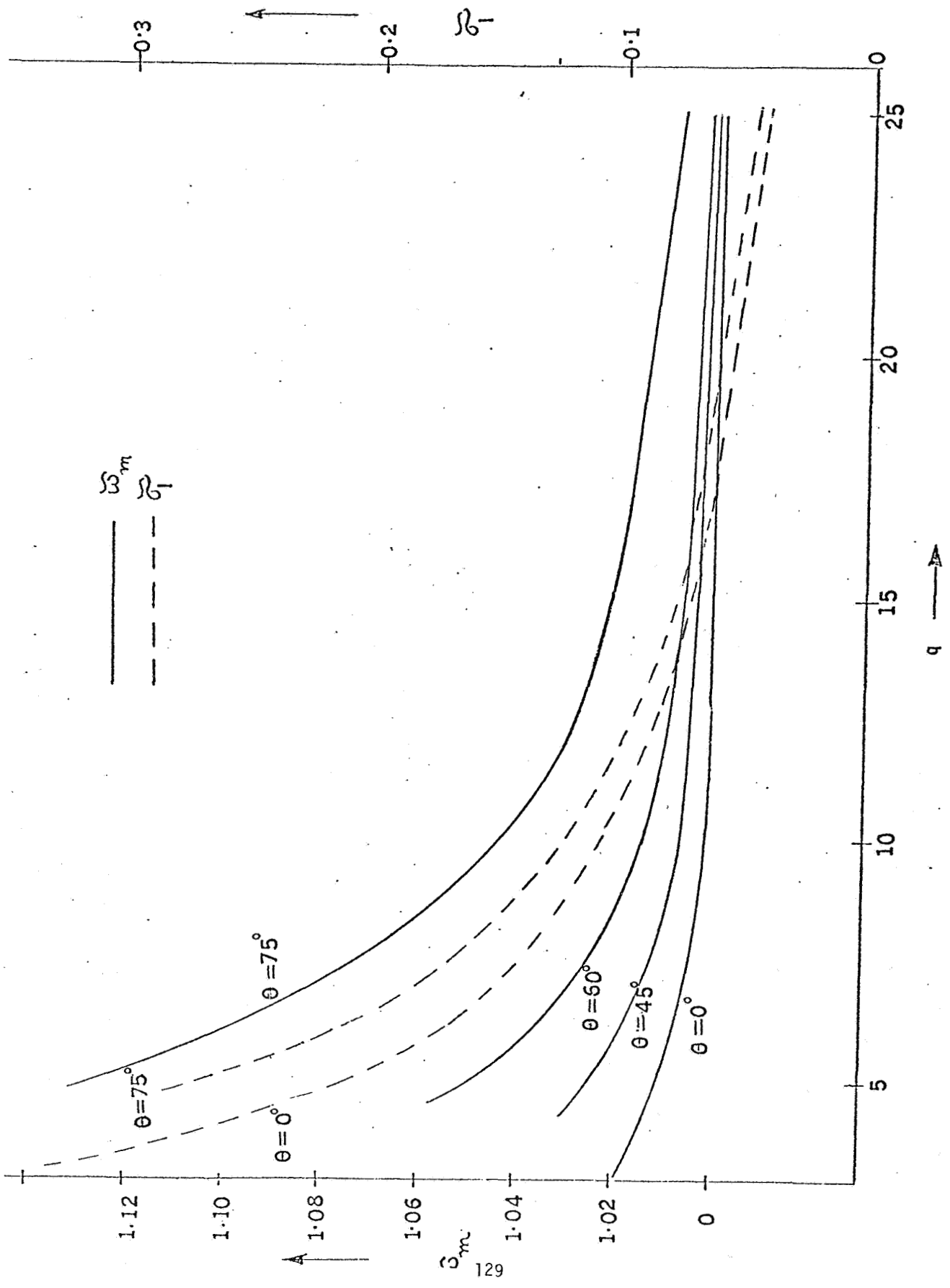FIG. 1. : SCHEMATICS OF THE EXPERIMENTAL SET-UP FOR HETERODYNE APPARATUS

128

FIG. 2 : DEPENDANCE OF THE MEAN FREQUENCY $\bar{\omega}_m$ AND STANDARD DEVIATION σ_Π OF THE INSTRUMENTAL FUNCTION ON q_v.
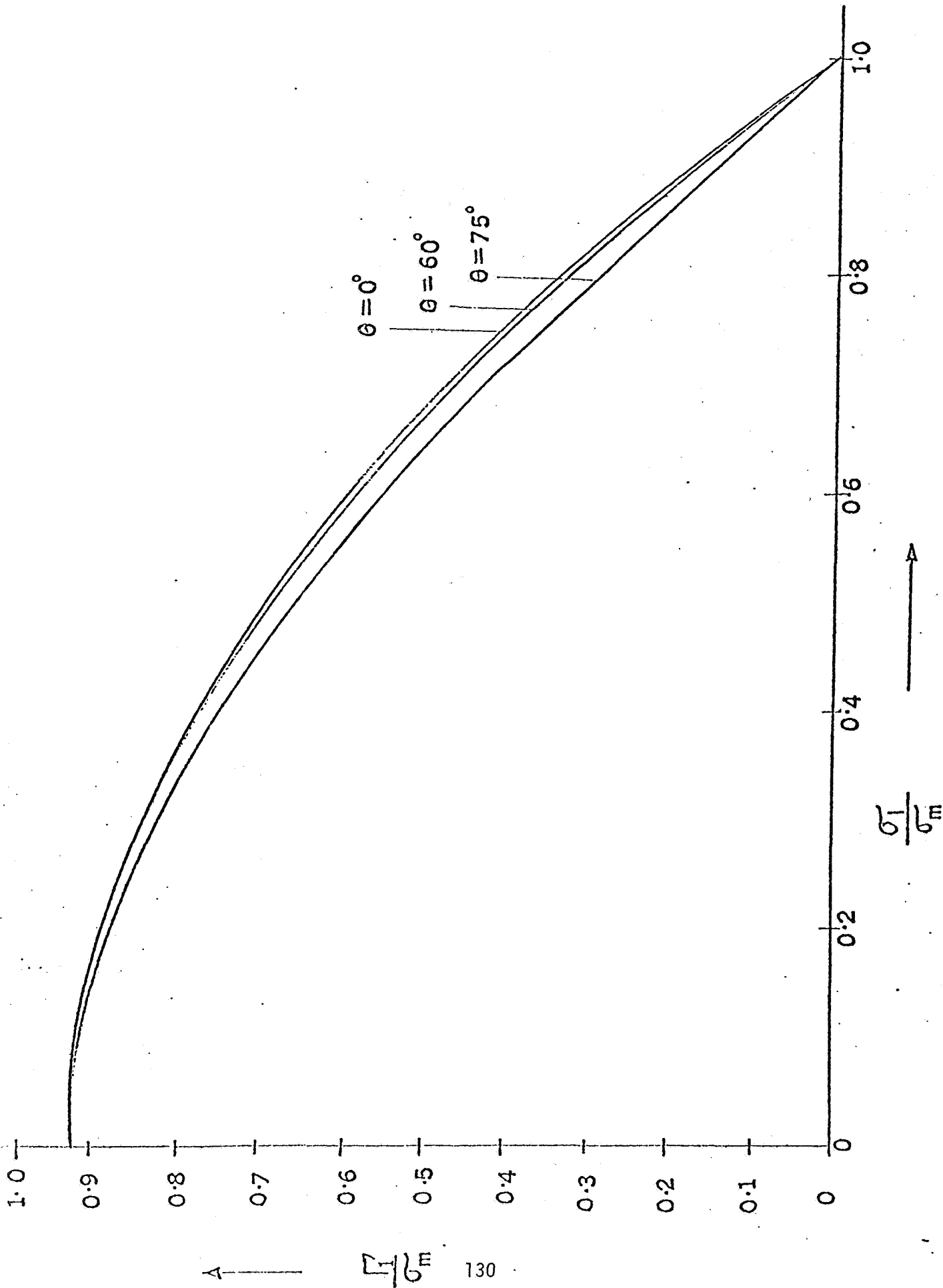
129

FIG.3 : RELATIONSHIP BETWEEN THE STANDARD DEVIATIONS OF INSTRUMENTAL FUNCTION AND MEASURED SPECTRUM, AND HMHH FOR LORENTZIAN SPECTRUM FOR A SET OF INCIDENT ANGLES
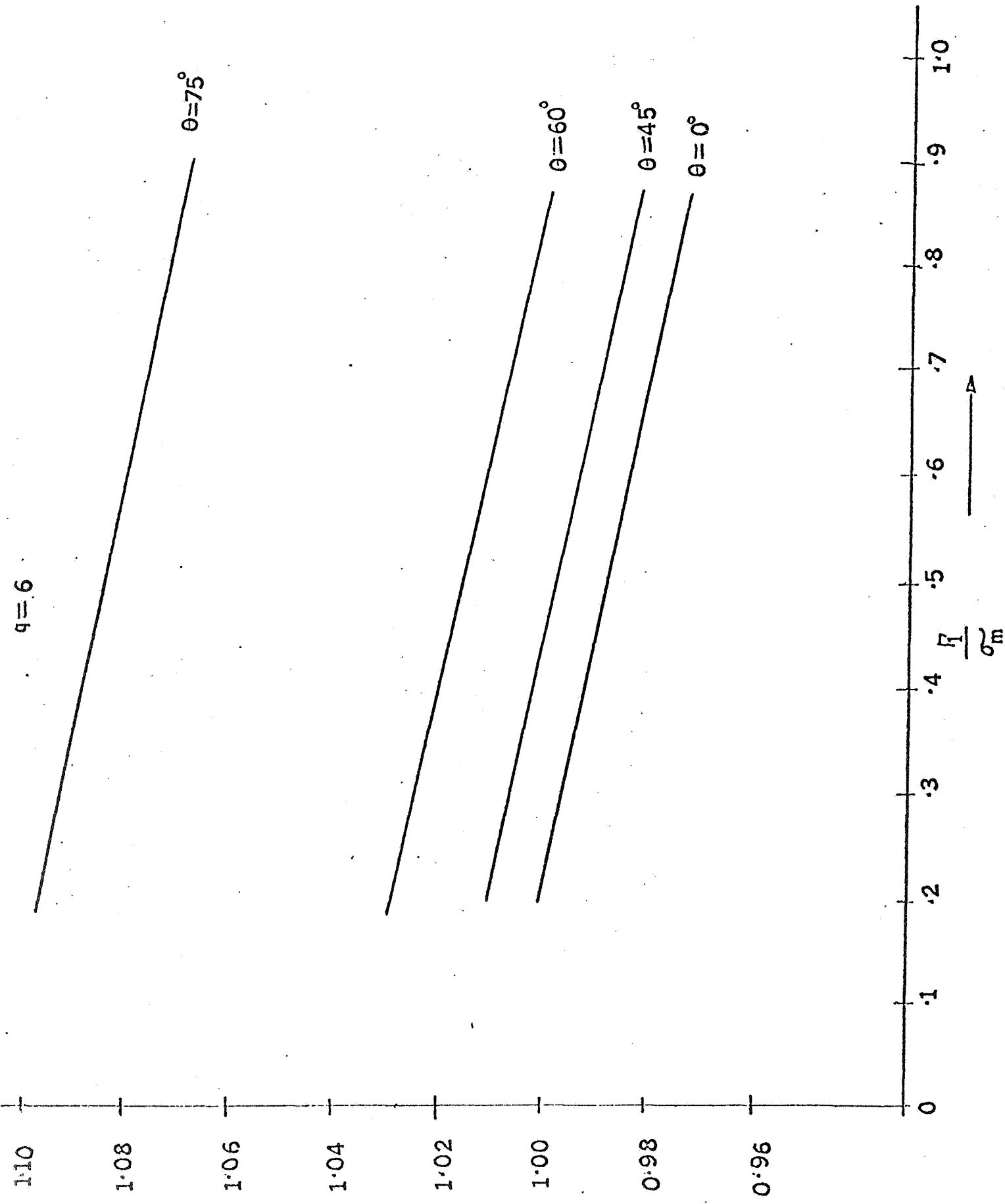
130

FIG. 4 : VARIATION OF MEAN FREQUENCY $\tilde{\omega}$ OF THE MEASURED SPECTRUM WITH $\dfrac{F_1}{\sigma_m}$ FOR $\dot{q}_1 = 6$.
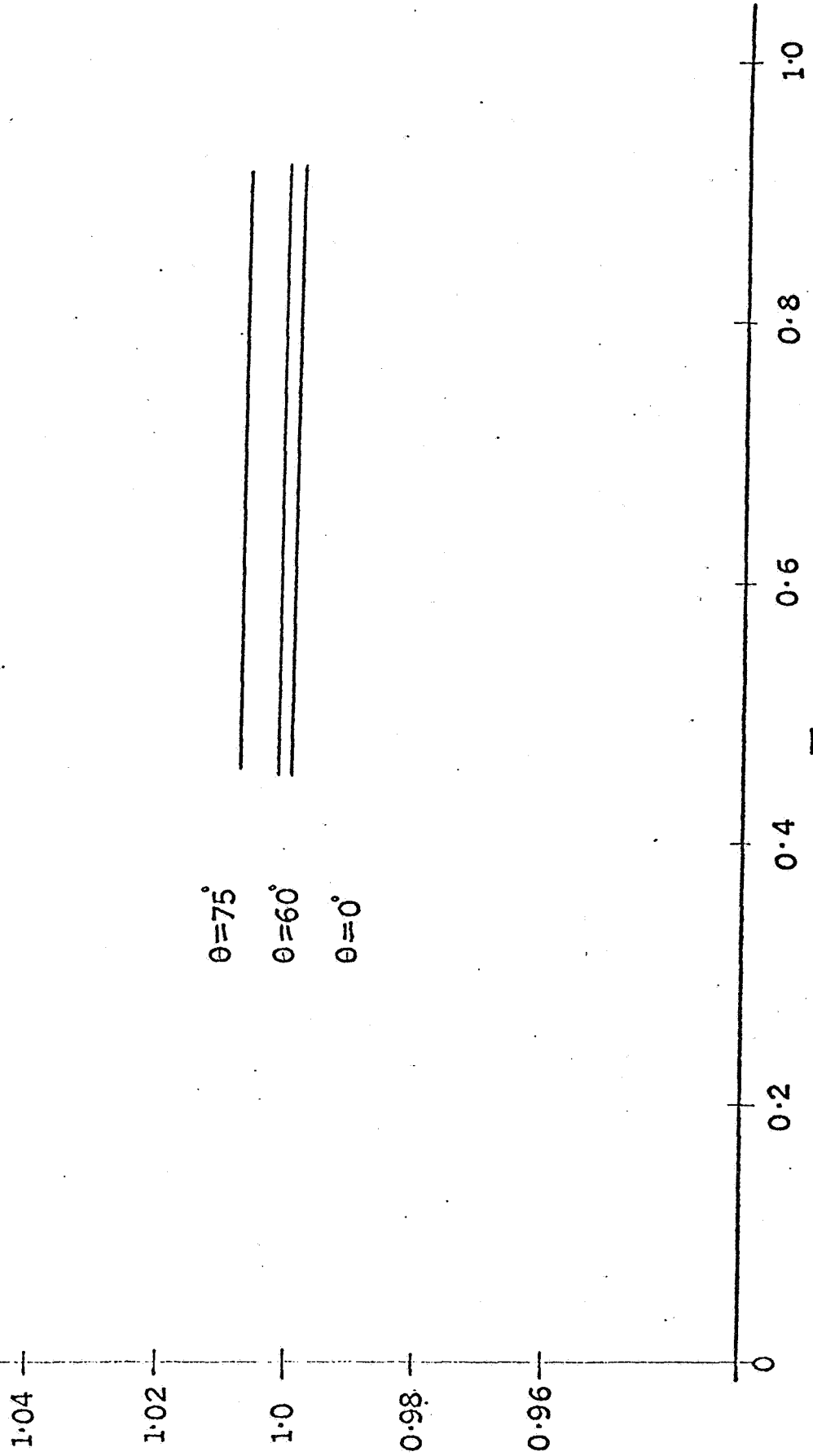
FIG.5 : Variation of mean frequency $\tilde{\omega}$ of the measured spectrum with $\dfrac{\Gamma_1}{\sigma_m}$ for $q_v = 25$.
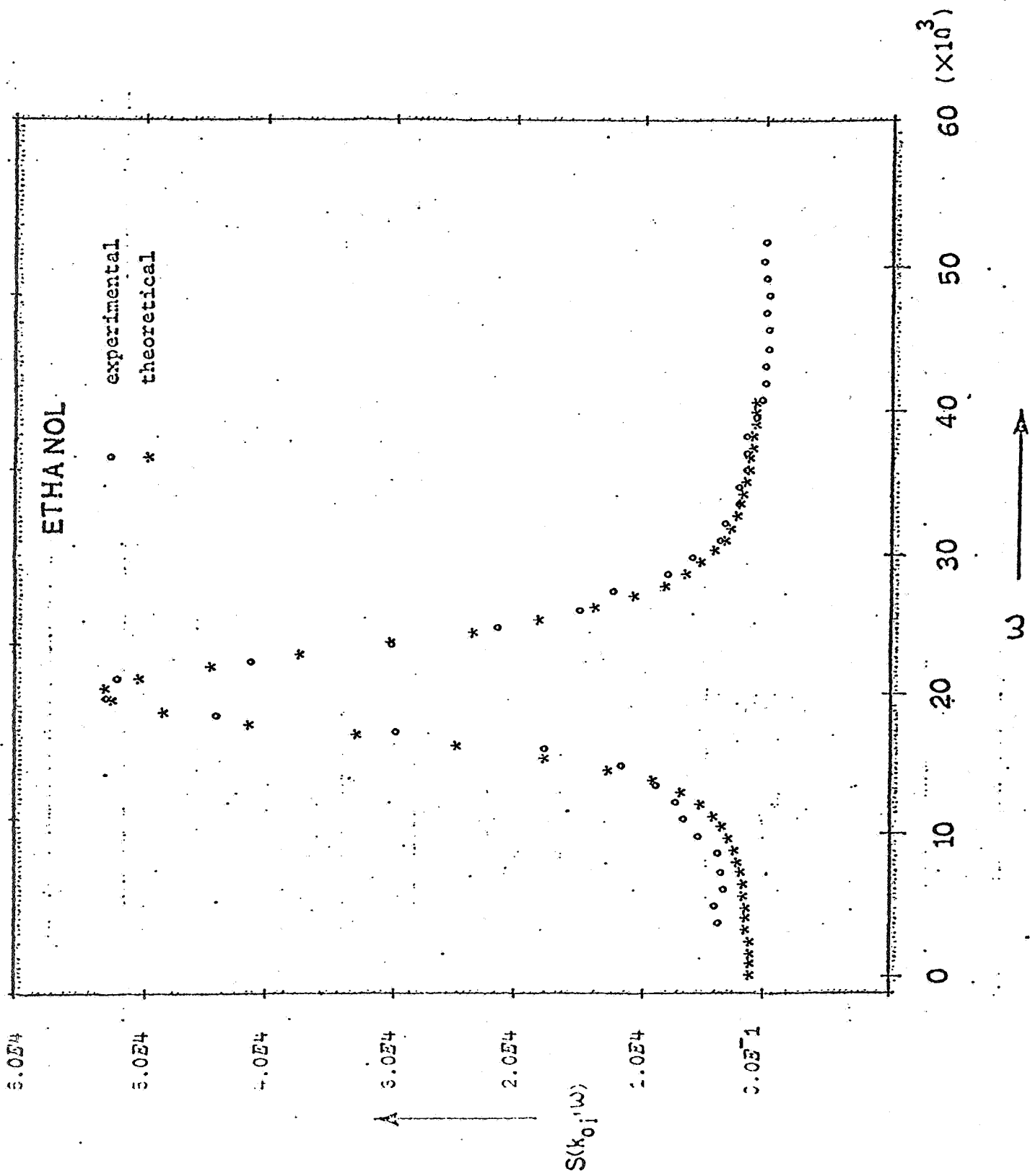
FIG.6 : EXPERIMENTAL AND THEORETICAL SPECTRA FOR ETHANOL
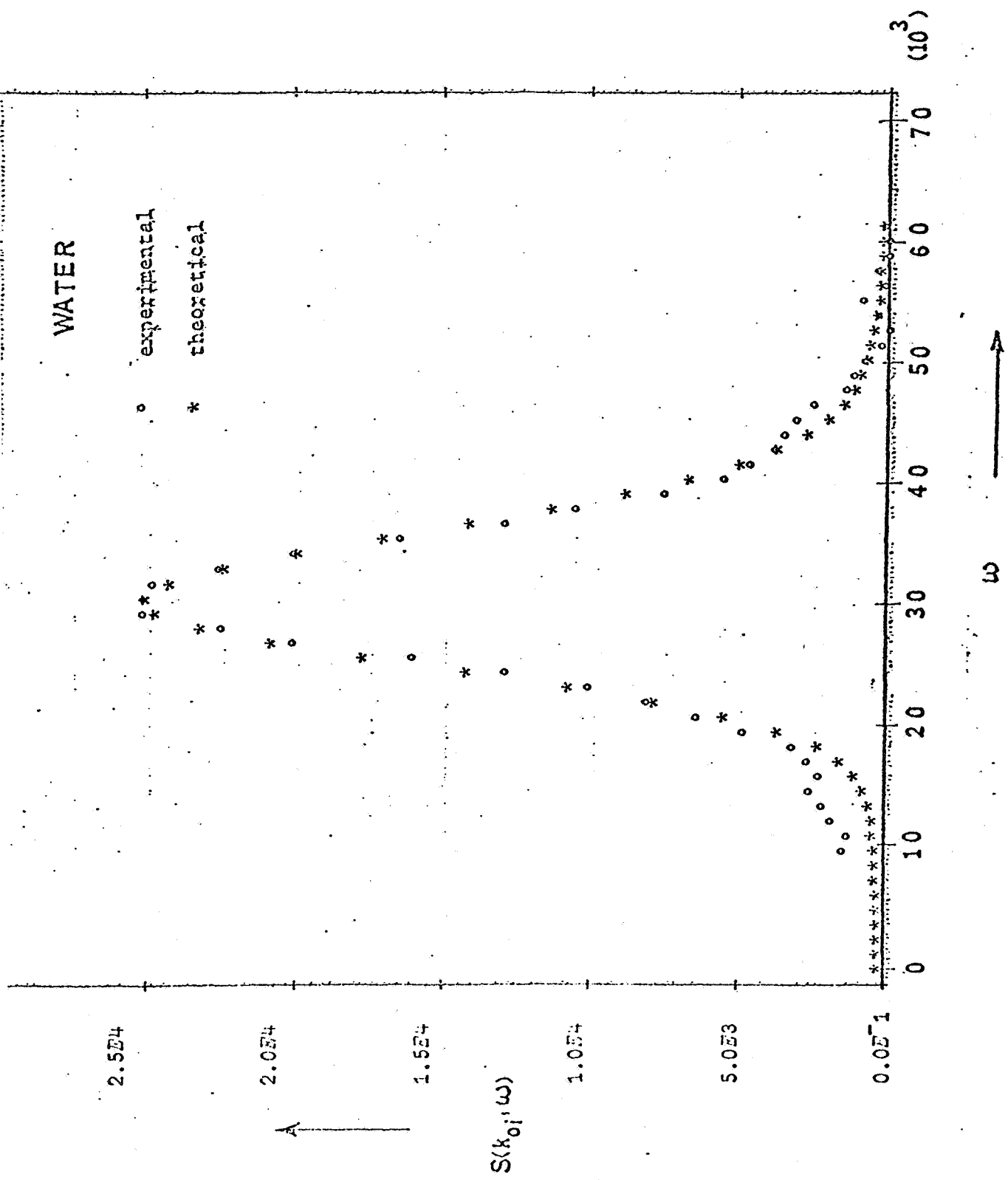
133

FIG.7 : EXPERIMENTAL AND THEORETICAL SPECTRA FOR WATER

134

B. Report of the measurement of surface flow velocity with ripplon scattering

This manuscript represents a report of the work by Dr. R. S. Sirohi on

the surface flow field problem. Notice that the correspondence between

theory and experiment was good. Sirohi points out the limitation of the

technique but Edwards and I are more optimistic about the lower limits of

teh speeds that can be determined when using a careful curve fitting procedure.

MEASUREMENT OF SURFACE FLOW VELOCITY WITH RIPPLON SCATTERING

R. S. Sirohi, R. V. Edwards, J. A. Mann, Jr.
Chemical Engineering Department
Case Western Reserve University
Cleveland, Ohio 44106

Abstract

It is shown that the light scattered from the ripplons on a moving liquid interface can be used to measure the velocity fields in the interface. The technique measures the true interface velocity. It is, however, limited to the measurement of relatively fast moving interfaces because 1) the scattered irradiance is large only in a very small angular range about the specularly reflected beam, and 2) the concerted influence of instrumental and natural broadening of the power spectrum leads to severely overlapping doublet for low velocity fields.

1. Introduction

The scattering of light from capillary waves has been used for the study of visco-elastic properties of the liquid interface.[1-4] It is not always appreciated that surface waves can be quantized and represented by quasi-particles called ripplons. In this language the light scattering problem can be thought of as a photon-ripplon scattering process. The quasi-particle model suggests that ripplons can be used as tracers for following surface velocity fields much as solid particles are used in tracing velocity fields in bulk fluids using laser "doppler"[6] effects. Unlike solid particle tracers that might be used for the same purpose, ripplons are confined to the true interface.

We show that surface velocity fields can be measured easily but there are experimental limits to the range of speeds that can be covered with the state of the art techniques. We will describe the physical basis for the technique, show results of measurements made on a simple system and comment on the range of applications we can anticipate in view of the limitations.

2. Theory

In most of the recent studies, an optimal grating is an essential element of the heterodyne scheme. The grating provides a well defined and controllable local oscillator by diffracting the beam into various order spots in the far-field. The photo-detector receives light, scattered from the capillary waves, that propagates along with one of the diffracted beams from the grating. Mixing of the selected diffracted beam and the scattered light beam occurs on the surrace of the square-law detector; a photomultiplier tube is used in our experiments. The time varying photo-current is studied either in the time domain by a correlator or in the frequency domain by a

137

spectrum analyzer. The function of interest, however, is the power spectrum

of the photo-current. The central frequency ω_o of the power spectrum and

the wave vector K_o of the surface wave are related through a well known

dispersion equation for capillary waves:

$$\omega_o^2 = Y_I \frac{Y}{\rho} K_o^3 = \beta K_o^3 \tag{1}$$

where γ is the surface tension and ρ is the density of the liquid. Y_1 is a

dimensionless group whose value lies between 0.95 and 1.05 and can be

calculated exactly.[5] The width of the spectrum can be calculated exactly[4,5]

and depends on the bulk viscosity as well as other physical properties of

the surface and bulk phases.

The ripplons are decaying travelling waves propagating in random

directions generated by local thermal fluctuations in the surface profile.

If we consider the propagation of waves along x direction, on the average,

equal number of ripplons will cross any line in the surface $x = x_1$ at any

instant of time from both positive and negative x directions. If the

interface is translated along the positive x direction with a velocity v,

the frequency of ripplons propagating along the positive x direction is

increased by $K_o v$ while of those propagating along negative x direction is

decreased by the same amount. The power spectrum of the photo-current, thus,

exhibits two peaks situated at $\omega = \omega_o \pm K_o v$. A detailed mathematical

analysis[7] leads to a dispersion equation

$$(\omega \pm K_o v)^2 = Y_I \frac{Y}{\rho} K_0^3 \tag{2}$$

This equation has two roots at $\omega = \omega_o \pm K_o v$. The purpose of this note is

to shown that the study of the field scattered from a moving interface can

be used to extract surface velocity information. It is known that the field

scattered by ripplons is mostly concentrated in a very narrow angular range
about the specularly reflected beam, and hence relatively coarse gratings
$(K_g \leq 1000 \text{ cm}^{-1})$ are employed in practice. A measurable frequency shift
can be obtained from relatively fast moving interface, > 1 cm/sec.

The important factor which restricts the application of this technique
to the measurement of fast surface flows is the concerted influence of
instrumental broadening and natural broadening of the power spectrum. It
has been shown[8] that the power spectrum of the photo-current, when both
instrumental and natural broadenings are considered, is given by

$$S(K_o; \hat{\omega}) = \frac{1}{3} Q_i^2 \frac{\omega_o^{1/3}}{\beta^{4/3}} \int_{-\infty}^{\infty} \frac{\xi \tilde{\omega}^{5/3}}{\xi^2 \tilde{\omega}^{8/3} + (\hat{\omega} - \tilde{\omega})^2} \int_{-\pi/2}^{\pi/2} e^{-q^2[(1-\sin\phi\tilde{\omega}^{2/3})^2 + \Gamma^2 \cos^2\phi\tilde{\omega}^{4/3}]} d\phi d\tilde{\omega} \quad (:$$

where $\tilde{\omega} = \frac{\omega'}{\omega_o}$, $\hat{\omega} = \frac{\omega}{\omega_o}$, $\xi = \frac{2\nu K_o^2}{\omega_o}$, $q = \sigma_x K_o$ and $\Gamma = \cos\theta$. ω' is the frequency
corresponding to the peak of the spectrum for wave vector K_s, and θ is the
angle of incidence. Q_i is a function of experimental parameters. The
instrumental width is governed by q and θ.

When the interface is moving, in the laboratory frame, uniformly with
velocity v, the resultant spectrum is obtained by the linear superposition
of the two spectra with their peaks at $\omega_o - K_o v$ and $\omega_o + K_o v$. Therefore
the resultant spectrum $S_c(\hat{\omega})$ is given by

$$S_c(\hat{\omega}) = S_{\omega_o + K_o v}(\hat{\omega}) + S_{\omega_o - K_o v}(\hat{\omega}),$$

where $S_{\omega_o + K_o v}(\hat{\omega})$ is the spectrum with the peak located at $\omega_o + K_o v$. For
smaller velocities the resultant spectrum may not be resolved and hence
exhibits only a single peak. Velocity information is then contained in
the shape of the spectrum. In fact, the shape of the spectrum can be

analyzed for extracting velocity information for speeds < ca 1 cm/sec.

However, as the velocity of flow increases, the two peaks may develop.

Indeed there is a velocity for which the resultant spectrum is just resolved.

One can define various criteria for this just resolved spectrum depending

on the signal processing scheme. The point to note is that the resultant

spectrum may be resolved even for smaller velocities provided a grating of

higher K_g is used.

3. Experimental

In order to confirm the theory, the experiments are conducted on the

surface of ethanol. A circular disk of ca 30 cm in diameter containing

ethanol was rotated slowly (6 sec per revolution) and the laser beam was

reflected off the surface at various distances from the center of rotation.

A grating of $K_g = 247$ cm^{-1} was used, and the beam was incident at an angle

of 24.8°, giving an effective K_o of 224.8 cm^{-1}. The beam at the surface

was such that it provided a value of $q = \sigma_x K_o = 18$.

The measurements are made at various locations on the surface of

ethanol in the rotating disk. The original data was obtained as 400 points

auto-correlation functions. These were then converted to 256 points spectra

by digital Fourier transform methods. Figure 1a shows the spectrum from

the stationary ethanol surface. Figure 1b shows the spectrum obtained by

shining the laser beam at a location where the mean velocity was 5.5 cm/sec.

The spectrum is not resolved and appears identical in shape to that of

Figure 1a except for the higher width. However, when the mean velocity is

9.5 cm/sec, the spectrum is well resolved with the frequency separation

between the two peaks of 635 Hz. This spectrum is shown in Figure 1c. The

theoretical spectra using the experimental data in eqn. (3) are computed and

plotted in Figures 1a, 1b and 1c for the sake of comparison. There is an

excellent fit between experimental and theoretical spectra.

Figure 2 shows the plot between the separation of resolved peaks and the distance of the measurement region from the center of rotation. The measurements were made at distances of 5 cm, 8.75 cm, 10 cm, 11.25 cm and 12.5 cm from the center of rotation. The spectrum corresponding to the measurement at 5 cm is not resolved, however, the shape of the spectrum still contains the velocity information. The bars in Figure 2 represent the uncertainty of distance (or velocity) measurement due to the fat beam ($4\sigma \hat{=} 3$ mm) used in the measurement.

In summary, we may state that surface flow velocities can be measured by studying the light scattered from the capillary waves on the moving interface. A non-linear least squares procedure will be required in the analysis of the line shape of spectra obtained from slow flows. The experimental and theoretical understanding of the experiment are sufficient for this extension to be accomplished.

As a final remark, we note that the unexpected splitting of the power spectrum, measured by Mann et al.[4] for scattering from a pumped ripplon field was very likely due to a surface velocity field set up by the device used to force the surface into high amplitude ($< 10^{-4}$ cm) random waves.

References

1. R. H. Katyl and U. Ingaard, Phys. Rev. Lett. $\underline{19}$, 64 (1967).

2. S. Härd, Y. Hammerius and O. Nilsson, J. Appl. Phys. $\underline{47}$, 2433 (1976).

3. D. Byrne and J. C. Earnshaw, J. Phys. D: Appl. Phys. $\underline{10}$, L207 (1977)
   & $\underline{12}$, 1133 (1979).

4. J. A. Mann, J. F. Baret, F. J. Dechow and R. S. Hansen, J. Coll. and Interface Sci $\underline{37}$(1), 14 (1971).

5. R. S. Hansen and J. A. Mann, J. Appl. Phys. $\underline{1}$, 152 (1964).

6. F. Durst, A. Melling and J. H. Whitelaw, "Principles and Practice of Laser Doppler Anemometry," Academic Press (1976).

7. J. A. Mann, unpublished.

8. R. S. Sirohi, R. V. Edwards and J. A. Mann, Jr., Appl. Opt. (communicated).
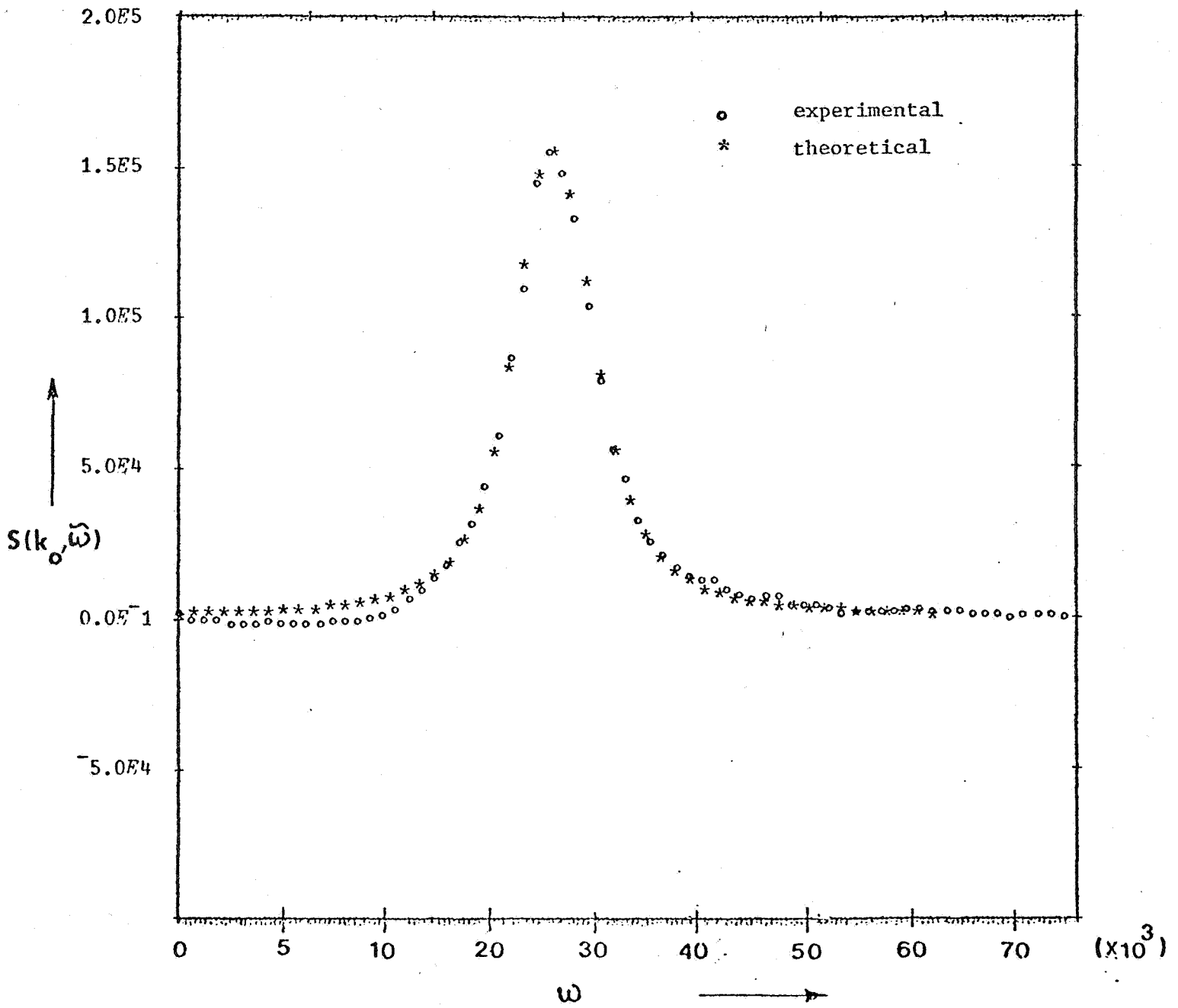
Figure 1a. Experimental and Theoretical Power Spectra from Stationary Surface.
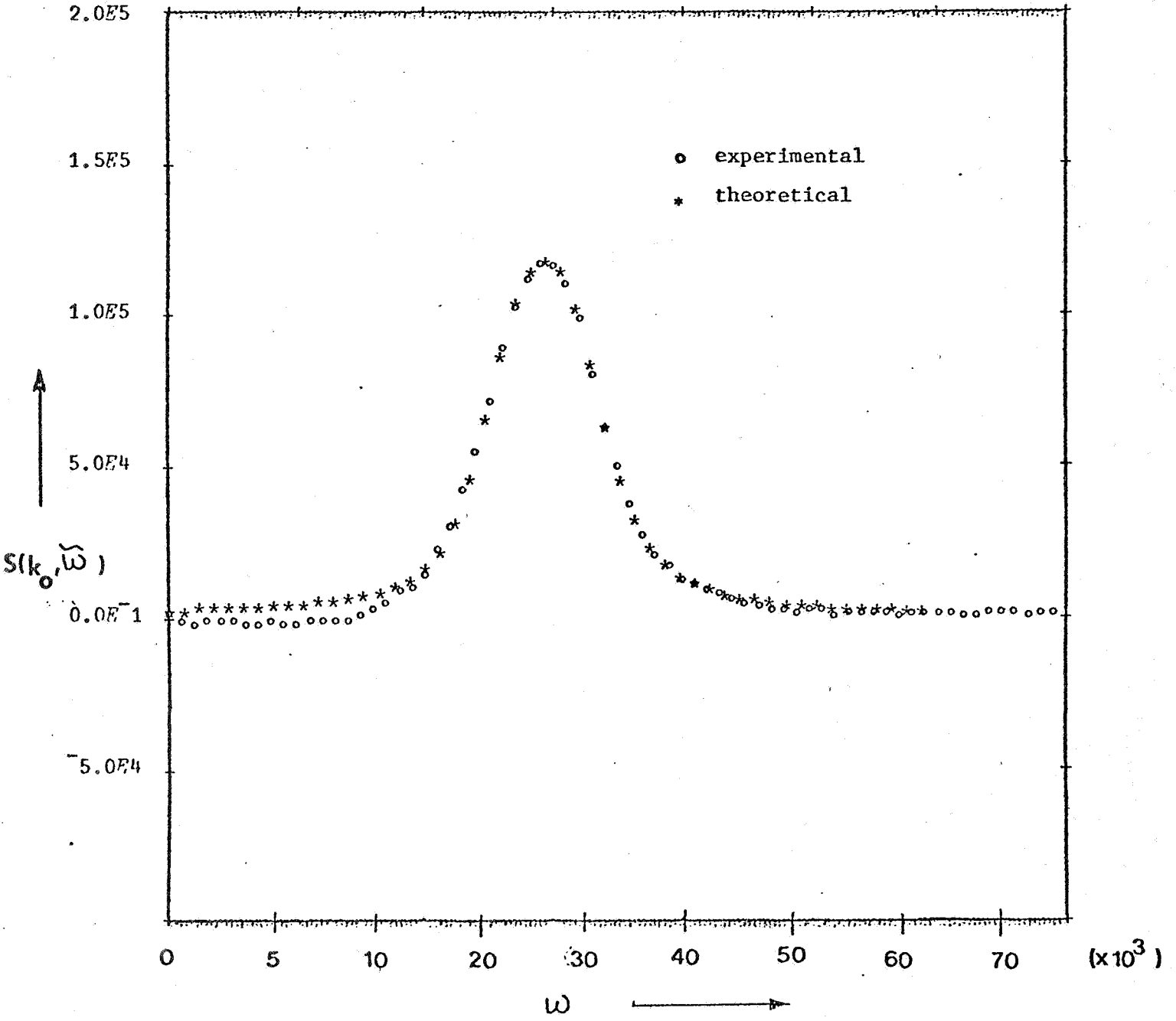
Figure 1b. Experimental and Theoretical Power Spectra from the Moving
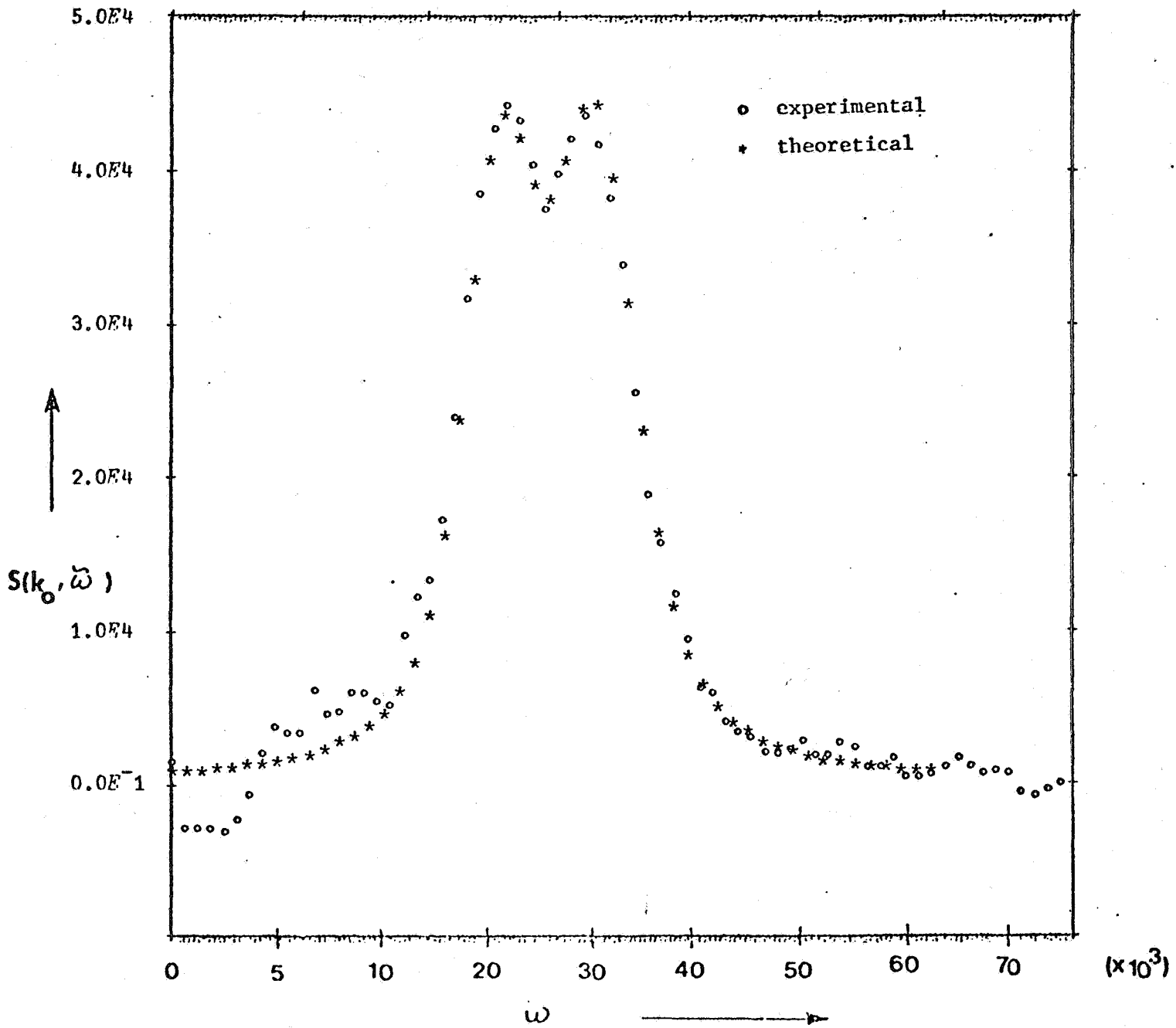Surface — Velocity = 5.5 cm/sec.

Figure 1c. Experimental and Theoretical Power Spectra from the Moving Surface —
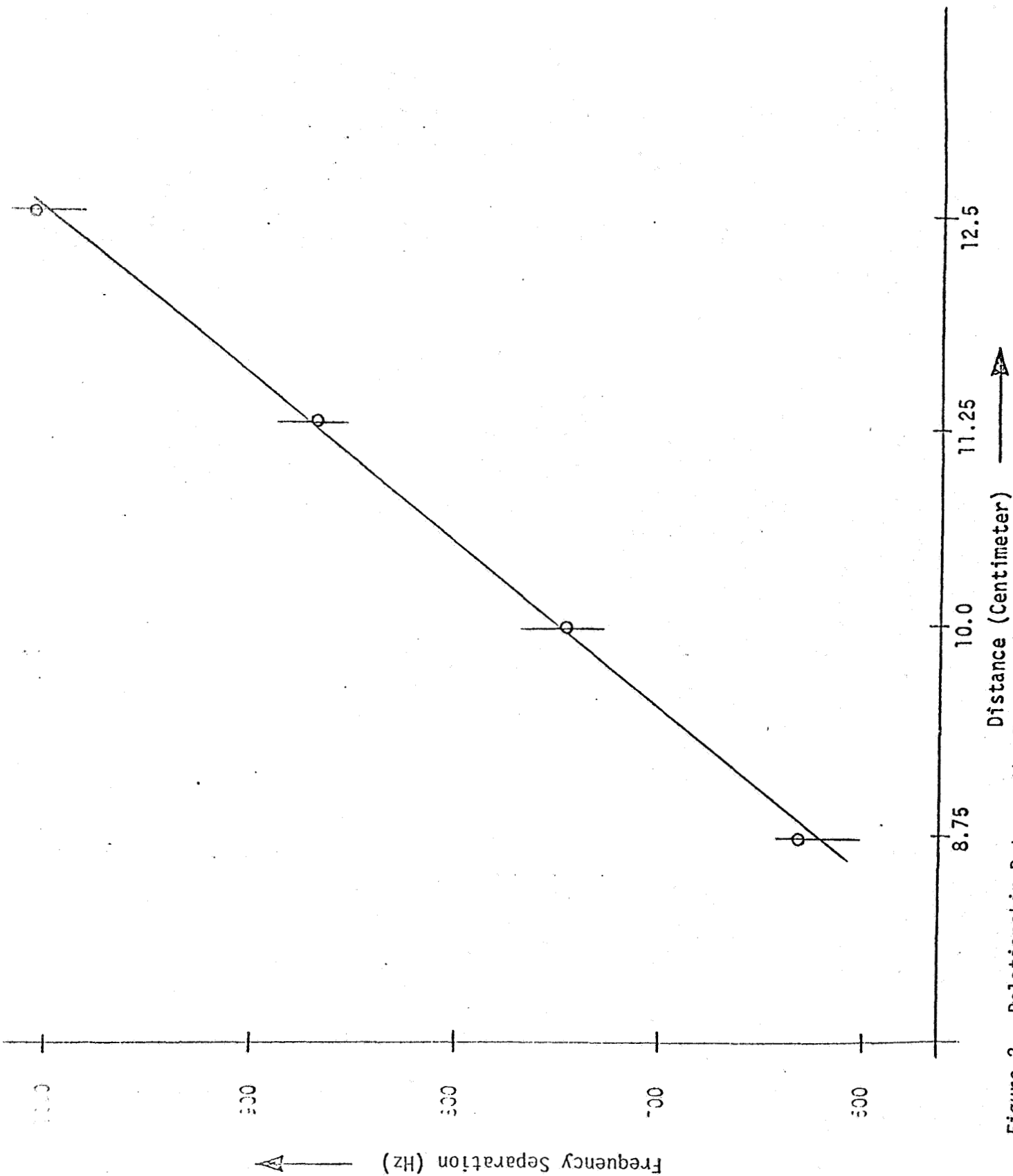Velocity = 9.5 cm/sec.

145

Figure 2. Relationship Between the Frequency Separation of the Peaks and the Distance (Velocity) of the Region of Measurement from the Axis of Rotation.

C. Surface Fluctuations of Nematic Liquid Crystals
    L. B. Shih, G. H. Brown, J. A. Mann
    Fall Meeting of the American Chemical Society,
    25 August, 1980 in Las Vegas, Nevada

We presented the results of L. B. Shih's work on determining the surface

tension of materials as a function of temperature using our light scattering

techniques.

The figures used in that presentation are included here and form the

basis of a paper that is being written for publication and is part of the

thesis to be submitted by L. B. Shih. A copy of her thesis will be submitted

as a final report of the design effort we have made on utilizing the light

scattering methodology for surface tension studies.

We have concluded that surface scattering is the method of choice for

a wide range of systems. In fact we feel that commercialization of our

methodology might be possible.

Figure 1.

A general schematic of the surface light scattering apparatus.
Temperature controlled to ca 0.01°C and the temperature gradiants
are about 0.01°C/cm. This is satisfactory for the studies of
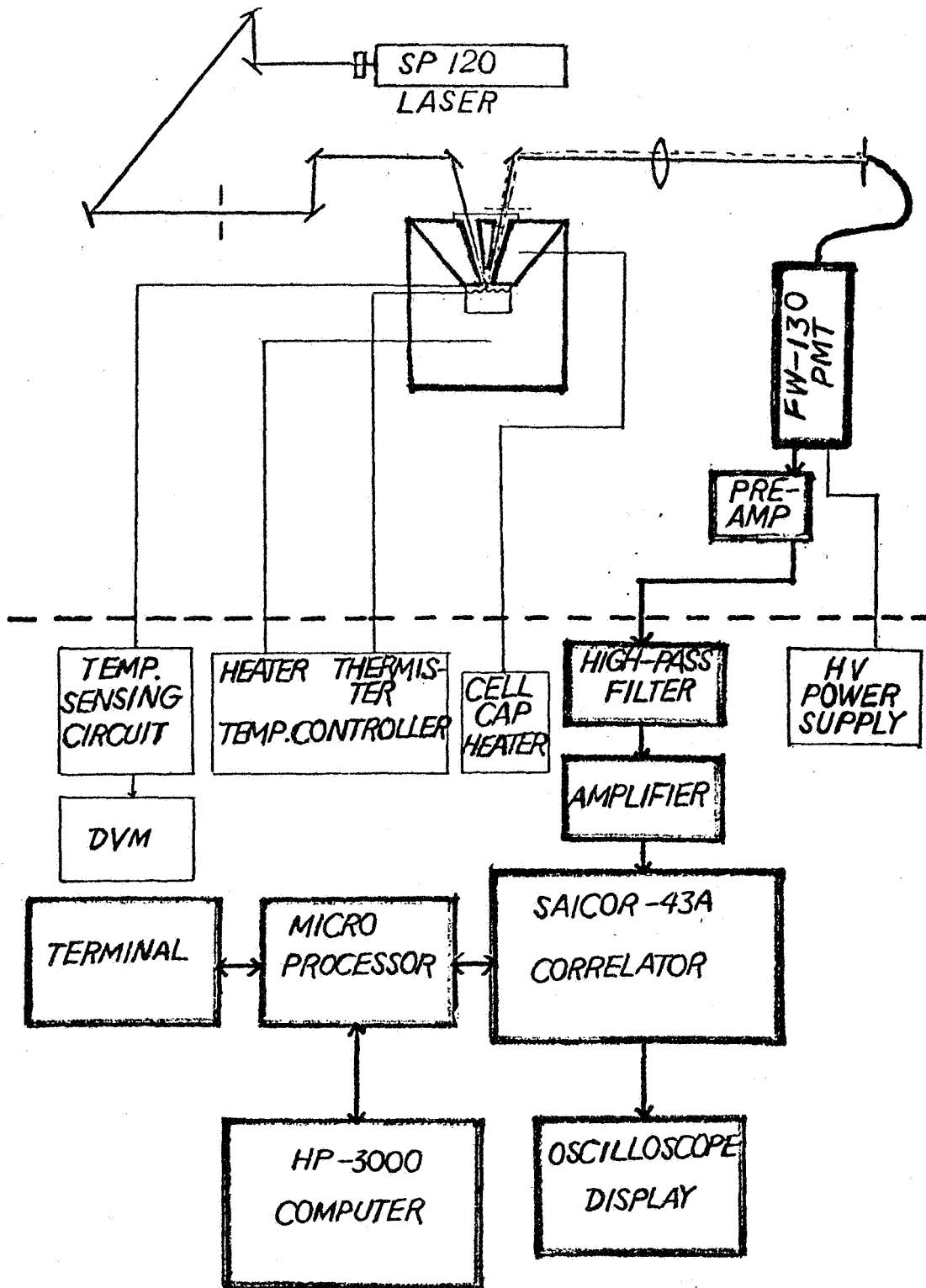mercury and gallium but it is a bit crude for modern phase transition
studies.

Figure 1

149

Figure 2.

A close-up view of the scattering cell showing details of the
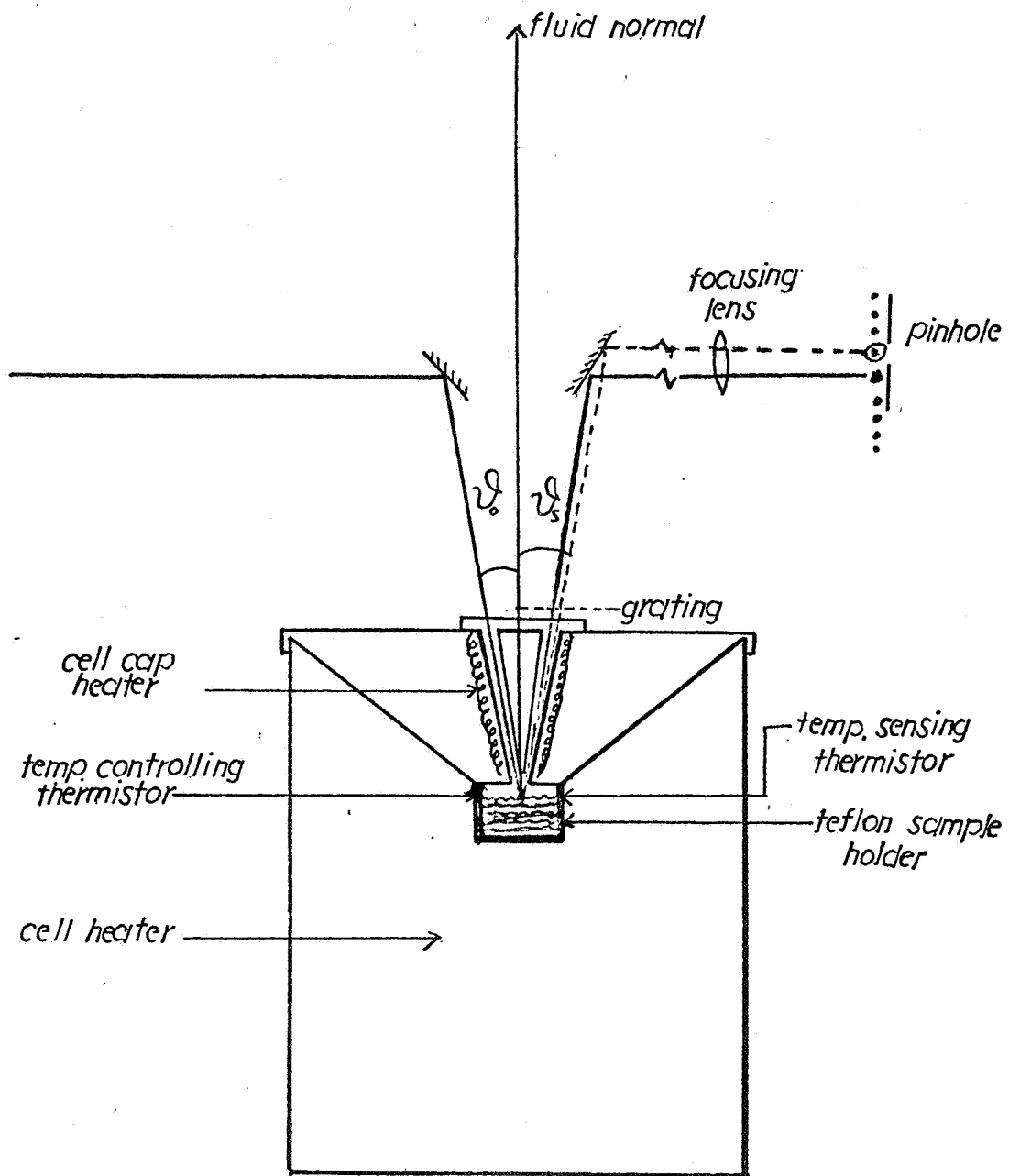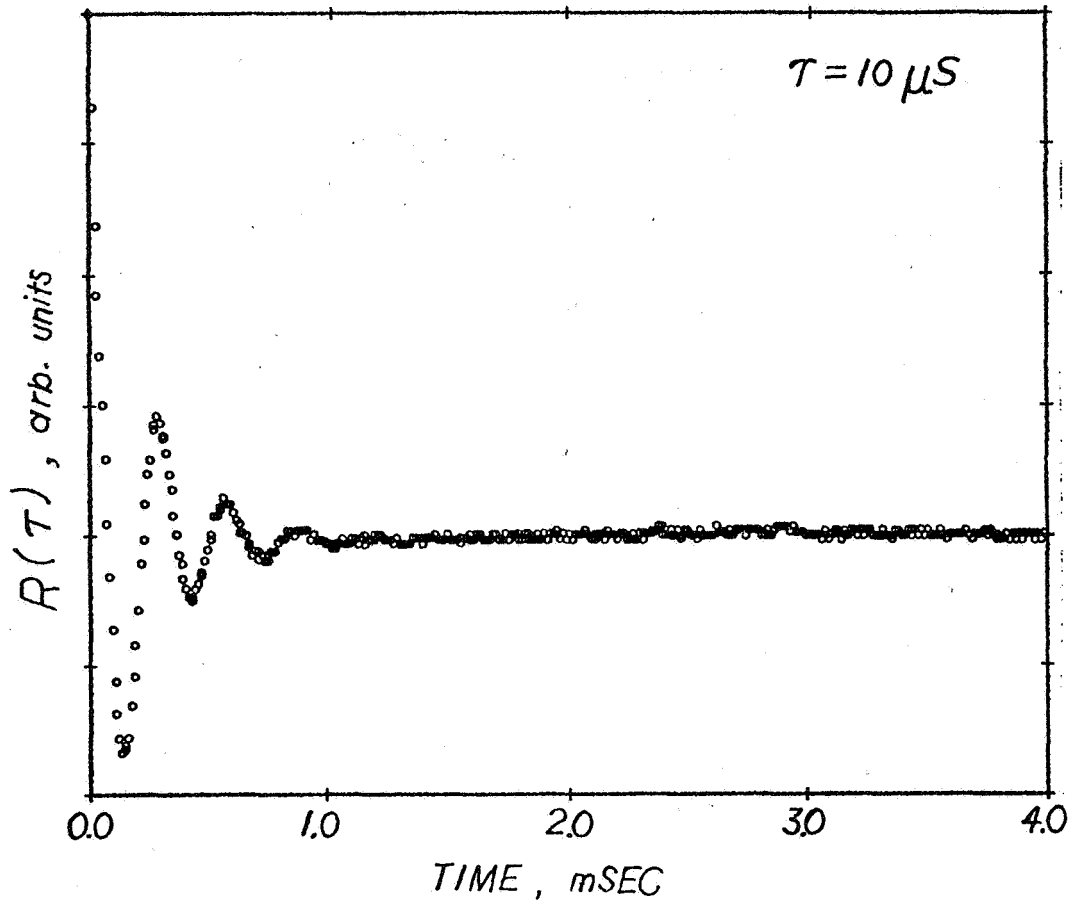thermostate and the optical path.

fluid normal

focusing
lens

pinhole

grating

cell cap
heater

temp. sensing
thermistor

temp controlling
thermistor

teflon sample
holder

cell heater

Figure 2.

Figure 3.

A typical autocorrelation function of the scattered field. This

is the form of the raw data.

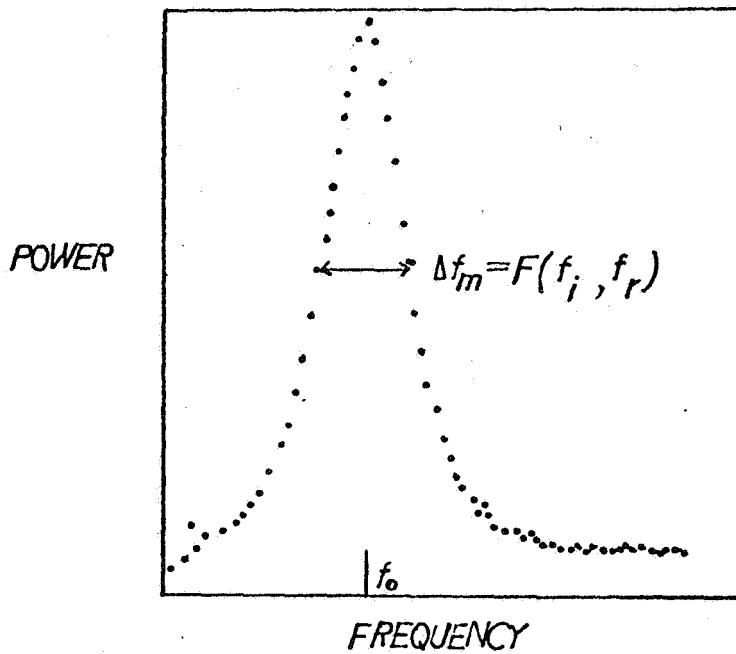$$R(\tau) = A\delta(\tau) + Be^{-\Gamma\tau}\cos\omega_0\tau + C$$

DATA CODE :

PAA 14.-PS 1439 , PAA at 132.3° C

Figure 3.

Figure 4.

The raw data is transformed into the uncorrected power spectrum. The instrumental effects that involve grating effects (see Sirohi, Edwards and Mann in a previous section) must be applied in order to find a deconvolved spectrum for fitting to the power spectrum. Alternately, the line width and frequency of the raw power spectrum can be converted to the numbers corresponding to the deconvolved spectrum.

INSTRUMENTAL FUNCTION

$$I^2(\omega,k) = I_o^2(\omega,k)\, exp\left[-(k-k_o)^2\left(\frac{D}{4\cos\vartheta}\right)^2\right]$$

$$\Delta k_i = 2\sqrt{\ln 2}\,\left(4\cos\vartheta/D\right)$$

$$\Delta f_i = (4\sqrt{\ln 2}/\pi D)\cos\vartheta\,\frac{d\omega}{dk}$$

$$\Delta f_i = 1.590\left(\frac{1}{D}\right)\sqrt{\sigma k_o/\rho} \quad when \;\cos\vartheta = 1$$

$$\Delta f_r \cong \Delta f_m - \frac{\Delta f_i^2}{\Delta f_m}$$
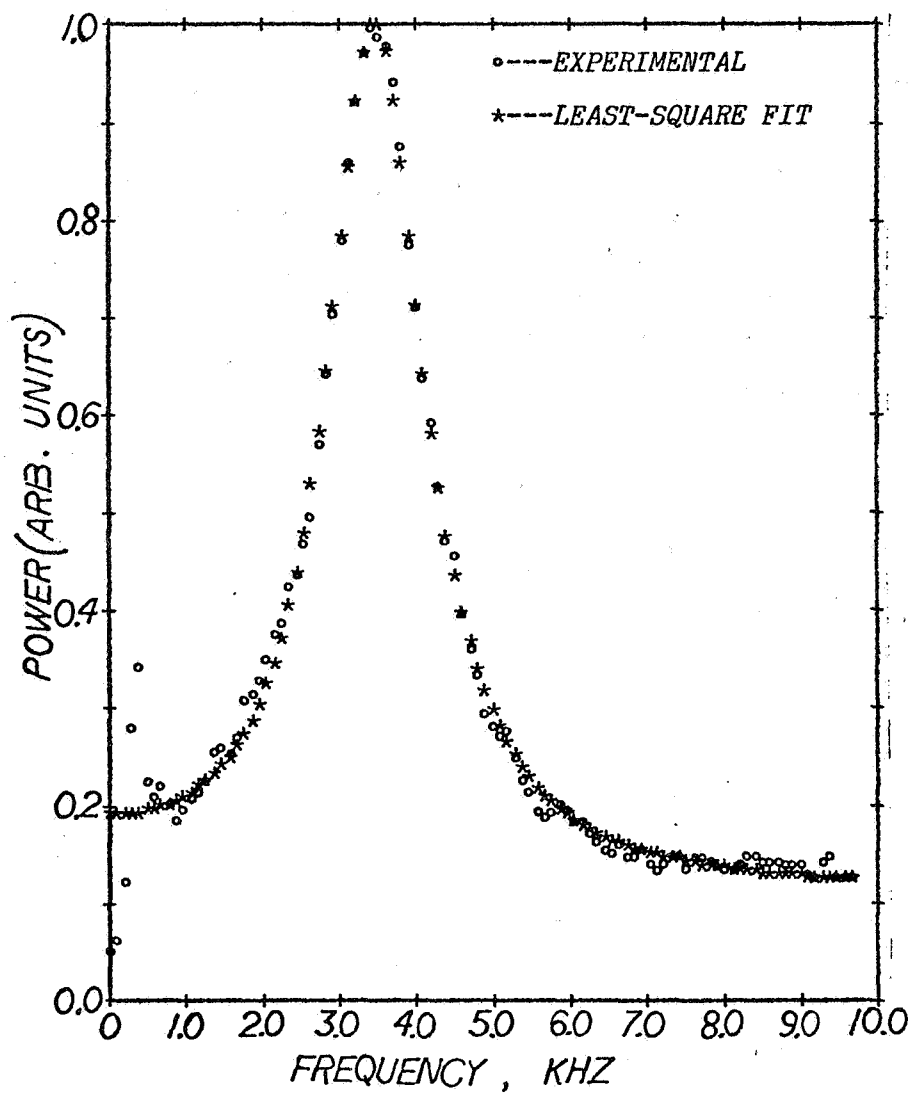
BANDWIDTH AT
HALF HEIGHT :

Δf_m : MEASURED

Δf_i : INSTRUMENTAL

Δf_r : RIPPLON

Figure 4.
155

Figure 5.

The autocorrelation function has been transformed into a corrected

power spectrum which is then fit by the Lorentzian line shape funtion.

The line width parameter, Γ, and frequency, ω_0, are determined by a

weighted least-squares algorithm.

$$P(\omega) = A' + B'\left[\frac{\Gamma}{\Gamma^2 + (\omega - \omega_o)^2} + \frac{\Gamma}{\Gamma^2 + (\omega + \omega_o)^2}\right]$$

DATA CODE :   PAA/4 – PS/440
            PAA at 132.3°C

$f_o = \omega_o/2\pi = 3.469$ KHZ ,CENTER FREQUENCY

$\Delta f_m = \Gamma/\pi = 1.532$ KHZ ,BANDWIDTH AT HALF-HEIGHT

Figure 5.

157

Figure 6.

The surfact tension variation with temperature is shown for para-azoxydianisole. The precision of the measurements were $\pm$ .2mN/m and the accuracy was about $\pm$ .4mN/m. We expect to refine the technique to the $\pm$ .1mN/m accuracy range. However, we feel that the results shown here support our view that the light scattering method is suitable for determining the surface tension to high accuracy without invading the s ample with porbes. The technique is fast. The data collection takes ca 1 min. The data reduction is handled by APL functions as a part of the data acquisition system. These calculations execute within 1 min.
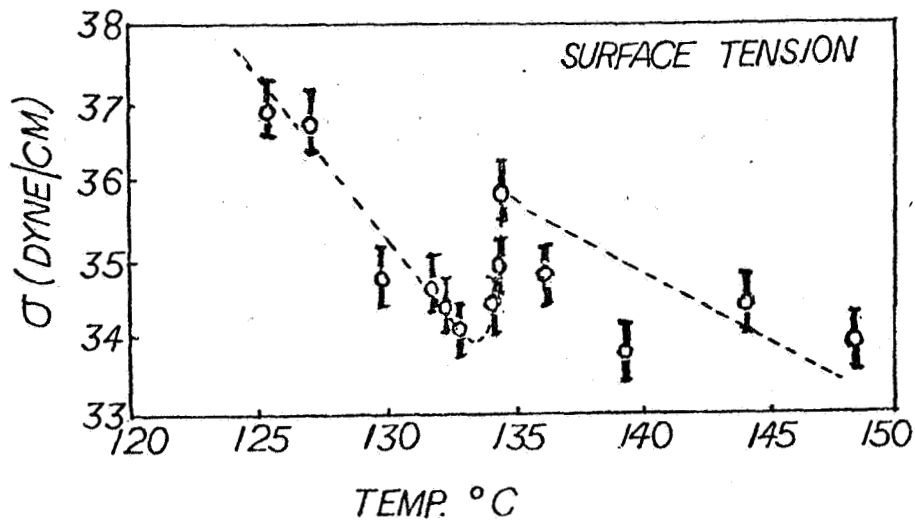
SURFACE TENSION OF PAA:

REPORTED VALUES: 1. $\sigma = 38$ DYNE/CM at $128°C$
(Naggiar and Schwartz and Moseley)

2. $\sigma = (38 \pm 4)$ DYNE/CM at $122°C$
(Langevin and Bouchiat)

OUR MEASUREMENTS: $\sigma = 36.9$ DYNE/CM at $125.4°C$

$\sigma = 34.8$ DYNE/CM at $129.9°C$

SHEAR VISCOSITY OF PAA:

REPORTED VALUES: 1. $\mu \approx 2.8$ cP at $128°C$
(Becherer and Kast)

2. $\mu = (3.6 \pm 0.4)$ at $122°C$
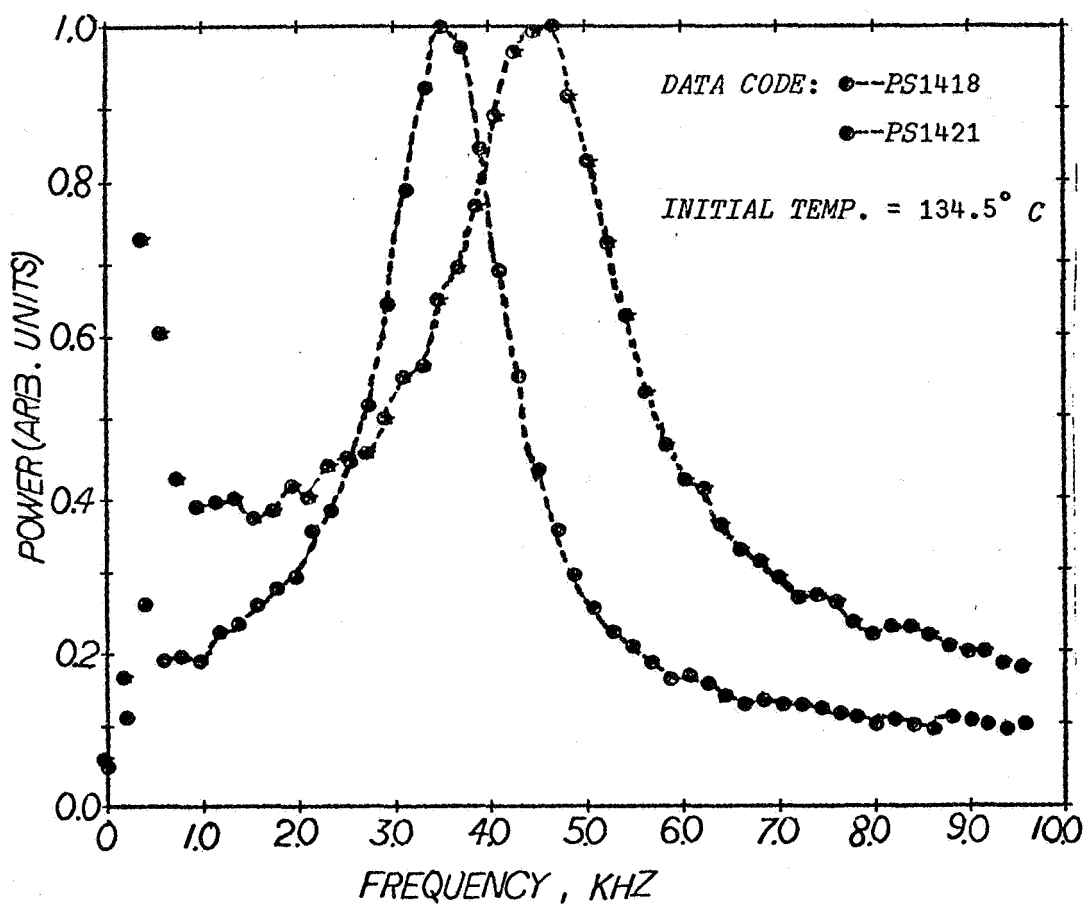(Langevin and Bouchiat)

OUR MEASUREMENTS: $\mu = 2.77$ cP at $125.4°C$

$\mu = 2.33$ cP at $129.9°C$

Figure 6.

159

Figure 7.

Temperature jump measurements are reported here and in the next figure. The temperature was "jumped" from 134.4°C to 135.5°C over 15 min. The result was a striking change in the power spectrum as shown here. The ω_0 value increased by ca 1000 Hz and the width increased as well.

DATA CODE: ●--PS1418
●--PS1421

INITIAL TEMP. = 134.5° C

● CURVE : EQUILIBRIUM TEMP.   134.5° C

$$f_o = 3.535 \ KHZ \left.\begin{array}{c} \\ \\ \end{array}\right\} \Rightarrow \quad \sigma = 35.80 \ DYNE/CM$$

$$\Delta f_m = 772 \ HZ \qquad\qquad \mu = 2.97 \ c.POISE$$

● CURVE : TRANSIENT TEMP. SLIGHTLY >134.5° C

$$f_o = 4.684 \ KHZ \left.\begin{array}{c} \\ \\ \end{array}\right\} \Rightarrow \quad \sigma = 62.64 \ DYNE/CM$$

$$\Delta f_m = 1059 \ HZ \qquad\qquad \mu = 3.97 \ c.POISE$$

Figure 7.

161

Figure 8.

The transient experiment is summarized here showing the extreme sensitivity of surface fluctuations to very small changes in temperature close to the transition temperature. The large effective surface tension numbers represent a transient effect and are not equilibrium surface tension numbers. We do not have a good model for these observations at this time.
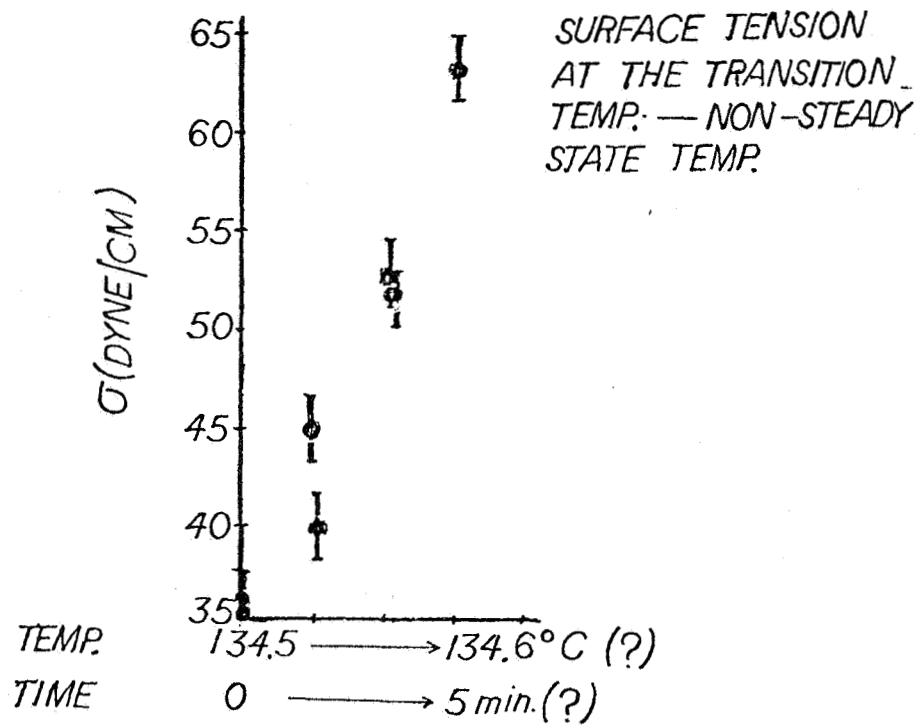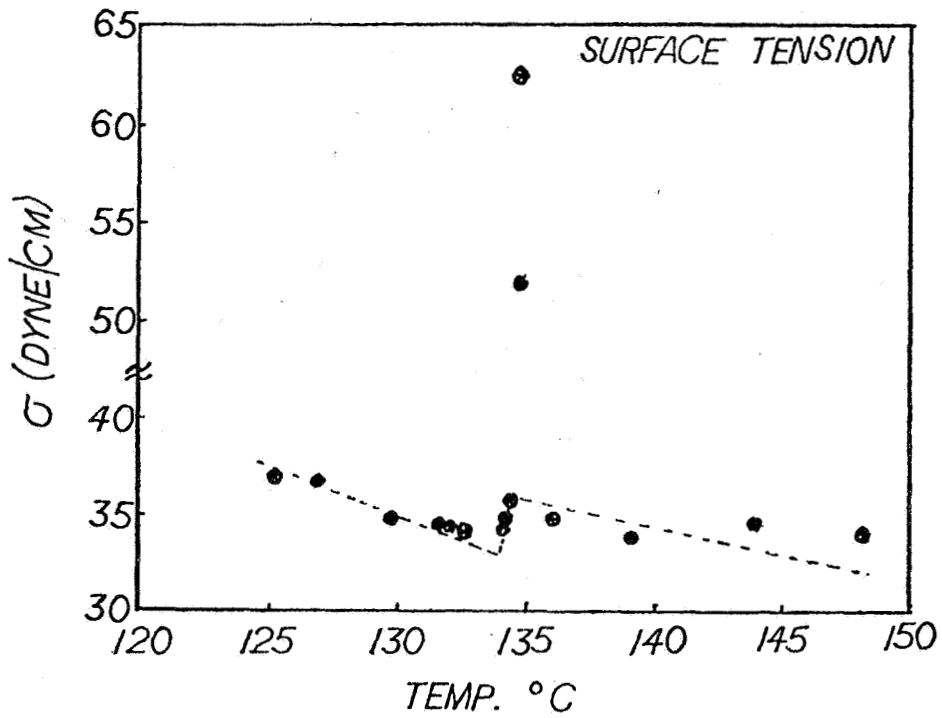
Figure 8.

163

II. Surface LDV Design and Evaluation

The purpose of this subproject was to develope a crossed beam
LDV that would work for surfaces seeded by small particles. Further,
we are to compare the sensitivity and accuracy of this instrument with
the ripplon light scattering apparatus. In particular we intended to
run the evaluations on the A.D. Little thin film apparatus for arranging
surface tension driven flows due to temperature gradients.

We have completed the development and this work is described in
the next paragraphs. The evaluation is not yet completed since the
A.D. Little experiment could not continue for fiscal reasons. However,
we have worked out an alternate way of evaluating the two pieces of
equipment with the following conclusions.

The seed system to be described works down to the Brownian motion limit
of the ca $10\mu m/sec$ velocity range. Typically, 2% to 5% precision is
obtained in these measurements. However, the problem of seeding the surface
is harder than we expected. At this time, appropriate seed material
(ca $1\mu m$ particles) must be selected for each system studied. The surface
chemistry of floating the seeds can be difficult and they are often a
source of surface contamination. It is apparent that curved surfaces can
be handled more easily using the crossed beam techniques than with the
ripplon techniue.

The ripplon technique enjoys the great advantage that seeding is not
necessary. It certainly is the method of choice when surface tension
measurements are to be studied along with the surface velocity fields.

164

However, the technique is limited to faster flows than is possible with the cross-beam, seeded LDV technique. The magnitude of the surface velocity should be above 100µm/sec for effective use of the ripplon technique. In fact, 1000µm/sec is a confortable range. In contrast the seeded system will go down to 10µm/sec without difficulty.

We have shown that there is a strong curvature effect in the ripplon scattering power spectrum. Fortunately the theoretical basis for the effect is obvious and can be dealt with effectively. Never the less, the problem of deconvolving the ripplon power spectrum is harder for cylinder interfaces systems than for flat interfaces.

In late March, early April of 1980, the initial version of the laser anememeter was installed at the recently completed surface tension driven flow apparatus located at the A.D. Little facility in Cambridge, Massachusetts. At the time of this installation the need for modification of several design parameters became obvious and an effort to construct a second system to incorporate these needed changes was initiated by our group.

We obviously needed a flow cell which would model the fluid flow characteristic of the actual cell being used at A.D. Little. Preliminary attempts to generate mechanically flows on the order of one millimeter per second or slower, involving fluid depths of only a few millimeters were deemed inadequate due to overall flow rate instability and control, and the seemingly ubiquitous presence of fluid vibrations of a compatable dimensional scale with those of the desired fluid velocities.

For these reasons, a simple convection driven flow cell was constructed. A combination of electrical resistance heaters and a solid state thermo-electric cooling module was employed to create a fluid density gradient across the surface of a teflon block of area of 16 cm^2.

The heating and cooling elements were affixed to aluminum flanges which set flush against the interior walls of the cell. The hot side of the cooling module was joined via a copper block of approximately 16 cm^3 in volume to a large tank which functions as a heatsink. Because the working temperature differential between the module and the ambient room temperature is only on the order of 2-3°C, the surface area of the heatsink was calculated to be 5000 cm^2 or greater. This was accomplished by constructing a copper tank in the form of a cube 20 cm on a side. Three sides are covered fully by finned aluminium panels. The tank was then filled with H_2O to aid in uniformly distributing the heat throughout the volume. Even without the aid of a servo-regulated temperature controller, it was observed that flows on teh order of 10^{-1} mm/sec or less could be easily generated in a stable fashion. Under such operating conditions, the heating and cooling modules were presenting about 7 watts of power to the fluid volume. Note that we designed only to obtain surface flows we have not duplicated the A.D. Little apparatus.

The optical modifications centered around three main features. Most importantly, the f number of the main converging lens was increased by a factor of 4. In doing so, the k vector presented to the surface was increased by the same factor, which facilitated the accurate detection of much smaller rates of flow. In addition, the depth of the sample volume was decreased by the same factor, thus providing a more accurate measure of the actual flow at the surface.

In the initial optical system, the dual beams were generated by presenting a spatially expanded laser source to a flat glass dish with selectively mirrored spots deposited on its surface. The additional working space created

166

by the larger diameter converging lens allowed this disc to be replaced by a combination of beam splitters and corner reflectors. In addition to being easier to align, the intensity of the interference pattern projected onto the fluid surface was greatly increased, since the laser source did not have to be intially expanded spatially.

The third modification was essentially to provide for increased ease of operation. By positioning a 45° reflecting surface at the top of the optional column, the sensitive alignment procedure could be undertaken from beside the apparatus, instead of from above. A 4x microscope was also incorporated into the viewing aperture in order to more closely observe the sample volume. The microscope is secured to a pivoting mount; once the system has been aligned, the microscope is moved out of the focal region, and the photomultiplier tube is connected to the pinhole aperture via a fiber-optic bundle.

Tests were run to show that the flows could be detected and measured accruately at the 10μm/sec velocity range. These tests were satisfactory. We did find a problem with the preamplifier for the detection system which has now been corrected. This system will be taken to A.D. Little for the remaining studies when their funding situation allows the work to continue.

We feel that this phase of the development work promised in the contract is finished. A separate report will be written over the next six months describing the LDV apparatus and its evaluation in detail.

We set up a cruder version of the LDV apparatus for a series of measurements on the apparatus designed by the Ostrach group. The preliminary data will be discussed in his report. A refined apparatus will be set up for their use when appropriate.

III. Studies of Surface Structure of Monolayers

Several subprojects supported by the contract are advancing but at a slower pace as a result of directing most of our effort toward the ripplon scattering technology and toward the surface LDV surface technology.

A. Interferometric method for the study of the visco elastic properties of contaminents on liquid metal systems.

The optical part of this system for characterizing small amplitude, forced fluctuations on surfaces is complete and works well. Devices for forcing the liquid surface into motion are being developed. One such device uses an oscillating, large, electronic field gradient. The second device uses a ultra sonic generator of special design. Our rate of progress on these details is frustratingly slow.

Manipulation of liquid metal surfaces requires special techniques. The NBS work (S. Hardy) is sufficiently advanced that we will be able to use several of their methods to attain relatively clean surfaces. These techniques are difficult to implement in our apparatus. In general we are using the techniques devised by Dr. B. J. Kinzig (Naval Research Laboratory, Washington, D.C.) for dealing with liquid mercury.

Mann and Kinzig have done a detailed analysis of the electron beam scattering to be expected from liquid gallium when monolayers of various materials are distributed on the surface. There is no doubt left after this study that low energy electron diffraction or high energy electron diffraction studies will be definitions in determining the structures of monolayers packed on liquid gallium surfaces. This work will be complimentary and supportive of the NBS effort by S. Hardy.

IV. Future Work

A. The light scattering work will be directed toward the analysis of monolayers spread on liquid mercury and liquid gallium. Temperature effects on the visco-elastic properties of monolayers will be determined. We will compare our results, where possible, with those coming from the NBS group. The effect of surface visco-elastic properties of liquid gallium under float zone operating conditions on surface tension driven flows will be studied.

B. Reports and papers will be written on the crossed beam LDV system we have designed. Some additional data may be collected as part of the evaluation program.

C. Work on determining the structure of compact monolayers on liquid gallium will be continued with the hope of attempting a definitive experiment using a high energy electron diffraction system located at NASA-Lewis in Cleveland.

D. We wish to initiate a fundamental study of the solid-liquid float zone interface using interfacial fluctuations in a transparent medium. The fluctuations would be studies using our several light scattering techniques.

APPROVAL

FLOAT ZONE WORKSHOP

Edited by R. J. Naumann

The information in this report has been reviewed for technical content. Review of any information concerning Department of Defense or nuclear energy activities or programs has been made by the MSFC Security Classification Officer. This report, in its entirety, has been determined to be unclassified.

CHARLES A. LUNDQUIST
Director, Space Sciences Laboratory

170